Effect of Fluidization Temperature and Catalyst Presence on the Extent of Wall Fouling and Charge Distribution in Polyethylene Gas-Solid Fluidized Beds

by

Mohsen Isaac Nimvari

uOttawa

A thesis submitted in partial fulfillment of the
requirements for a

DOCTOR OF PHILOSOPHY IN CHEMICAL ENGINEERING

Department of Chemical and Biological Engineering
Faculty of Engineering
University of Ottawa

Abstract

Electrostatic charge transfer among solids can pose significant operational challenges in various industries dealing with solid handling and processing including pneumatic conveying, gas-solid fluidization, etc. This phenomenon, known as triboelectrification or contact electrification, has been notably observed to negatively affect the gas-phase polyethylene production process. In this process, polyethylene resin is produced in a gas-solid fluidized bed reactor, while the catalyst is injected into the reactor to initiate polymerization reaction. The contact electrification among particles and particles with the reactor wall prompts the adhesion of polyethylene and catalyst particles to the reactor wall, forming a thick layer, an occurrence known as *sheeting. Sheeting* can eventually necessitate reactor shutdown, and in turn, resulting in significant economical loss due to production downtime and maintenance costs. Therefore, it is essential to investigate the mechanisms and parameters that potentially influence the polarity and magnitude of the generated charge in such reactors in order to determine mitigation techniques. Given that the gas-phase polyethylene reactors temperature typically ranges from 80ºC to 110ºC, studying the triboelectrification of polyethylene at these temperatures is important. Furthermore, contact electrification is primarily a surface phenomenon, and thus, particles with various surface chemistry are able to alter electrostatic charge generation magnitude or charge transfer direction. Consequently, catalyst particles with diverse and complex chemistries could potentially be a key player influencing *sheet* formation in commercial polyethylene reactors. This thesis attempts to provide information concerning the influence of temperature and the presence of catalyst on triboelectrification and fouling formation in gas-phase polyethylene fluidized bed reactors.

The first investigation of this thesis focuses on assessing the effect of temperature, which spanned from 24°C to 58°C, on the electrostatic charging characteristics of a commercially manufactured linear low-density polyethylene (LLDPE) resin. This examination was conducted within a pressurized pilot-plant fluidized bed operating at 2600 kPa. Through these experiments, the amount of wall fouling and the charge of particles in the bed, including those fouled on the wall and those entrained, were examined. Results indicated a significant reduction in wall fouling as the fluidization temperature increased to 58°C from 24°C, corresponding to a reduction in net specific charge of the fluidized particles. To delve deeper into the mechanism behind the influence of temperature on solid's charging, shake tests were performed to also

differentiate the effects of types of contacts within the fluidized bed, namely interactions between polyethylene particles and between particles and the stainless-steel column wall. No variation in charge transfer behaviour between particles and a stainless-steel cup was observed with increasing temperature, whereas charge transfer for insulator-insulator contacts reduced. A volume resistivity measurement cell was constructed in-house in accordance with ASTM D257 standards, and the volume resistivity of various insulator films (nylon, LLDPE and LDPE) was measured at 23°C and 60°C. Volume resistivity measurements confirmed the decline in materials' volume resistivity as temperature increased, in turn validating the contribution of this parameter to the reduction in charge transfer in the fluidized bed.

In the subsequent investigation, the triboelectric consequences which are originated from chemistry of catalysts employed in polyethylene production, as well as their components including the catalyst support and cocatalyst, are investigated. Silica as the catalyst base, methylaluminoxane as the cocatalyst, and a metallocene catalyst in both active and deactivated forms were studied at two mass loadings. These samples were introduced to a bed of LLDPE resin through a pneumatic conveying line, and the electrostatic charge generation of each sample in the conveying tube and in the fluidized bed was examined. Low powder concentration of 100 ppm did not affect the resin charging; however, 1000 ppm concentrations led to notable changes. Methylaluminoxane was believed to be ionized in the bed, and in turn, significantly mitigated the amount of fouling as well as charge generation. Metallocene catalysts, without altering the bed charge magnitude and polarity, caused a substantial augmentation in the mass of fouling by retaining fine particles in the bed. Adding static control agents to the catalyst helped in suppressing the resulted fouling augmentation. Furthermore, powders with an acidic property such as silica and deactivated metallocene catalyst induced a negative polarity to the bed.

The concluding investigation concentrates on the impact of electrostatic charge on particle's pneumatic conveying velocity. This influence was investigated by measuring particle velocity through a new measurement technique developed in-house to measure particle velocity based on the electrostatic charge of particles in pulse pneumatic injections inside a conductive tube. Results from this measurement were in good agreement with a video imaging technique, and it was revealed that particle velocity is influenced by the turbulency of the conveying gas as well as the presence of electrostatic charge on particles, a parameter that is not included in the existing empirical and semi-empirical models proposed to predict particles conveying velocity.

Résumé

La transmission de charge électrostatique entre les solides peut entraîner des difficultés opérationnelles significatives dans diverses industries, notamment lorsqu'il s'agit de procédés impliquant des solides, tels que le transport pneumatique et la fluidisation gaz-solide. Il a été démontré que ce phénomène, connu sous le nom de triboélectrification ou d'électrisation par contact, affecte négativement le procédéde production de polyéthylène en phase gazeuse. Dans ce procédé, la résine de polyéthylène est produite dans un réacteur à lit fluidisé biphasique (gaz-solide), avec le catalyseur injecté dans le réacteur pour initier la réaction de polymérisation. L'électrification, par contact entre les particules, et entre les particules et la paroi du réacteur, entraîne l'adhérence des particules de polyéthylène et de catalyseur à la paroi, formant ainsi une couche épaisse, un phénomène pouvant être qualifié de *formation de plaques*. La *formation de plaques* peut éventuellement nécessiter l'interruption du fonctionnement du réacteur pour son entretien, entraînant des pertes économiques importantes. Par conséquent, il est essentiel d'étudier les mécanismes et les paramètres qui peuvent potentiellement influencer la polarité et l'ampleur de la charge générée dans de tels réacteurs afin de déterminer les méthodes appropriées pour y remédier. Étant donné que la température des réacteurs de polyéthylène en phase gazeuse varie généralement de 80°C à 110°C, l'étude de le triboélectrification du polyéthylène à de telles températures devient imminente. De plus, l'électrification par contact est principalement un phénomène qui surgit sur les surfaces, ce qui signifie que les particules présentant différentes chimies à la leur peuvent modifier la fréquence de génération de charge électrostatique ou la direction du transfert de charge. Par conséquent, les particules de catalyseur avec des chimies diverses et complexes pourraient potentiellement jouer un rôle clé dans l'influence de la *formation de plaques* dans les réacteurs de polyéthylène commerciaux. Cette thèse tente de fournir des informations concernant l'influence de la température et de la présence de catalyseur sur le triboélectrification et la formation de dépôts dans les réacteurs à lit fluidisé de polyéthylène en phase gazeuse.

La première étude de cette thèse porte sur l'évaluation de l'effet de la température, de 24°C à 58°C, sur les caractéristiques de chargements électrostatiques d'une résine de polyéthylène de basse densité linéaire (PEBDL) commerciale. Cette étude a été réalisée dans un lit fluidisé de taille industrielle opérant à 2600 kPa. À travers ces expériences, la formation de dépôts sur les

parois et la charge des particules comprenant le lit, y compris celles adhérées aux parois et celles en suspension, ont été examinées. Les résultats ont indiqué une diminution significative de la formation de dépôts sur les parois à mesure que la température de fluidisation augmentait jusqu'à 58°C, illustrant une réduction de la charge spécifique nette des particules fluidisées. Pour mieux comprendre le mécanisme de l'influence de la température sur la charge des particules solides, des tests de secouage ont été réalisés, pour élucider les effets des types de contacts au sein du lit fluidisé, menant à mieux comprendre l'origine des interactions entre les particules de polyéthylène et entre les particules et la paroi en acier inoxydable de la colonne. Aucune variation du transfert de charge entre les particules et la colonne d'acier inoxydable n'a été observée, au fur et à mesure que la température d'opération augmentait. Cependant, le transfert de charge entres matériaux isolant-isolant a diminué. Une cellule utile pour la mesure de la résistivité volumique de certains isolants a été construite conformément aux normes ASTM D257, avec laquelle la résistivité volumique de différents films (nylon, PEBDL et PEBD) a été mesurée entre 23°C et 60°C.

La prochaine étude traite des conséquences triboélectriques, découlant de la chimie des catalyseurs utilisés dans la production de polyéthylène, ainsi que de leurs composantes comprenant le support de catalyseur et le co-catalyseur. La silice, servant de support de catalyseur, et le méthylaluminoxane, en tant que co-catalyseur, en plus d'un catalyseur fait de métallocène, sous forme activée et désactivée, ont tous été étudiés à deux charges massiques différentes. Ces échantillons ont été introduits dans un lit de résine PEBDL à travers une ligne de transport pneumatique, où la génération de charge électrostatique de chaque échantillon, dans le tube de transport et dans le lit fluidisé, a été examinée. Les faibles concentrations de poudre de 100 ppm n'ont pas été suffisantes pour mener au chargement de la résine, cependant, des concentrations à partir de 1000 ppm ont entraîné des changements remarquables. La quantité de dépôts formés à la paroi ainsi que la génération de charge ont considérablement diminuées étant donné le méthylaluminoxane ionisé dans le lit de particules. Les catalyseurs métallocènes, sans modifier l'ampleur et polarité de la charge du lit, ont entraîné une augmentation substantielle de la masse de dépôts en retenant les fines particules dans le lit. L'ajout d'agents de contrôle statique au catalyseur a su empêcher l'augmentation de ces dits dépôts. De plus, les poudres ayant une propriété acide telles que la silice et le catalyseur métallocène désactivé, ont induit une polarité négative dans le lit.

L’étude finale portait sur l’impact de la charge électrostatique sur la vitesse de transport pneumatique des particules. Cette influence a été étudiée en mesurant la vitesse des particules à l’aide d’une nouvelle technique de mesure développée à l’interne, basée sur la charge électrostatique des particules lors d’injections pulsatives pneumatiques à l’intérieur d'un tube conducteur. Les résultats de cette mesure concordaient avec une technique d’imagerie vidéo, révélant que la vitesse des particules est influencée par la turbulence du gaz de transport ainsi que par la présence de charge électrostatique sur les particules, des paramètres qui ne sont pas inclus dans les modèles empiriques et semi-empiriques actuels proposés pour prédire la vitesse de transport des particules.

Statement of Contributions of Collaborators

All chapters presented in this thesis were written solely by me with the editorial comments provided by Dr. Mehrani and Dr. Sowinski.

Chapter 2 is a published work in a peer-reviewed academic journal. I performed all the experiments and analyzed the results with the supervision and editorial comments provided by Dr. Mehrani and Dr. Sowinski who are also listed as co-authors.

Chapter 3 is a published study in a peer-reviewed academic journal. The experimental work and results' analysis were conducted by me with the supervision and editorial comments provided by Dr. Mehrani and Dr. Sowinski who are also listed as co-authors.

Chapter 4 is a manuscript submitted to a peer-reviewed academic journal. The experimental work and results analysis were conducted by me with the supervision and editorial comments provided by Dr. Mehrani and Dr. Sowinski who are also listed as co-authors.

Chapter 5 is a published manuscript in a peer-reviewed academic journal. The experimental work was conducted equally by me and a former PhD student Dr. Milad Taghavivand, and I performed 70% of the experimental design, data analysis and writing. Editorial comments were provided by Dr. Mehrani and Dr. Sowinski who are also listed as co-authors.

Table of Contents

Abstract ..... **ii**

Résumé ..... **iv**

Statement of contributions of collaborators ..... **vii**

Table of contents ..... **viii**

List of tables ..... **xii**

List of figures ..... **xiii**

Nomenclature ..... **xx**

Acknowledgement ..... **xxii**

1 Chapter 1 – Introduction **1**

1.1 Electrostatic Charge Generation 1

1.2 Conductors, Semiconductors, and Insulators 2

1.3 Charge Transfer Mechanisms 4

1.3.1 Metal-Metal Contact 4

1.3.2 Metal-Insulator or Insulator-Insulator Contacts 5

1.3.3 Triboelectric Series 9

1.4 Charge Measurement Techniques 10

1.4.1 Faraday Cups 11

1.4.2 Electrostatic Probes 12

1.5 Gas-Solid Fluidization 13

1.6 Polymerization Catalysts 15

1.7 Electrostatics in Gas-Solid Fluidized Beds 18

1.7.1 Effect of Fluidization Operating Conditions 21

1.8 Effect of Temperature 22

1.9 Effect of Solid's Surface Chemistry 23

1.10 Electrostatic Charging in Pneumatic Conveying 27

1.11 Thesis Objectives 30

1.11.1 Effect of Temperature on Electrostatics in Fluidized Beds 31

1.11.2 Effect of Catalyst on Electrostatic Charging in Polyethylene Fluidized beds 31
1.11.3 Effect of Electrostatic Charging on Solids Conveying Velocity 33
1.12 Thesis Outline 33
References 34

2 Chapter 2 – Effect of Temperature on Triboelectrification of Polyethylene Particles in a Pilot-Scale Pressurized Gas-Solid Fluidized Bed 43
Abstract 43
2.1 Introduction 44
2.2 Materials and methods 47
2.3 Results and discussion 50
2.4 Conclusion 57
Acknowledgement 58
References 58

3 Chapter 3 – Investigation of the role of temperature on contact electrification of polyethylene particles 61
Abstract 61
3.1 Introduction 62
3.2 Material and method 64
3.3 Volume Resistivity 66
3.4 Results and discussion 69
3.4.1 Shake test 69
3.4.2 Volume resistivity 71
3.4.3 Discussion 71
3.5 Conclusion 74
Acknowledgement 75
References 75

4 Chapter 4 – Triboelectrification of a Metallocene Catalyst in an Atmospheric Polyethylene Fluidized Bed 79
Abstract 79

4.1 Introduction 80
4.2 Materials and Experimental Method 88
4.2.1 Materials 91
4.3 Results and discussion 92
4.3.1 Pneumatic injections 92
4.3.2 Fluidization 94
4.4 Conclusion 104
Acknowledgments 105
References 105

5 Chapter 5 – Velocity measurement of pneumatically conveyed particles via a simple current signal technique and the influence of electrostatic charge 112
Abstract 112
5.1 Introduction 113
5.2 Materials and methods 117
5.3 Particle velocity measurement techniques 120
5.3.1 Current Signal Analysis 120
5.3.2 Video Imaging 121
5.3.3 Comparing the two velocity measurement techniques 122
5.4 Results and Discussion 124
5.4.1 Electrostatic charge generation 124
5.4.2 Particle Velocity 127
5.4.3 Back flow observation 132
5.5 Conclusion 134
References 135

6 Chapter 6 - Conclusions and Recommendations 139
6.1 Conclusions 139
6.2 Recommendations for Future Work 142

Appendix A – Experimental Equipment 144

Appendix B – Active Catalyst Injection & Gas-Solid Fluidization Procedure 155

Appendix C – Catalyst polymerization 159
Ziegler-Natta Polymerization..... 159
Metallocene polymerization..... 159

Appendix D – Triboelectric Charging of Particles in Pneumatic Conveying..... 161

Appendix E – Safety Guidelines 164

References 165

List of Tables

Table 1-1 Geldart classification of particles [40]. 14

Table 2-1. Properties of PE particles and the fluidizing gas. 50

Table 2-2. Particle size distribution range of samples collected before (initial) and after fluidization from different regions of the bed for all operating conditions tested. 52

Table 3-1. Operating conditions of the shake tests used in this study. 66

Table 3-2. Insulating film used in volume resistivity measurements. 67

Table 4-1. A summary of findings on the common types of catalyst used in industrial gas-phase polyethylene process and the resulting bed charge polarity measured by electrostatic probe..... 86

Table 4-2. Properties and operating conditions related to the fluidizing particles. 91

Table 4-3. The samples tested in this study together with their size and mass loadings. 91

Table 4-4. Size distribution of PE particles which was measured using a Malvern Mastersizer 2000 for different regions of the column after 1 hour of fluidization. 96

Table 5-1. Summary of particle velocity correlations. 116

Table 5-2. Properties of particles. 119

Table D - 1. Influential Parameters on Triboelectric Charging of Particles in Pneumatic Conveying. 161

Table E - 1. Safety Procedure Regarding Active Catalyst Exposure 164

List of Figures

Fig. 1-1 Charge transfer between two solids as they approach each other, collide and separate. .. 2

Fig. 1-2 Induction charging mechanism. 2

Fig. 1-3 Schematic of energy levels in one atom. E is the energy level of electrons, and yellow lines are the orbitals [8]..... 3

Fig. 1-4 Conduction band and valence band for metals, semiconductors and insulators. Black colour shows the electron density in each band. For metals, conduction and valence band overlap and electrons can easily move between two bands, whereas for insulators, valence band is fully occupied by electrons and to reach next available band (conduction band) high energy is required (copied from [11]). 4

Fig. 1-5 Electron transfer illustration in metal-metal contacts (copied from [14]). 5

Fig. 1-6 Electron transfer illustration in insulator-insulator contacts (copied from [14]). 7

Fig. 1-7 Schematic illustration of ion transfer mechanism (copied from [23]). 7

Fig. 1-8 Schematic illustration of material transfer between two materials, a) AFM height and AFM-Peakforce QNM DMT modulus maps before (top) and after (bottom) contact (PTFE spheres shaken in PS dishes) show PTFE on PS surface (copied from [28]), b) Transfer of material after bond cleavage (copied from [27]). 8

Fig. 1-9 a) An example of a linear triboelectric series, b) An example of a cyclic triboelectric series (copied from [16]). 9

Fig. 1-10 Coulomb force between two point-charges. 10

Fig. 1-11 Electric field in the surrounding of a positive, negative, and neutral particle. 10

Fig. 1-12 Schematic showing how a Faraday cup measures the charge of a charged object. 11

Fig. 1-13 Components of an electrostatic probe. 12

Fig. 1-14 Different flow regimes by increasing fluidization gas velocity (copied from [39]). 13

Fig. 1-15 Schematic of a polyethylene fluidized bed reactor (copied from [43]). 15

Fig. 1-16. An example of chemical structure for a Phillips catalyst. 16

Fig. 1-17 An example of chemical structure for a silyl chromate catalyst. 16

Fig. 1-18. Schematic illustration of an example of mononuclear $TiCl_4$ (a) and active site precursors (b) on the (110) $MgCl_2$ supported on silica. 18

Fig. 1-19 Locations that sheeting may occur in a commercial polyethylene reactor (copied from [1]). 19

Fig. 1-20 Mechanism proposed for wall fouling formation (copied from [65]) 21

Fig. 1-21 Chemical structure of an ionomer (poly(ethylene-co-methacrylic acid)) with an immobile anion covalently bonded to the backbone of the polymer and a mobile cation (copied from [82]). 23

Fig. 1-22 Electrostatic charge of functionalized polystyrene or glass microspheres (200 mm in diameter) after contact electrification with aluminum (copied from [16]). 24

Fig. 1-23 Net specific charge of bulk polyethylene particles and the corresponding total wall fouling in the presence of different additives including silica (Si), AS-990 (A), aluminum distearate (B), calcium stearate (C), CHIMASSORB 944 (D), zinc stearate (E)) (copied from [84]). 26

Fig. 1-24 Schematic of a typical pneumatic conveying system (copied from [85]). 28

Fig. 1-25 Illustration of Faraday cup technique for pneumatic conveying application (adapted from [89]). 29

Fig. 1-26 Illustration of charge measurement technique off a conveying line (copied from [89]). The conveying line passes through an internal copper cylinder connected to an electrometer while the outer cylinder is grounded. 29

Fig. 2-1. Schematic of the pilot-scale pressurized fluidization system. 47

Fig. 2-2. Schematic of the different locations that particles are present. 49

Fig. 2-3. The net specific charge of *Bulk* particles at different operating temperatures and pressures. 51

Fig. 2-4. The net specific charge of particles fouled in different regions of the column wall at various operating temperatures and (a) 101 kPa and (b) 2600 kPa. 51

Fig. 2-5. An example of particle layer formation on the column wall. 52

Fig. 2-6. Total amount of wall fouling and its distribution within the column at different operating temperatures. (a) 101 kPa and (b) 2600 kPa. 54

Fig. 2-7. Images taken from inner column wall at different operating conditions. The red arrow shows the *Fouling-bottom* layer (from the distributor plate up to the static bed height). (a) 101 kPa, low-range T, (b) 101 kPa, mid-range T, (c) 101 kPa, high-range T, (d) 2600 kPa, low-range T, (e) 2600 kPa, mid-range T, (f) 2600 kPa, high-range T. 55

Fig. 2-8. Cumulative charge of *Fines* measured at different operating conditions. 57

Fig. 3-1. A schematic of the apparatus inside the glove box filled with N_2, 1- Electrometer, 2- Faraday cup, 3- Shaker, 4- SS cup, 5- Coated cup, 6- PE particles. 65

Fig. 3-2. Volume resistivity cell and the connections. 1- Electrometer, 2- Current electrode, 3- Guard electrode, 4- Potential electrode, 5- A grounded copper cylinder that prevents any interference from environment. 67

Fig. 3-3 Current signal measurement over time from the volume resistivity measurement cell. Sample: LDPE film, temperature: 23°C, potential difference: 5000 VDC. 68

Fig. 3-4 The net specific charge of the PE particles shaken in the SS cup at different temperatures. 69

Fig. 3-5 The net specific charge of the particles shaken in the coated cup at different temperatures. 70

Fig. 3-6 Volume resistivity of various insulating films and PE resin at 23 and 60°C. 71

Fig. 3-7 Current versus time during volume resistivity measurements for LDPE film, (a) 23°C and (b) 60°C. The solid line shows the best curve fitted line based on Eq. (3-3). 73

Fig. 4-1. An example of chemical structure for a Phillips catalyst. 82

Fig. 4-2. An example of chemical structure for a silyl chromate catalyst. 83

Fig. 4-3. Schematic illustration of an example of mononuclear $TiCl_4$ (a) and active site precursors (b) on the (110) $MgCl_2$ supported on silica. 84

Fig. 4-4. An example of a typical MCN catalyst structure. A metal complex (a cation) on a metallocene catalyst. Silica is the catalyst base and methylaluminuxane (MAO) is the cocatalyst (an anion). 85

Fig. 4-5. Linear (a) and cage (b) structure of MAO. 85

Fig. 4-6. Silanol and siloxane groups on a silica support particle. 86

Fig. 4-7. Schematic of the atmospheric fluidization system, pneumatic conveying line, and measurement techniques. 90

Fig. 4-8. The net specific charge (Q/m) of various samples upon existing the conveying tube and entering the fluidized bed. 93

Fig. 4-9. Particle layer formation on a conductive wall of a fluidized bed. a) net charge of particles in the bed and the resulted induced charge on the fluidization column wall, b) first layer wall fouling formation due to the attractive force between the oppositely charged objects, c) second layer wall fouling formation where the attraction between particles is stronger than the repulsion between the bed particles and the wall, d) the second layer formation where the attraction between the particles and the column wall is stronger than the repulsion between similarly charged particles. 95

Fig. 4-10. The accumulative net charge of elutriated particles during fluidization period of 60 minutes, a) 100 ppm and b) 1000 ppm. (Please refer to the web version of this article for color interpretations in this figure). 97

Fig. 4-11. The amount of fouling (a), the net specific charge of Bulk (b) and Fouling-Bottom (c) for 0.1 g powder injections. 98

Fig. 4-12. The amount of fouling (a), the net specific charge of *Bulk* (b) and *Fouling-Bottom* (c) at 1000 ppm concentrations. 99

Fig. 4-13. The net charge of *Bulk* particles measured during their collection into the bottom Faraday cage when a) without the addition of Si, b) the bed contained 1 g of Si. 100

Fig. 4-14. The final mass of elutriated particles for PE and for when various powders were added to the bed, a) 100 ppm and b) 1000 ppm. 102

Fig. 5-1. Schematic of the pneumatic conveying apparatus with the electrostatic charge and two particle velocity measurement techniques. 118

Fig. 5-2. Images of the tested samples: (a) 0.1 g of glass beads, (b) 0.1 g of amorphous silica, (c) SEM of glass beads with 1000x magnification, (d) SEM of amorphous silica with 1000x magnification. 120

Fig. 5-3 FT-IR spectroscopy of the tested samples..... 120

Fig. 5-4. A typical electric current signal recorded by E_1 (glass beads, L = 3 m, and U_g = 15 m/s). 121

Fig. 5-5. An example of a silica particles observed in the transparent tube: (a) before injection when the transparent glass tube is clear, (b) upon injection and when the dilute and dense plumes appear. 122

Fig. 5-6. Various types of electric current signals captured from the pneumatic conveying line. (a) *signal Type-I* (glass beads, L = 3 m, U_g = 30 m/s); (b) *signal Type-II* (non-dehydrated silica, L = 3 m, U_g = 15 m/s); (c) *signal Type-III* (non-dehydrated silica, L = 3 m, U_g = 7 m/s); (d) *signal Type-IV* (dehydrated silica, L = 2 m, U_g = 7 m/s). 124

Fig. 5-7. The net specific charge of glass beads (a), non-dehydrated silica (b) and dehydrated silica (c) when conveyed at various conveying tube length and gas velocities. 126

Fig. 5-8. The $Q/m/L$ of glass beads (a), non-dehydrated silica (b) and dehydrated silica (c) tested at different conveying tube length and gas velocities. 127

Fig. 5-9. Comparison of particle velocity of glass beads (a), non-dehydrated silica (b) and dehydrated silica (c) at 7±1, 15±1 and 30±1 m/s gas velocities in 2 and 3 m in-length conveying tubes measured by the current signal and video imaging. 128

Fig. 5-10. U_p/U_g based on current signal technique for various conveying tube length and gas velocity. 130

Fig. 5-11. Estimated and measured particle velocity for non-dehydrated and dehydrated amorphous silica particles in the 2 m conveying line at various conveying gas velocities. 131

Fig. 5-12. Estimated and measured particle velocity for glass beads in the 2 m conveying line at various conveying gas velocities. 132

Fig. 5-13. An example of back flow observed for non-dehydrated amorphous silica particles at 15 m/s gas velocity in a 3 m in length tube. Direction of gas flow is from left to right. a) t<0 only air is passing through, b) t=0 s when the back flow is first seen, c) t=0.2 s, d) t=0.4s, e) t=0.6, f) t=0.8 s..... 133

Nomenclature

A	Surface Area, m^2
Ar	Archimedes number, -
C_D	Drag coefficient, -
D	Diameter of tube, m
D_{50}	Pipe diameter of 0.05 m
d	Gap between electrodes, m
d_p	Diameter of particle, m
E	Electric field, N/C
e	Electron Charge, C
F	Coulomb force, N
Fr	Froude number, -
Fr_t	Froude number at u_t, -
f_p	Friction factor, -
g	Acceleration of gravity, m/s^2
I	Current, A
k	Coulomb constant, $N.m^2/C^2$
k_b	Boltzmann constant, eV/K or J/K
L	Thickness, m
Q	Cumulative charge, C
q	Electric charge, C
R	Resistance, Ω
Re_p	Reynolds number of particles, -
r	Distance between two points in space, m
S	Specific gravity, -
T	Temperature, ºC
t	Time, s
t_0	Time at which particles start moving in the feeder, s
t_{in}	Time at which particles enter the conveying line, s
t_{out}	Time at which particles exit the conveying line

t_r	Residence time (s)
U_g	Superficial gas velocity, m/s
U_p	Particle velocity, m/s
u_t	Terminal velocity, m/s
V_C	Contact charge potential, V
ε	Void volume fraction, -
ρ	Volume resistivity, Ω.m
ρ_g	Density of gas, kg/m^3
ρ_p	Density of particle, kg/m^3
τ_1	Time constant, s
φ	Work function, eV, J

Acknowledgement

I am deeply grateful to the International Doctorate Scholarships program, sponsored by Canada's government, the collaborating organizations including Univation Technologies, LLC (USA) and the Natural Sciences and Engineering Research Council of Canada (NSERC), for granting me the opportunity to work on this project.

I extend my thanks to my supervisors Dr. Poupak Mehrani and Dr. Andrew Sowinski for their great support, insightful feedback, and valuable suggestions on this dissertation. I also appreciate the support and guidance provided by the Faculty of Engineering and its dedicated staff members at the Department of Chemical Engineering.

Lastly, I am indebted to my family and friends for their unwavering support throughout this challenging academic journey.

Chapter 1 – Introduction

Electrostatic charge generation is an inevitable phenomenon in many gas-solid processes including pneumatic conveying, fluidization, etc., resulting from contacts of solids with each other and/or with the neighbouring surfaces (e.g., wall of their containing vessel). Electrostatic charging of solids may result in undesired occurrences including particles agglomeration leading to changes in the process dynamics, particle fouling on adjacent surfaces necessitating cleaning and process shutdown, and electrostatic discharge creating an ignition source for fires or explosions. The adverse impacts of electrostatic charging have been reported in many industries such as petrochemicals, pharmaceuticals, etc [1–3]. One example of a commercial process that typically faces operational challenges due to electrostatics is polyethylene production. In this process, highly charged polyethylene and catalyst particles adhere to the gas-solid fluidized bed reactor walls and consequently result in a phenomenon known as *sheeting*. *Sheeting* could lead to reactor shut down due to a poor quality of fluidization, or blockages at the reactor distributor plate and/or product outlet. Loss of production and required maintenance in turn result in significant economic losses for the industry. Although much research has been carried over the past few decades to address this issue, the problem persists, necessitating a principal understanding of the sources that contribute the most to the generation of electrostatic charge and its adverse effects under industrially relevant operating conditions.

1.1 Electrostatic Charge Generation

When two solids contact each other, electrostatic charging can occur via three mechanisms: contact charging, frictional electrification, and induction charging. Contact charging occurs when two surfaces are brought into contact and separated (Fig. 1-1). For instance, consider two metal balls (one negatively charged, and one positively charged) that are isolated from environment. At the time of contact, charge transfer between surfaces happens in the fraction of time. Frictional electrification arises when two materials are rubbed against each other. Nevertheless, it is difficult to distinguish the occurrence of contact electrification from frictional electrification, thus the term *triboelectric charging* or *tribocharging* is generally used to describe both mechanisms [4–7].

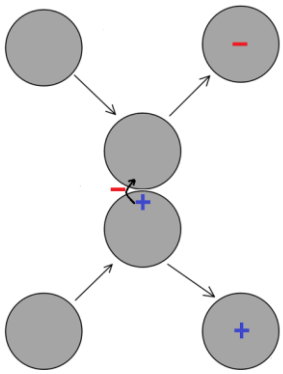

Fig. 1-1 Charge transfer between two solids as they approach each other, collide and separate.

Induction charging is a process in which a charged material (e.g., an insulator) gets close enough to a conductive material, which is neutral and isolated from the environment (Fig. 1-2). The electric field from the charged insulator will redistribute the electrons in the conductor such that the side closer to the charged insulator will gain the opposite polarity. If the conductive material is then grounded, electrostatic charge with the same polarity as the insulator will be discharged, leaving the conductive material with a net opposite polarity. In this case, the presence of a charged insulator in the vicinity of an isolated conductive material, attracts and holds the opposite charge on the surface of the conductive material with a force called *image force* [4].

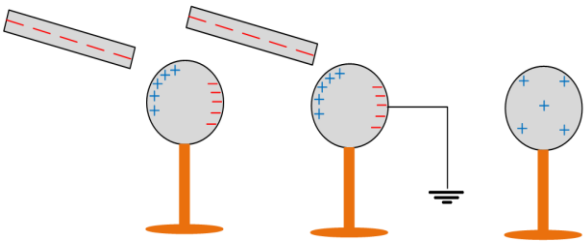

Fig. 1-2 Induction charging mechanism.

1.2 Conductors, Semiconductors, and Insulators

An atom is composed of neutrons, protons, and electrons. Protons and neutrons form the nucleus which is surrounded by electrons. According to the Bohr model, electrons are present in shells that represent their energy levels, and each shell can accommodate different numbers of electrons [8]. For a single atom, electrons are filled from the lowest to the highest energy level (Fig. 1-3). The electrons located in the outermost shell are called valence electrons. The highest energy range at 0 K occupied by valence electrons is called the valence band [8–10].

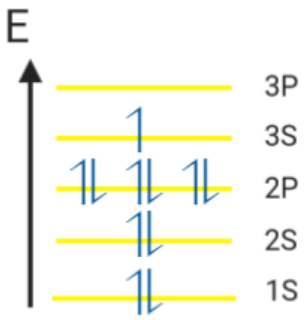

Fig. 1-3 Schematic of energy levels in one atom. E is the energy level of electrons, and yellow lines are the orbitals [8].

Electrons can be energized and enter the next available energy band where electrons are loosely bound to the atom and can move freely through the material. This energy band is called the conduction band. In the case of *conductive* materials where the valence band is not completely filled, the conductive band overlaps with the valence band, and as a result, a wide energy band is formed that enables electrons to easily acquire higher energies and be mobilized in a material (Fig. 1-4). However, in *insulators*, the valence band is completely filled, and the next available energy band is at higher energy levels. As a result, the electrons should have enough energy and be present at a higher energy band to move freely. The difference between the valence and conduction band is called *band gap* or *forbidden gap* and their energy difference is called *Fermi energy*. Band gap in insulator is high enough that even at room temperatures electrons cannot be present in the conduction band. Other materials that their band gap is not high so that there are few electrons in the conduction band, which are mobilized, are named semiconductors [8,10,11].

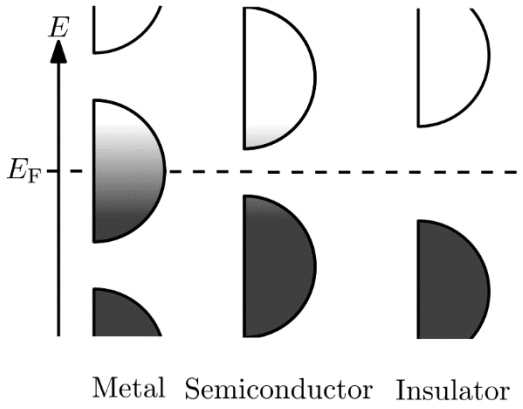

Fig. 1-4 Conduction band and valence band for metals, semiconductors and insulators. Black colour shows the electron density in each band. For metals, conduction and valence band overlap and electrons can easily move between two bands, whereas for insulators, valence band is fully occupied by electrons and to reach next available band (conduction band) high energy is required (copied from [11]).

Adding more electrons to a conductive material causes the free electrons within the material to repel each other such that excess electrons are evenly distributed on the surface of the conductor. In insulators, however, there are no free electrons and therefore, the excess electrons cannot move and are trapped in the material [12]. For semiconductors, the band gap is small so there are few electrons present in the conduction band that enable the semiconductors to flow electrons through themselves. By removing an electron from a semiconductor, the hole created can be filled by neighboring atoms and this phenomenon continues to happen within the material [12].

1.3 Charge Transfer Mechanisms

The underlying mechanisms for adding or removing electrons to or from materials has been discussed in several studies [13–17]. Depending on the type of the materials in contact, these mechanisms are categorized as metal-metal contact, metal-insulator contact and insulator-insulator contacts.

1.3.1 Metal-Metal Contact

The mechanism that is responsible for charge transfer between conductors is electron transfer. In this mechanism, electrons are transferred from one metal to another depending on the metal work function. Work function (φ) is the difference between Femi energy and the energy at vacuum level where an electron is removed and has no bond with the material. In other words, it is the minimum energy required to remove an electron from a solid to a point in vacuum. When two

metals with different work functions φ_1 and φ_2 are in contact, then the contact potential difference, V_c, is given by:

$$V_C = V_{1/2} = -\frac{\varphi_1 - \varphi_2}{e} \qquad \text{Eq. (1-1)}$$

Where $V_{1/2}$ is the contact potential difference of metal 1 against metal 2 and e is the elementary charge (1.602×10^{-19} C). According to this definition, the greater the work function, the higher energy you need to extract an electron from a material. Therefore, a metal with the lower work function (metal 1) is more willing to donate electron to a metal with a higher work function (metal 2), and after reaching an equilibrium, some electrons will be left on the metal with higher work function (Fig. 1-5) [14].

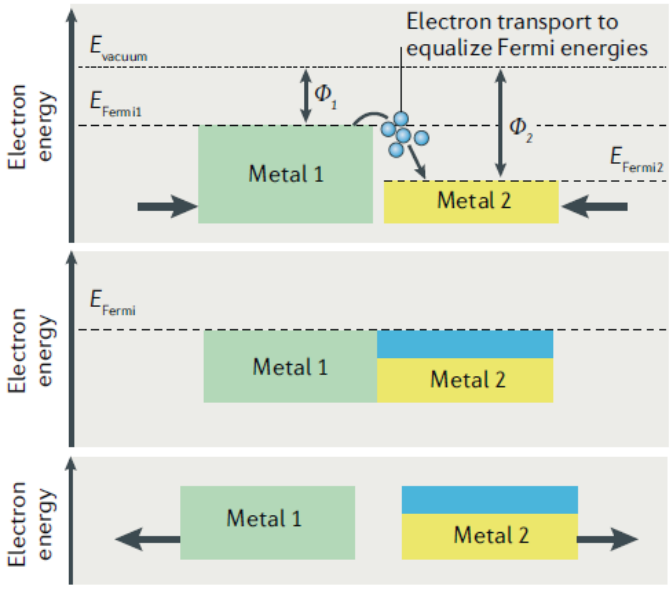

Fig. 1-5 Electron transfer illustration in metal-metal contacts (copied from [14]).

1.3.2 Metal-Insulator or Insulator-Insulator Contacts

As insulators lack free electrons and their valence band is full, their behavior in charge transfer is more complex. To explain the charge transfer as a result of contact, three mechanisms (electron transfer, ion transfer, and material transfer) have been proposed.

1.3.2.1 Electron Transfer

Although the electron transfer mechanism applies to metal-metal contacts, it may also occur in metal-insulator and insulator-insulator contacts. In these cases, a work function term needs to be assigned to insulators. For insulators, this term is called *effective work function* with the same definition used for conductors.

$$V_C = V_{1/2} = -\frac{\varphi_e - \varphi_m}{e} \qquad \text{Eq. (1-2)}$$

Where φ_e is the effective work function of insulator and φ_m is the work function of metal. As insulators lack conduction bands to transfer electrons, there are two possibilities that explain such phenomenon. The first possibility is the presence of surface defects (e.g., highly strained bonds) that act as an intermediate state between conduction and valence band to facilitate electron transfer [18]. However, the number of defects is not high enough to account for the charge transfer magnitude [15]. The other possibility is the delocalization of electron-wave functions that occurs after contacts. In other words, electron states on the surface of a material hybridize with those on the contacting surface. As a result, electrons delocalize and tunnel through the barrier [14] (Fig. 1-6)

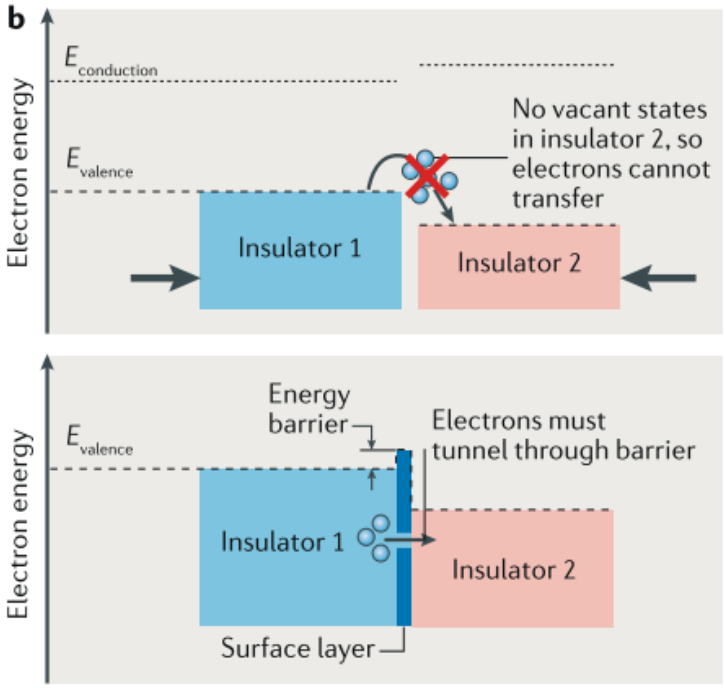

Fig. 1-6 Electron transfer illustration in insulator-insulator contacts (copied from [14]).

1.3.2.2 Ion Transfer

The charge carriers in this mechanism are ions. As illustrated in Fig. 1-7, an ion is considered as a charged atom or molecule since the number of electrons is not equal to the number of protons. In this mechanism, mobile ions which are loosely bound to the ionic materials dissociate and sit on the contacting material [13,14,16,19–22].

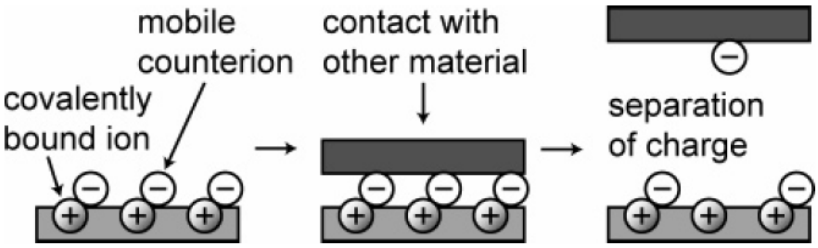

Fig. 1-7 Schematic illustration of ion transfer mechanism (copied from [23]).

Moreover, it has been proposed that surface of materials can lose and donate OH^- and H^+ groups for charge transfer according to their pK_b (a factor to determine the strength of a base) [24]. This means that materials basic in nature are more likely to adsorb positive charges and vice versa. Even for non-ionic polymers, OH^- and H^+ ions are assumed to come from environment. The moisture present in the environment or on the surface of a material carry excess charge which

can be adsorbed or desorbed, and result in charge accumulation or dissipation on the insulator surface [25]. Furthermore, it has been claimed that adsorption of water molecules increases the surface conductivity of materials, and thus improves charge transfer [16].

1.3.2.3 Material Transfer

The collision and friction between two bodies can result in a transfer of fractured materials or impurities on the surfaces. In such cases, the charge of the transferred material is added to the net charge of the contacting material (Fig. 1-8a) [17,26,27]. Baytekin et. al [28] observed that the contact surface of the materials becomes significantly rougher after shaking. In addition, in their work Quantitative Nanomechanical Property Mapping (QNM) atomic force microscopy identified patches of the contacting materials on each other. In another work, Pandey et. al [27] suggested that bond cleavage during contact results in charge generation; and transfer of these fractions leads to a significance charge transfer (Fig. 1-8b).

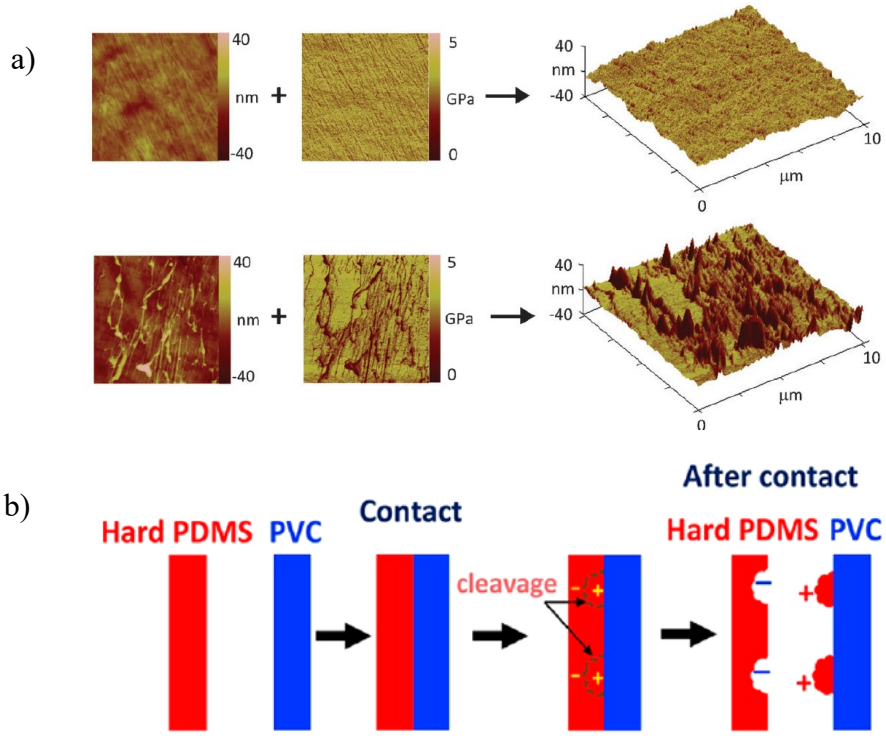

Fig. 1-8 Schematic illustration of material transfer between two materials, a) AFM height and AFM-Peakforce QNM DMT modulus maps before (top) and after (bottom) contact (PTFE spheres shaken in PS dishes) show PTFE on PS surface (copied from [28]), b) Transfer of material after bond cleavage (copied from [27]).

1.3.3 Triboelectric Series

A triboelectric series lists materials to show the empirical direction of charge transfer. In such lists, a material that has a higher location in the table acquires positive charge if it contacts with lower located materials (Fig. 1-9a) [4,29]. However, this method has shown inconsistency in some cases [17,18,30]. For instance, experiments show a cyclic triboelectric series for silk, glass, zinc, paper and cotton rather than a linear one (Fig. 1-9b) [16,31,32]. In addition, charge polarity of materials may alter by having different surface finish, shape, purity, and humidity [4,18,29,30]. The unpredictable nature of triboelectric charging and the disputable proposed mechanisms is one of the reasons why it has been extensively studied.

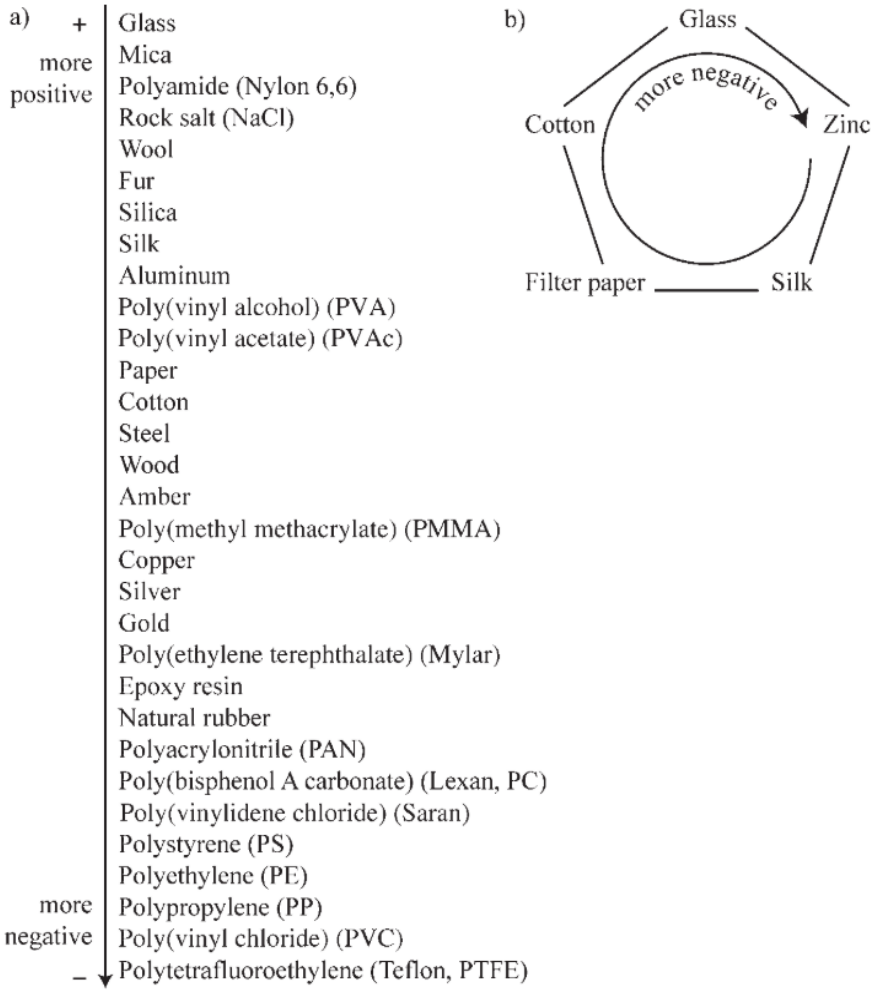

Fig. 1-9 a) An example of a linear triboelectric series, b) An example of a cyclic triboelectric series (copied from [16]).

1.4 Charge Measurement Techniques

A basic concept in physics explains that two point-charges impose a force called *Coulomb force* ($\vec{F}$) on one another (Fig. 1-10), which can be calculated by the following equation.

$$\vec{F} = \frac{kq_1q_2}{r^2} \qquad \text{Eq. (1-3)}$$

Where k is the Coulomb's constant ($k = 8.9879\text{x}10^9$ N.m^2/C^2), q is the magnitude of the charge in Coulombs (C) (which is equal to -6.24151x10^{18} electrons or 6.24151x10^{18} protons) and r is the distance between the charges in meters. The interaction force is attractive if the sign of F is negative (charges are in opposite polarity) and repulsive if F is positive (charges are in same polarity).

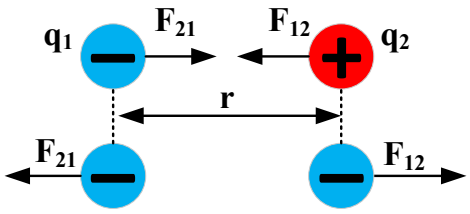

Fig. 1-10 Coulomb force between two point-charges.

Electric field ($\vec{E}$) is also defined as a property in the vicinity of a charge q_0 that exerts force on other charges in the field (Fig. 1-11). The intensity of an electric field at a point is the electric force exerted per unit positive electric charge q at that point.

$$\vec{E} = \frac{\vec{F}}{q_0} = \frac{kq_0q}{q_0r^2} = \frac{kq}{r^2} \qquad \text{Eq. (1-4)}$$

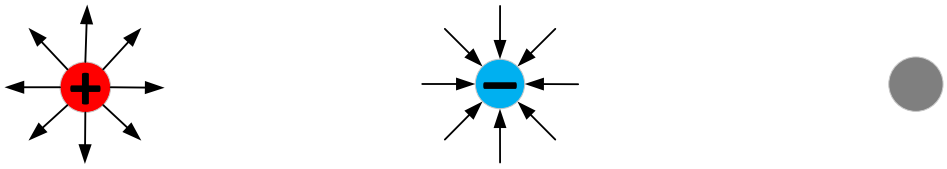

Fig. 1-11 Electric field in the surrounding of a positive, negative, and neutral particle.

Electric field concept has been implemented in different devices to measure the charge of materials. Almost all devices can be categorized into two groups: Faraday cups and electrostatic probes.

1.4.1 Faraday Cups

A Faraday cup is composed of two metal shells, as such that the inner shell is isolated from environment by an outer shell with an insulator (Fig. 1-12). The outer shell is grounded to prevent any external electric field to affect the measurement. Upon entrance of any charged material to the inner shell, the electric field resulted from the material attracts the opposite polarity charge on the inner walls of the inner shell and repels the same polarity to its outer wall (image force). Since the electrometer that is connected to the inner shell is grounded, the same polarity charge leaves the system and is read by the electrometer. Therefore, electrometer reads the same polarity and charge of the material inside a Faraday cup [4].

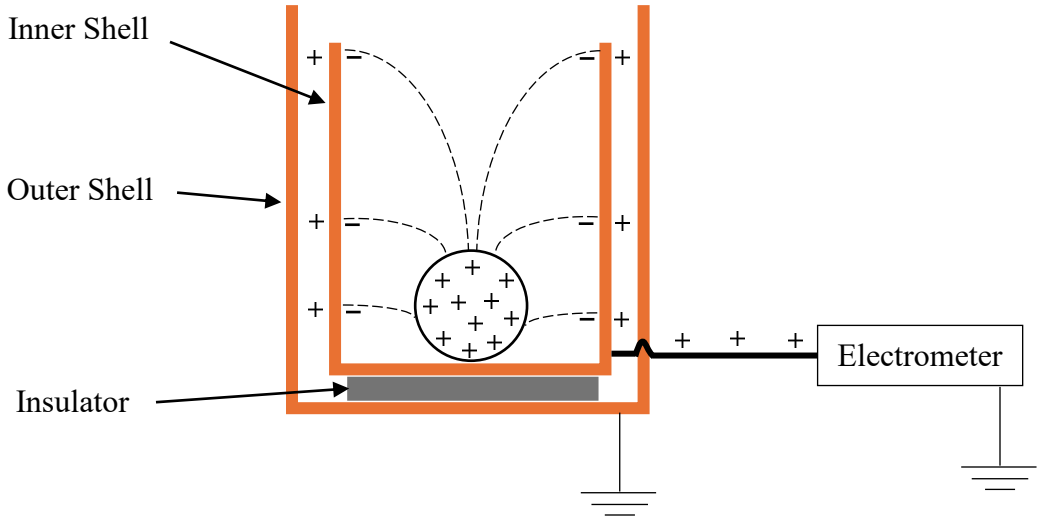

Fig. 1-12 Schematic showing how a Faraday cup measures the charge of a charged object.

A Faraday cup only measures the net charge of the material placed inside it. For instance, in the presence of several particles that would have different charge magnitudes and polarities, the sum of the charges will be measured. As well, any charge generation within the Faraday cup due to particle-particle and particle-wall contacts is not measured since the net charge of both positive and negative charge transfer is zero.

1.4.2 Electrostatic Probes

In 1960s, Ciborowski and Wlodarski [33] immersed a small metal ball in a fluidized bed with a thin platinum wire connected to an electrometer. This is the first study that aimed to measure electrostatics in gas-solid fluidized beds via electrostatic probe. Based on the concept behind this measurement technique, a real charge induces an image of itself onto a conducting surface such as stainless steel. In general, electrostatic probes consist of a conductive bar or wire, an insulating layer, and a grounded outer layer (Fig. 1-13). The other end of the probe (i.e., the conductive inner bar) is connected to an electrometer in order to measure the induced charge in form of electric potential, field, or current signals.

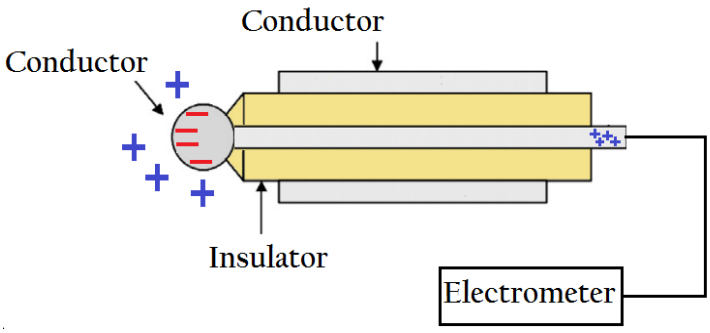

Fig. 1-13 Components of an electrostatic probe.

One disadvantage of this technique in the case of usage in granular type system, is that charged particles could stick to the tip of the probe due to electrostatic force, causing reduction in the actual potential read by the probe [34]. As well, since this technique is operated *in-situ,* the contacts with the charged particles might introduce extra charge and, in return, makes it problematic to distinguish between the charge induced by the surrounding particles and the charge generated as a result of particle-probe contacts. Moreover, this technique only measures the local charge in close proximity of the probe which is not a good representative of the electrostatic charge of all particles in a large system. The probe potential is also inversely related to the capacitance of the probe, which adds on more difficulties with this technique since the capacitance depends on geometric factors including the size and location of the probe, signal wires, the dimensions, and materials of the column. Furthermore, it could result in changes in hydrodynamics of a system due to the intrusion of the probe [35,36].

1.5 Gas-Solid Fluidization

The first industrial application of gas-solid fluidization technology goes back to 1942 with catalytic cracking process [37]. Since then, this technology has been used in wide variety of industries such as agriculture, oil and gas, pharmaceutics, petrochemical, etc.

In a gas-solid fluidized bed, the fluidizing gas is introduced from bottom of the column which then reaches a bed of particles after passing a distributor plate. By increasing fluidizing gas velocity, different flow regimes will take place (Fig. 1-14). At a low gas velocity where the gravitational force prevails drag and buoyant forces, the particles bed height remains at the static bed height. When the gas velocity is high enough so that the drag and buoyant forces balance the gravitational force, the particles enter a fluidized state. This is the point of minimum fluidization, and the superficial gas velocity at this point is referred to as minimum fluidization velocity (U_m). At velocities higher than $U_{mf,}$ the excess gas forms bubbles at the distributor, which grow, rise, and finally burst at the bed surface (referred to as bubbling flow regime). If the gas velocity increases even higher, the bubbles will grow larger in diameter, even becoming close or equal to the diameter of the column which is the point at which the slugging flow regime is reached [37]. Turbulent fluidization happens when the fluidization gas velocity is large enough such that it becomes difficult to detect the top surface of the bed and fine particles entrainment becomes significant [38]. Finally, at very high gas velocities, and especially for those cases with very small particles, fast fluidization and pneumatic transport regimes are achieved. This research will involve a bubbling flow regime.

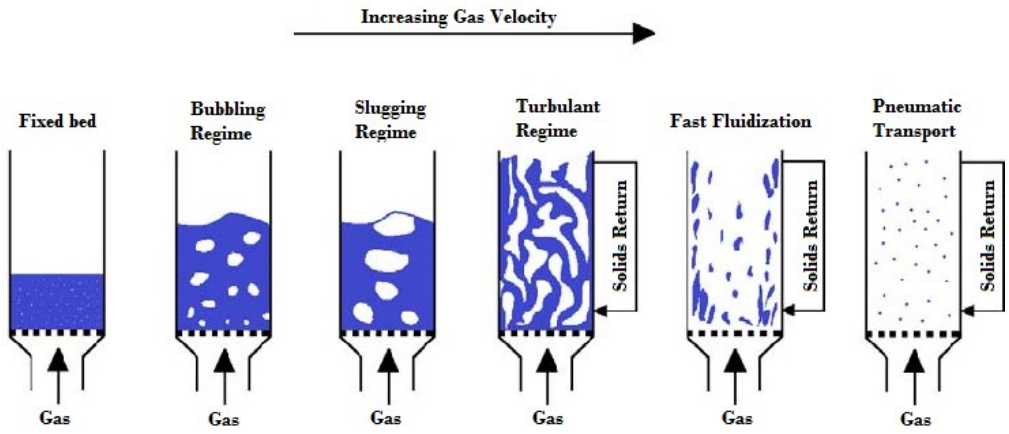

Fig. 1-14 Different flow regimes by increasing fluidization gas velocity (copied from [39]).

Geldart [40] classified the fluidization behavior of different particles based on their size and density (Table 1-1). Fine particles (referred to as group C) are known to be more cohesive due to high attractive forces (Van der Waals forces, electrostatics, or moisture), therefore they are not easily fluidized. For this group of particles, either fluidizing gas channels within the bed or portions of the particles rise as a plug. Group A particles are larger in size and/or density, and thus, less interparticle forces exist. The main characteristic of these particles is no gas bubble generation at minimum fluidization velocity. Groups B and D consist of larger and denser particles where interparticle forces become negligible. At minimum fluidization velocity, for group B particles gas bubbles are generated, while group D particles are difficult to fluidize and used in spouted beds. The solids used in this research fall under the Geldart group B particles.

Table 1-1 Geldart classification of particles [40].

Geldart group	Particle size (μm)	Particle-gas density difference (g/cm^3)	Features
A	20-100	Less than 1.4	Aeratable, Different minimum fluidization and bubbling velocity
B	40-500	1.4 – 4	Sandlike, easy to fluidize, Same minimum fluidization and bubbling velocity
C	Less than 60	Less than 1.4	Cohesive, difficult to fluidize
D	Above 600	Above 1.4	Spoutable, difficult to fluidize

An industrial application of gas-phase fluidization technology is in catalytic polymerization of ethylene to produce polyethylene (Fig. 1-15). In these reactors, the catalyst particles are periodically injected into the fluidization column using an inert gas such as nitrogen. The fluidizing gas, ethylene, along with the co-monomers (e.g., 1-octene, 1-hexene, and 1-butene) enter the reactor below the distributor plate and react with the active catalyst in the reaction zone. The exothermic polymerization reaction then occurs on the catalyst with polymer chains growing on the particle. To prevent runaway reactions, heat removal is achieved by cooling the recycle gas stream, whose flow rate is 50 times greater than the make-up gas, to a temperature below the desired polymerization temperature (referred to as gas phase mode). The rate of heat removal can be further enhanced by reducing the recycle gas temperature enough to form a stream composed

of liquid and gas. The recycle stream is then introduced into the fluidized bed reactor where the liquid portion vaporizes and removes the heat generated in the reactor (referred to as condensed mode). The final product is a polyethylene resin that encapsulates the spent catalyst at its center. The produced polyethylene resins are continuously removed from the reactor close to the distributor plate [41]. Polyethylene reactors are operated under steady-state condition with operating pressures and temperatures ranging from 1800 to 2400 kPa and 80 to 110ºC, respectively [42].

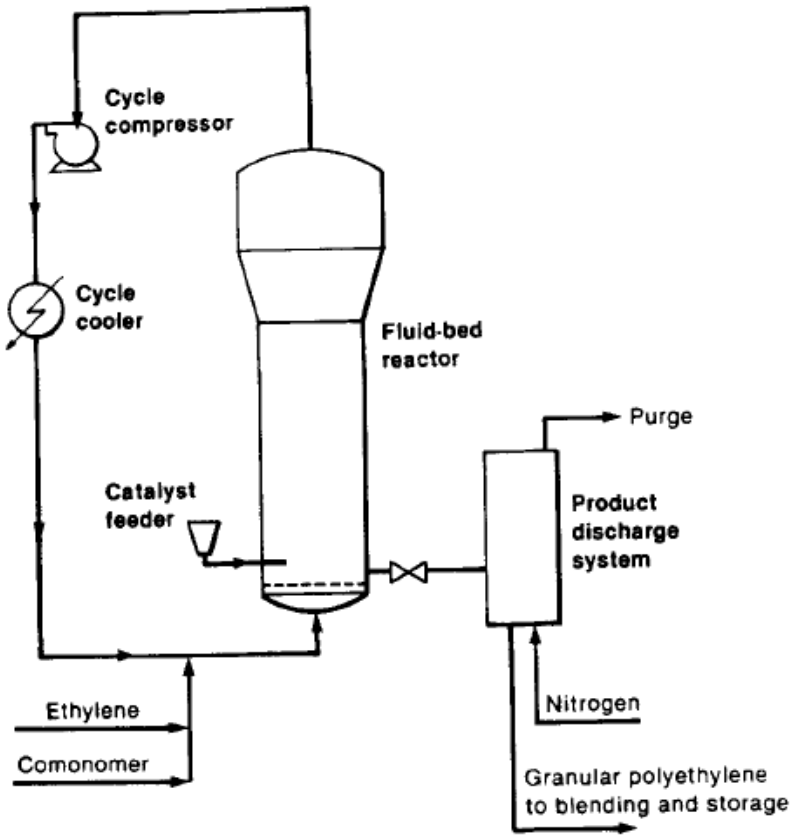

Fig. 1-15 Schematic of a polyethylene fluidized bed reactor (copied from [43]).

1.6 Polymerization Catalysts

Depending on the desired end product (e.g. high density, low density, extrusion grade, etc.) an appropriate catalyst is utilized from the five categories listed below [44]:

1- Silyl Chromate
2- Bis(cyclopentadienyl) + a transitional metal (*a **Metallocene***)
3- Chromium or titanium oxides

4- A mixture of a titanium compound, a magnesium compound, an electron donor compound which is a liquid Lewis base, and an activator compound (***Ziegler-Natta***)
5- Vanadium based catalysts.

Phillips Petroleum developed a commercial process for the heterogenous chromium catalyst discovered in 1951. Phillips catalyst is capable of producing high-density polyethylene (HDPE) as the most widely used form of polyethylene. This catalyst yields the broadest molecular weight (MW) distribution and exhibits a more pronounced shear thinning effect than that observed with other catalysts. Typically, Phillips catalysts are supported on silica, which undergoes impregnation with a chromium compound. Subsequently the catalyst becomes activated by calcination in dry air or oxygen. The chemical structure of this catalyst is depicted in Fig. 1-16 [45,46].

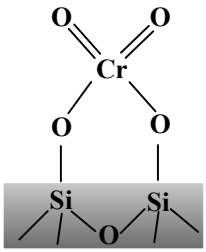

Fig. 1-16. An example of chemical structure for a Phillips catalyst.

Silyl chromate catalysts were initially developed by the Union Carbide Corporation (UCC) to produce HDPE using a gas-phase UNIPOL^{TM} process. The silyl chromate catalysts yield polymer distributions that are broad, extending to both high and low molecular weight ranges and featuring a distinctive high molecular weight tail which indicates a potential second type of active site. This catalyst can be supported on silica, and its chemical structure is illustrated in Fig. 1-17 [45,47].

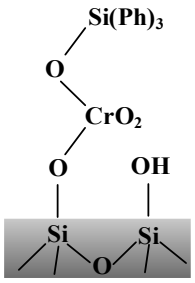

Fig. 1-17 An example of chemical structure for a silyl chromate catalyst.

Another type of catalyst widely used in PE production is Ziegler-Natta (ZN) catalysts. They possess multiple active sites, each with distinct characteristics such as propagation rates, comonomer reactivity ratios, and stereoselectivities. In general, heterogeneous catalysts are usually supported on silica, aluminum oxide or magnesium chloride to increase the surface area available for polymerization reaction. Furthermore, cocatalysts are added to increase the activity of catalysts. Heterogeneous ZN catalysts consist of titanium trichloride ($TiCl_3$), or titanium tetrachloride ($TiCl_4$) supported on magnesium chloride ($MgCl_2$), aided by cocatalysts like triethylaluminum ($AlEt_3$). Magnesium chloride stands out as the optimal support material due to its close resemblance in atomic size, shape, and coordination number to titanium [48]. To enhance stereo control in the propylene polymerization process, Lewis bases, such as ethyl benzoate, silanes, or other donors, are also introduced into the reactor [49]. Titanium tetrachloride catalysts, when directly bonded to oxide supports like silica or alumina, exhibit limited effectiveness in polymerization [50]. A silica/$MgCl_2$ support offers a solution by providing precise particle size control while maintaining the beneficial properties of an $MgCl_2$ base, crucial for controlling particle morphology [51]. Studies [52–60] show that $TiCl_4$ and $TiCl_3$ possess various actives sites on different lattice planes of $MgCl_2$. Fig. 1-18 shows just on example of mononuclear $TiCl_4$ on (110) $MgCl_2$ and its alkylation by $AlEt_3$ [53].

a)

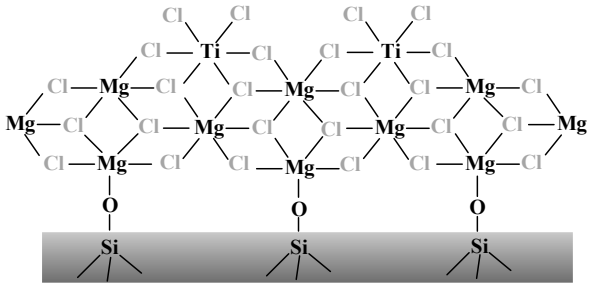

b)

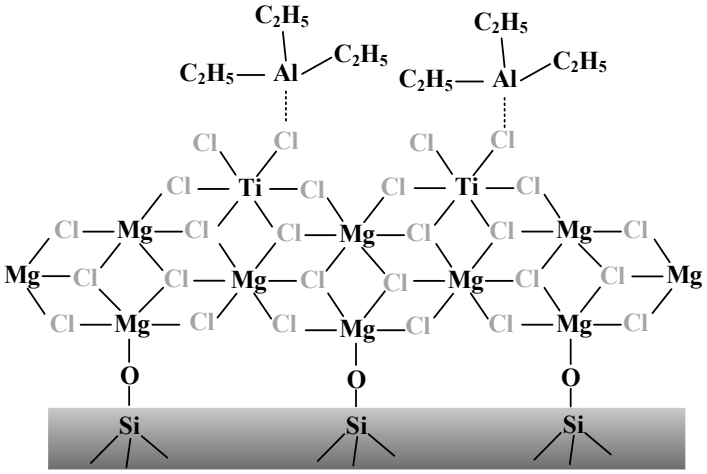

Fig. 1-18. Schematic illustration of an example of mononuclear $TiCl_4$ (a) and active site precursors (b) on the (110) $MgCl_2$ supported on silica.

The characteristics and chemical formula of a heterogeneous metallocene catalyst will be discussed in Chapter 4.

1.7 Electrostatics in Gas-Solid Fluidized Beds

Due to the nature of a fluidization process, particle-particle and particle-fluidization column wall collisions are inevitable which result in electrostatic charging of the fluidizing particles. Depending on its extent, the electrostatic charge built up could then cause considerable operational challenges such as particle agglomeration and accumulation on the reactor walls. Such adverse effects can be seen in some commercial processes including gas-phase polymerization fluidized bed reactors. In such reactors, electrostatically charged catalyst and polyethylene particles migrate to the reactor wall, and thus, the exothermic reaction occurs in the absence of the heat removal, resulting in hot spots on the reactor wall. These hot spots then cause

the polyethylene particles to melt and fuse together and lead to formation of *wall sheets* in various locations (e.g., in the fluidization region, expanded section or dome) of the reactor as shown in

Fig. 1-19a. According to Fulks et al. [41] sheets vary in size with a thickness ranging from 0.006 to 0.013 m, length of 0.30 to 1.5 m and width of 3.6 to 5.5 m. Depending on the source particles that accumulate on the reactor wall, sheets are categorized either as *warm sheets* or *cold sheet*. Warm sheets are formed when catalyst particles adhere to the reactor wall, resulting in wall temperature to increase due to polymerization reaction. The wall temperature then decreases as the sheet thickens and the reaction zone moves away from the wall. These sheets are composed of an inner core with granular polymers fused on the surface of the core and orientated in the direction of the long sheets with a hairy appearance at their edges. However, cold sheets are formed by the polymer particles accumulating on the reactor wall. Polymerization continues slowly in these particles, and when the temperature reaches the sintering temperature, sintered sheets are created without building the orientated strands of polymers as seen in warm sheets [1,44].

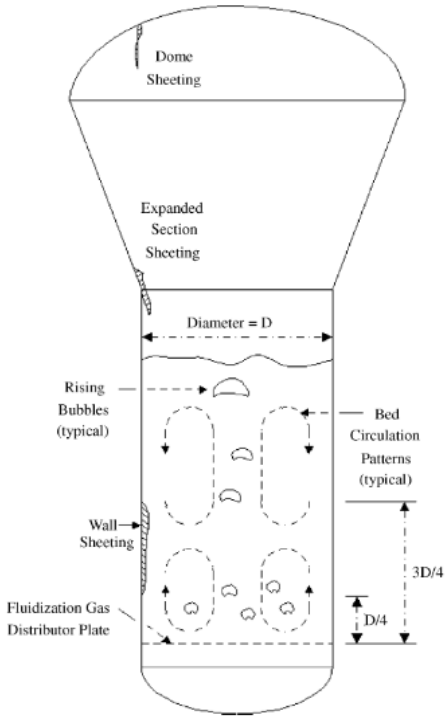

Fig. 1-19 Locations that sheeting may occur in a commercial polyethylene reactor (copied from [1]).

As the sheets grow, they could separate from the reactor wall, fall, and accumulate on the distributor plate, causing a reduction in fluidization quality by blocking the distributor plate and making dead zones. In some cases, reactor shutdown for cleaning would then be required which in turn results in significant economic losses due to loss of production and maintenance costs. For instance, a reactor shutdown in Dow Canada linear low-density polyethylene (LLDPE) production plant in Alberta, with an approximate production capacity of 500,000 ton/yr, will result in approximately 2 million USD/day loss. Depending on the severity of sheeting, reactor shutdown for cleaning may take up from one to several months.

To address the issue of sheet formation in commercial polyethylene reactors, several techniques have been applied including treating the reactor wall surface with a chromium containing compound to reduce static electric generation, as well as injection of continuity additives (previously known as antistatic agents) [41,42,61]. Nevertheless, most of the techniques are found to be applicable for only some types of catalysts (e.g., Ziegler-Natta catalysts) and not for recent growing metallocene based catalysts which enable synthesis of polymers more desired properties [41,42,49,61,62]. The most common method applied to reduce sheeting is the addition of static control agents such as *aluminum distearate* and *ethoxylated stearyl amine* (also known as *AS-990* with IUPAC name of *2,2'-(octadecylimino)bis[ethanol]*) to the reactor during operation. These continuity additives are hypothesized to help control static by reducing or eliminating electrostatic charge buildup on the surface of the materials by increasing their ionic conductivity (the tendency of an ion to move from one site to another) or electronic conductivity [63,64].

As suggested by Song & Mehrani [65], the mechanism for formation of wall fouling (the adhesion of particles to reactor wall) can be explained by the attractive and repulsive forces caused by image and Coulomb forces between the electrostatically charge fluidizing particles and the metallic column wall as shown in Fig. 1-20.

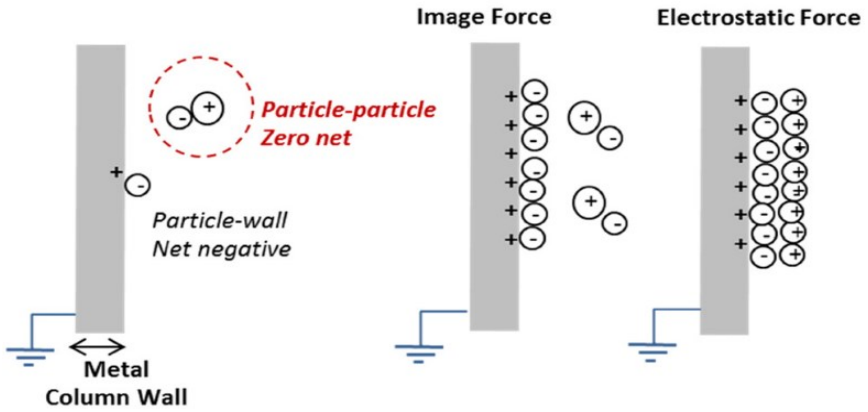

Fig. 1-20 Mechanism proposed for wall fouling formation (copied from [65])

Fluidizing PE particles in contact with the metallic wall build a negative polarity electrostatic charge. This net negative polarity in the fluidizing particles would induce an image of the charge (of opposite polarity) on the column wall, resulting in accumulation of the negatively charged particles on the wall. Subsequently, the Coulomb force originated by the first layer on the wall, attracts or repels the particles with an opposite or same polarity, respectively. Therefore, depending on the magnitude of the Coulomb force different layers of particles will form on the wall.

1.7.1 Effect of Fluidization Operating Conditions

To better understand the mechanisms of charge generation and in turn wall fouling in gas-solid fluidized beds, several works have focused on studying the influence of various fluidization operating conditions. The fluidization gas type and velocity, particle size, and operating pressure are expected to be quite influential due to their effect on the fluidization hydrodynamics. Operating pressure is found to have a direct relationship with bed electrification by influencing bubble rise velocity, frequency, and volume fraction [66,67]. Gas velocity is also one of the parameters that has been most reported to increase electrostatic charge built up due to increase in bubble size and rise velocity, in turn resulting in more mixing and collisions inside the bed [34,66,68–71]. The maximum charge build-up on a surface of a particle depends on the breakdown voltage of the gas. Results have shown that using argon can substantially reduce the amount of fouling in a polyethylene fluidized bed [72]. Excluding parameters that affect fluidization hydrodynamics, fluidizing particle and column wall material, gas relative humidity and temperature are also found to play an important role [73–76].

1.8 Effect of Temperature

Among all aforementioned parameters, the influence of temperature has received minimum attention, and contradicting results have been reported [77,78]. In relation to the influence of temperature on the electrostatic charging behavior of solids at the fundamental level with no reference to fluid beds, a few bench-scale works have been reported [77–80]. Jantac et al. [77] examined the triboelectrification of polyethylene particles in a shaker or on a slide at two temperatures of 22 and 90°C. They concluded, without any measurement support, that at higher temperatures, polyethylene particles were assumed to be softer, and thus, their contact surface area increased during collisions, resulting in a higher charge generation. Greason [78] tested the triboelectrification of a metallic sphere in a cylinder made of different insulators and proposed that the volume and surface resistivity of insulators could experience a decline as temperature increases, resulting in an increase in the charge leakage to the ground and a less charge buildup on the surface. Harris et al. [79] investigated the triboelectrification of a nylon and a PTFE plate when the two insulator plates had contacts with each other and suggested a similar theory as Greason. Both studies did not confirm their theory through resistivity tests at different temperatures. Lin et al. [80] investigated the effect of temperature on charge transfer between a metal and an insulator by using atomic force microscopy (AFM) and Kelvin probe force microscopy. The metal was the cantilever of AFM, and the insulators were a thin film of SiO_2, AlN, polyvinyl chloride (PVC) and polymethyl methacrylate (PMMA). They found that the material with a larger value of the summation of Fermi energy (which is at 0 K) and the energy of electrons (which is $\sim k_b T$ at a given temperature, k_b is Boltzman constant) was labeled as an electron donor. This finding by Lin et al could imply that temperature can facilitate the transfer of electrons from a material by increasing the energy level of electrons. Further details about the aforementioned studies will be discussed in Chapter 2.

With respect to gas-solid fluidization process, only two studies have been found in open literature studying the influence of operating temperature on fluid bed electrification. Moughrabiah et al. [66] used collision ball probes to measure the cumulative charge of 600 μm (LLDPE) particles at different axial locations inside a stainless-steel fluidization column. At the operating condition of 60°C and 379 kPa, their results showed that the degree of cumulative charge generation on the particles was significantly less than that at 20ºC. The same team in their second work [81] evaluated the electrostatic charging of a mixture of fine (25-50 μm) and large

(425-600 μm) glass beads at 414 kPa while varying the temperature from 20°C to 75°C. They showed that by increasing temperature, electrostatic charge measured at different locations of the bed decreased, and for temperatures above 70°C, a polarity change was observed. In the same study, the authors also observed that the charge of entrained glass beads declined as the temperature increased while the mass flux of the particles did not have a noticeable change. The two aforementioned studies used electrostatic probes with a very short measurement period of 500 s and had no means of measuring the extent of LLDPE or glass beads wall fouling. In addition, they did not provide a discussion on reasoning behind observing a decline in the degree of charge generation at higher temperatures.

1.9 Effect of Solid's Surface Chemistry

Contact electrification is a phenomenon that takes place on the surface of the materials at the point of contact. Therefore, surface chemical composition is expected to influence the sign and magnitude of a material final charge [13]. Some researchers assume that electron transfer is still involved in contact electrification of insulators based on the work function of the different materials. The energy required for an electron to be separated from one material and transferred to another material is the energy difference between the highest occupied molecular orbital (HOMO) and lowest unoccupied molecular orbital (LUMO), or in other words, the band gap. This energy is typically in the order of several eVs which cannot be satisfied at room temperature ($k_bT \approx 0.026$ eV). Therefore, it is anticipated that ion transfer to be the main mechanism to transfer charge if the insulator is ionic. Based on this premise, the charge polarity can be manipulated by mobilizing or immobilizing one of the ions on the surface. For instance, in an ionomer which is a polymer with ionic side groups, one ion is covalently bonded to the polymer, while the accompanying counterion can be mobile (Fig. 1-21).

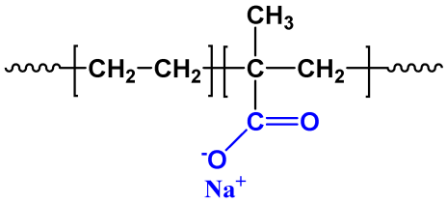

Fig. 1-21 Chemical structure of an ionomer (poly(ethylene-co-methacrylic acid)) with an immobile anion covalently bonded to the backbone of the polymer and a mobile cation (copied from [82]).

McCarty and Whitesides [16] synthesized polystyrene and glass microspheres that contained different mobile ions and covalently bound cations. They observed that after contact with aluminum the polarity of the microspheres was consistent with the ion transfer mechanism in which microspheres acquired the same polarity as their immobile ion (Fig. 1-22).

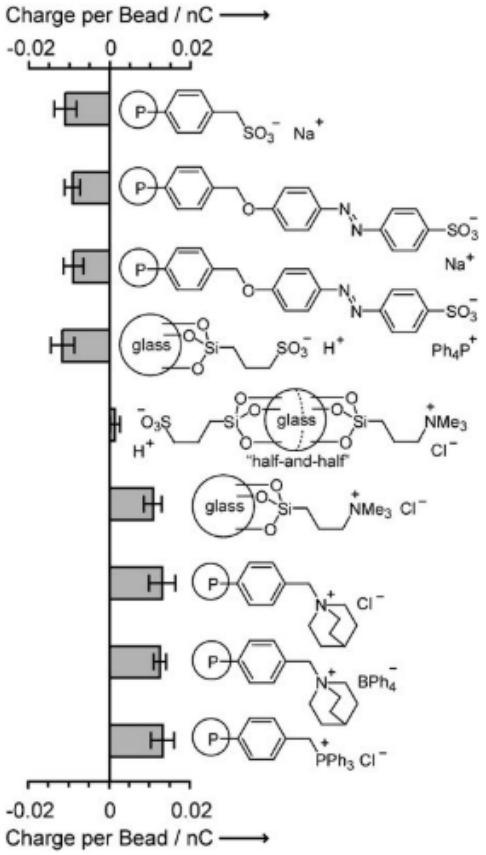

Fig. 1-22 Electrostatic charge of functionalized polystyrene or glass microspheres (200 mm in diameter) after contact electrification with aluminum (copied from [16]).

These results illustrate that the surface chemistry of materials plays a significant role in contact electrification. As discussed earlier in relation to the polyethylene process, catalysts and continuity additives are also present in the reactors, which necessitate further study on the role of their chemistry in electrostatic charge generation in such process. Majority of works investigating electrostatic charging in relation to polyethylene gas-phase reactors have only considered the charging behavior of polyethylene alone. The only work reported in literature that studied the role of presence of catalyst on electrostatic charge generation of polyethylene resin is a prior work from our group by Sowinski & Mehrani [83]. They conducted a preliminary study

on the effect of injection of a deactivated metallocene catalyst and an amorphous silica, being the catalyst support, into a polyethylene fluidized bed. In their study, it was concluded that the existence of such charged particles as a result of their injection promoted polyethylene resin fouling on the column wall.

Six years ago, our group initiated a research program that was focused on understanding the triboelectrification of pneumatically conveyed solids including commercially used catalysts and their support, as well as continuity additives. The first phase of this research was completed by the former PhD candidate, Milad Taghavivand [84] whose work focused on studying the role of amorphous silica, as a typical catalyst support, and several commercially available continuity additives. Amorphous silica was tested in its non-dehydrated and dehydrated (i.e., calcined to 600ºC) forms. The continuity additives tested included aluminum distearate, AS-990, calcium stearate, zinc stearate, and CHIMASSORB 944[1]. Taghavivand's work was also focused on determining the role of these solids on the degree of polyethylene fluidized bed wall fouling. It was hypothesized that the magnitude of the wall fouling would depend on the charge magnitude of these solids upon entering the fluidized bed through pneumatic conveying line. Regardless of the initial charge of the tested solids entering the fluidized bed, solids with non-ionic surfaces developed either negative polarity (i.e., dehydrated and non-dehydrated silica particles) or positive polarity (i.e., AS-990 and CHIMASSORB 944), depending on their proton affinity. The ionic surfaces based on the functional groups in their chemical structure resulted in positive polarity (e.g., aluminum distearate) or negative polarity (e.g., calcium stearate) in the bed. As shown in Fig. 1-23, it was found that depending on the net charge of particles inside a polyethylene fluidized bed, the addition of positive or negative inducing solids will influence the net specific charge of the fluidizing particles, and subsequently the amount of wall fouling [84].

[1] IUPAC name: Poly[[6-[(1,1,3,3-tetramethylbutyl)amino]-1,3,5-triazine-2,4-diyl][(2,2,6,6- tetramethyl-4-piperidinyl)imino]-1,6-hexanediyl[(2,2,6,6-tetramethyl-4- piperidinyl)imino]])

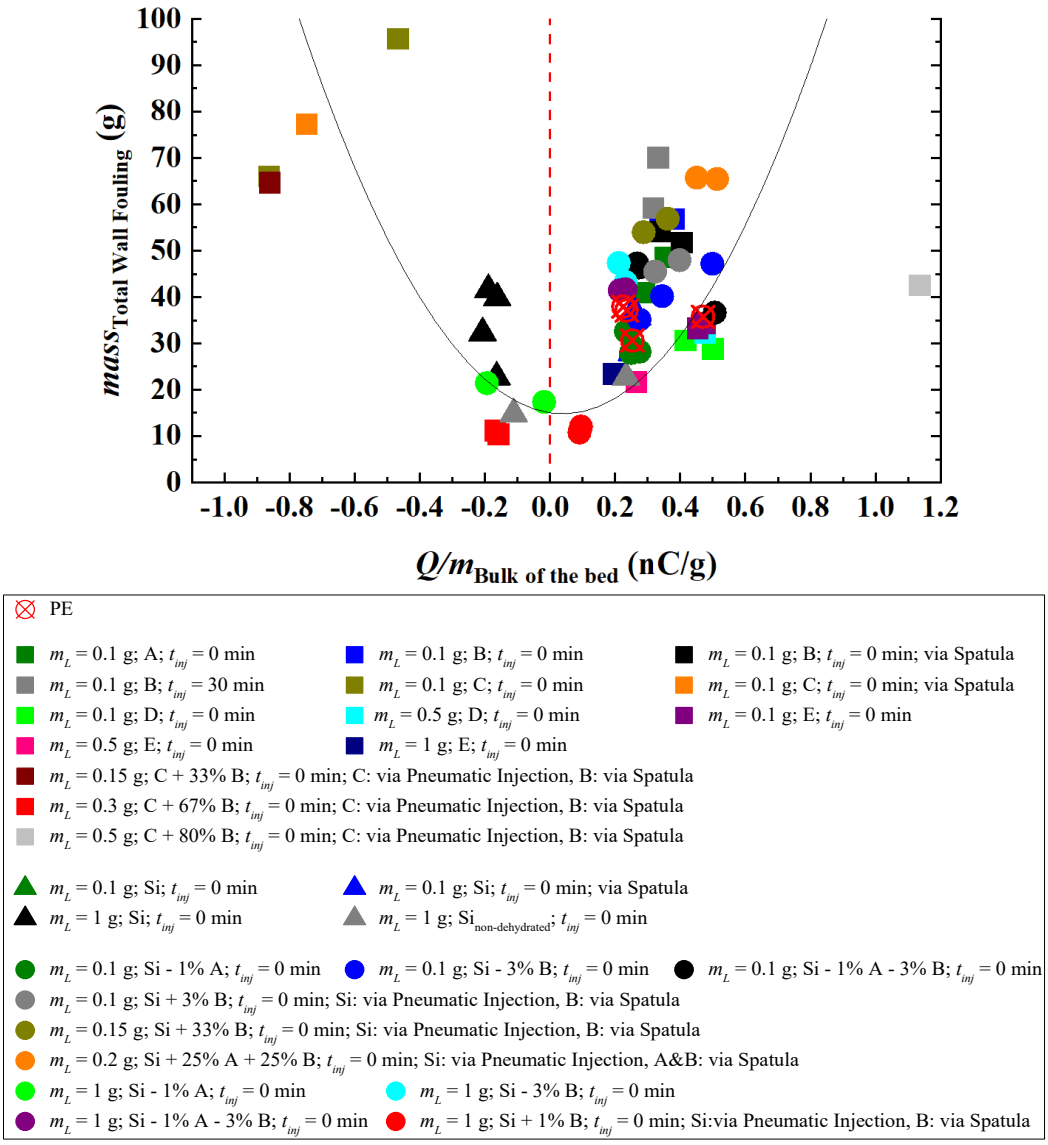

Fig. 1-23 Net specific charge of bulk polyethylene particles and the corresponding total wall fouling in the presence of different additives including silica (Si), AS-990 (A), aluminum distearate (B), calcium stearate (C), CHIMASSORB 944 (D), zinc stearate (E)) (copied from [84]).

Results from this prior study clearly implied that the total amount of wall fouling was directly related to the net specific charge of the bulk of the particles (i.e., lowest degree of total wall fouling was obtained when the net specific charge of the bulk was closest to zero).

Overall, as outlined above the first phase of the research program concluded that the surface chemistry of the solids added to the polyethylene particles played a more significant role in mitigating/promoting the extent of wall fouling than their accompanied charge magnitude brought into the fluidized bed. Knowing that in a commercial reactor, different solids with

various surface chemistry (i.e., catalysts) are present, they could also contribute to electrostatic charge buildup in polyethylene reactors due to Polyethylene-Catalyst, Polyethylene-Additive, and Catalyst-Additive collisions. Furthermore, since catalyst particles are pneumatically conveyed into the reactor, it is suspected that these particles become electrostatically charged by the time they arrive inside the reactor. This, in turn, is anticipated to influence not only the charging of the polyethylene resin within the reactor but also the role of continuity additives.

1.10 Electrostatic Charging in Pneumatic Conveying

Pneumatic conveying is a process that involves the transportation of solids in a gas stream. As summarized by Klinzing et al. [85] and shown in Fig. 1-24, a pneumatic conveying system is typically composed of four sections: a) prime mover; b) feeding, mixing, and accelerating; c) conveying; and d) separation. The prime mover provides the power required to convey solids and can be a compressor, a blower, a fan (positive pressure system) or a vacuum pump (negative pressure system). The feeding, mixing, and accelerating section is where solids are loaded into the system, and since there is a change in momentum for the solids, an acceleration zone should be provided to reach steady flow rate. Then, solids will enter the conveying part and eventually become separated from the conveying gas stream.

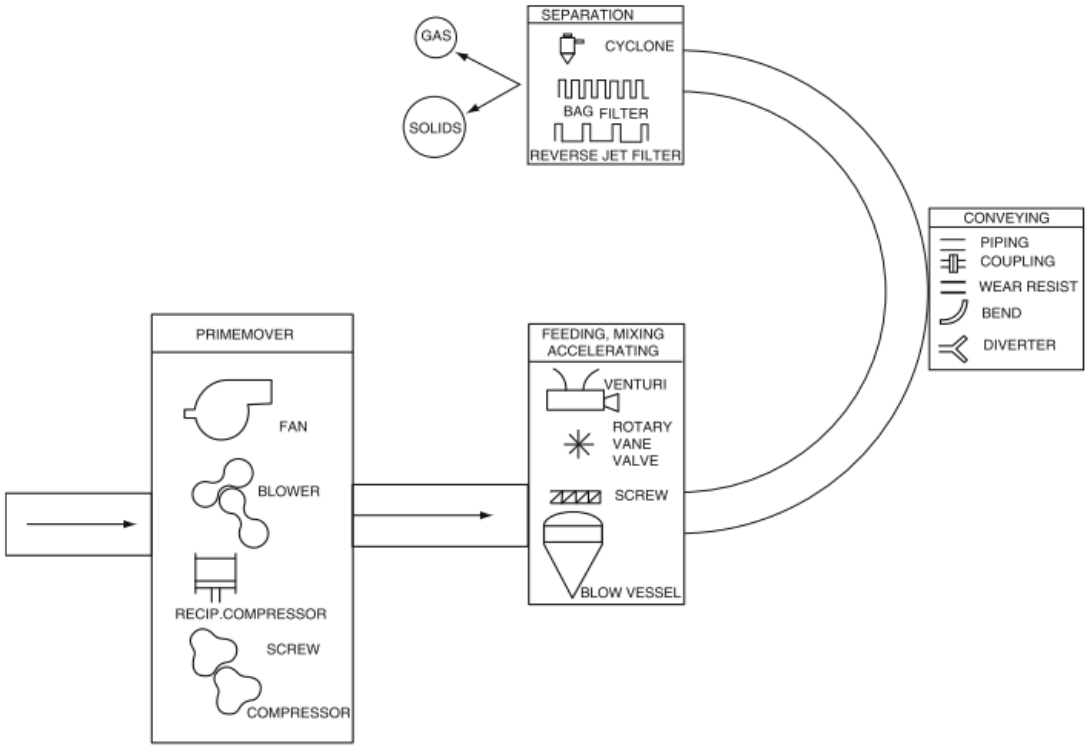

Fig. 1-24 Schematic of a typical pneumatic conveying system (copied from [85]).

Depending on the concentration of solids in the gas stream, pneumatic conveying is classified into a dilute phase or a dense phase system. If the mass ratio of solids to gas becomes greater than 15, pneumatic conveying changes from a dilute to a dense phase state. In a dilute phase, solid particles are fully suspended in gas and carried as discrete individuals in a velocity higher than saltation velocity (i.e., the velocity at which particles start to deposit at the bottom of a horizontal pipe), whereas in a dense flow, solids are not fully suspended and carried as discrete packs at a velocity lower than saltation velocity [85].

Pneumatic conveying systems are reported to generate the most amount of electrostatic charge among various types of gas-solid systems [86]. Parameters such as solids and conveying line material, solids loading ratio, mean particle size, conveying gas velocity, and relative humidity have been found to be influential on the magnitude and polarity of the charge generated [87,88]. Appendix D summarizes several studies on electrostatic charge generation in pneumatic conveying and the influence of different operating parameters.

To measure the electrostatic charge of the conveyed particles, two techniques have been used by researchers. One technique includes a flow-through type Faraday cup installed at the exit of the

conveying tube (Fig. 1-25). The Faraday cup contains a filter bag to capture the conveyed particles while allowing the conveying gas to exit the cup. The second method consists of two cylindrical metal pieces which are separated by an insulator. As illustrated in Fig. 1-26, to measure the charge of particles, the inner cylinder of the Faraday cup must completely cover the outer surface of the conveying tube. In this technique, particles induce the same polarity to the outer layer of the tube, and this charge is read by an electrometer.

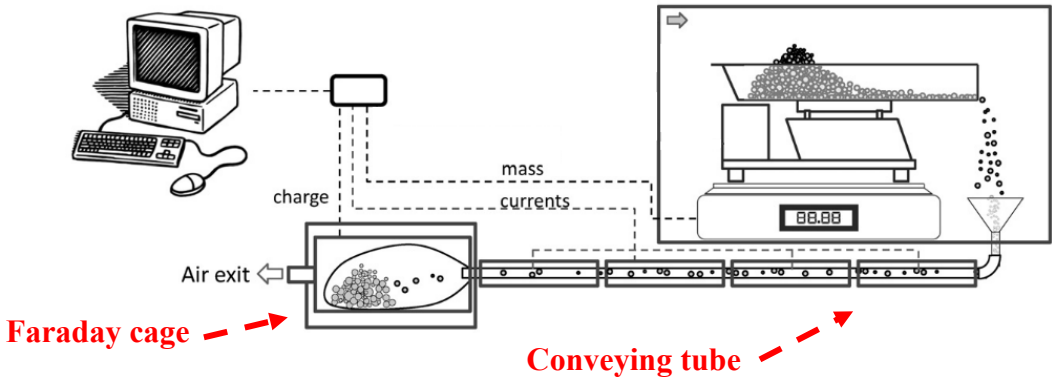

Fig. 1-25 Illustration of Faraday cup technique for pneumatic conveying application (adapted from [89]).

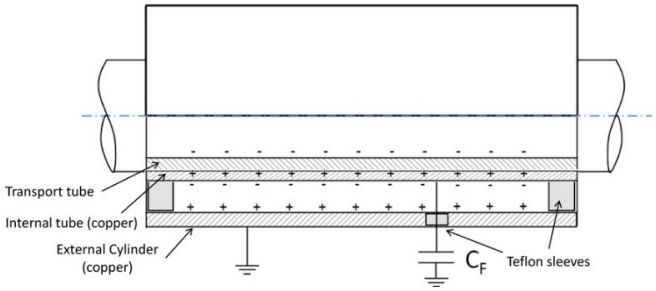

Fig. 1-26 Illustration of charge measurement technique off a conveying line (copied from [89]). The conveying line passes through an internal copper cylinder connected to an electrometer while the outer cylinder is grounded.

To design any pneumatic conveying system, the total pressure drop across the system needs to be determined. This can be calculated using the solids friction factor as a function of particle velocity [90]. Many studies have been conducted to evaluate particle velocity in continuous and dilute pneumatic conveying systems.

Although pneumatic conveying systems are known to generate the most amount of electrostatic charge in comparison to other gas-solid flow systems, none of the models presented in literature (see Chapter 5) account for the triboelectrification of the conveyed solids and its potential influence on the particle velocity. Therefore, it is important to study conveying particle velocity under conditions where electrostatics effects are significant. In addition, in relation to the polyethylene gas-phase process, catalyst particles are conveyed to the reactor via narrow (as small as 4.57 mm or ¼ inch nominal size) stainless steel tubes. However, no particle velocity correlation can be found for such small tube dimension which necessitates conveying particle velocity studies using such narrow tube diameters.

1.11 Thesis Objectives

Negative effects of electrostatic charging have been observed in many solids handling and processing systems. They include adhesion of charged particles to the neighbouring surfaces including the containing vessel walls, particle agglomeration, and high-voltage electric field generation that could be a source of hazardous ignitions. As previously mentioned, the polyolefin industry particularly experiences operational challenges due to electrostatic charging such as sheeting formation in polyethylene gas-solid fluidized bed reactors, which in turn results in reactor shutdowns and significant economic losses due to maintenance costs and reduction in productivity.

Despite several works reported in literature attempting to understand and determine means to mitigate the electrostatic charge generation, the issues related to electrostatics still persist in gas-solid industrial operations. This is mainly because the investigations at times are conducted under operating conditions that are not relevant to the industrial process that is affected by electrostatics. Hence, research is still necessary to better understand the sources that contribute the most to the generation of electrostatic charge and its adverse effects under industrially similar operating conditions. In relation to gas-solid fluidized beds and in particular polyethylene industrial reactors, two specific areas require further research, namely role of operating temperature and catalyst. The research presented in this thesis is focused on these two areas.

1.11.1 Effect of Temperature on Electrostatics in Fluidized Beds

As discussed, the effect of temperature on electrostatic charge generation and transfer in fluidized beds has not been completely understood. Irrespective to fluidization technology, there are three hypotheses on the effects of temperature on solids electrostatic charging:

1. Changes in surface area
2. Changes in material's electrical resistivity
3. Changes in energy levels of electrons

In gas-solid fluidized beds, the effect of temperature on solids charging behaviour has only been reported in two studies from one research group [66,81]. Both works have used electrostatic probes which provide a local measurement for a very short period, and most importantly do not provide a clear picture of the particles net charge distribution within the fluidized bed as well as their tendency to foul on the column wall which is of great importance in relation to industrial operations. Thus, in the first part of this thesis, the research focused on examining the effect of fluidization temperature on electrostatic charging of a LLDPE resin. Specifically, bench-scale shake tests as well as pilot-scale fluidization testing were conducted to better understand the role of temperature on the extent of particles charge generation and transfer. The main goal for this part of research was to:

a) Investigate the electrostatic charging behaviour of LLDPE particles in a fluidized bed at operating temperatures close to industrial reactors; and
b) Perform fundamental bench scale experiments to explain the influence of temperature on contact electrification.

1.11.2 Effect of Catalyst on Electrostatic Charging in Polyethylene Fluidized beds

In the study of electrostatic charge generation in polyethylene fluidized bed reactors, the majority of works have focused on charging tendency of polyethylene particles alone. However, in a real process, at any given time, catalyst particles are also present inside the reactor along with the polyethylene resin that is being produced. Knowing that the extent of triboelectrification and the polarity of charges generated is heavily influenced by the surface chemistry of the solids, it is critical to determine the role of the catalyst particles typically used in polyethylene production on the degree of the fluidized bed electrification and wall fouling formation. As discussed in section

1.5.1.2, a prior work in our research group [84] concluded that depending on the surface chemistry of solids added to the polyethylene bed, the net charge and polarity of fluidizing particles and the degree of wall fouling are influenced. In section 1.5.1, while discussing formation of sheeting in polyethylene reactors, the source of *warm sheets* was reported to be the catalyst particles. Therefore, the overall goal of this part of research was to investigate the electrostatic charging behaviour of the polyethylene resin in the presence of a commercially used catalyst (i.e., metallocene) and its support, which were pneumatically conveyed into a fluidized bed. To achieve this goal, a systematic approach was implemented in which, in addition to testing an active catalyst, the contribution of each component of the catalyst from its core to its surface, to the contact electrification inside the fluidized bed was also examined. Furthermore, the role of continuity additives on reducing wall fouling was examined by studying the active catalyst mixed with a continuity additive. In summary the powders tested include:

a) **Catalyst support:**
   Dehydrated amorphous silica
b) **Catalyst support + cocatalyst:**
   Dehydrated amorphous silica + Methyl aluminoxane (MAO)
c) **Active catalyst:**
   Dehydrated amorphous silica + MAO + $ZrCl_2$ + dicyclopentadiene
d) **Active catalyst + continuity additive:**
   Dehydrated amorphous silica + MAO + $ZrCl_2$ + dicyclopentadiene

The specific research objectives included:

a) Evaluation of the electrostatic charging behavior of a typical catalyst used in pas-phase polyethylene process (i.e., a metallocene catalyst) and its support and other components, in active and deactivated forms, due to their pneumatic conveying.
b) Study of the degree of the charge generation and the extent of fluidization column wall fouling when the powders tested in part (a) were pneumatically conveyed into a polyethylene bed.
c) Investigation of the influence of the concentration of powders tested in part (b) on the degree of the fluidized bed electrification and wall fouling.

It is important to note that the knowledge gained about the role of the catalyst and its chemistry on particles charging and their migration to the fluidization column wall in gas-phase polyethylene reactors will help in formulations of the new generation of catalysts that are being developed.

1.11.3 Effect of Electrostatic Charging on Solids Conveying Velocity

Since the research objective presented in 1.7.2 involved the investigation of powders charging behaviour due to their pneumatic conveying, a preliminary study was also carried out to determine the influence of the electrostatic charge on solids conveying velocity in narrow tubes similar to that used in this study for catalyst conveying. The motivation behind this objective was the hypothesis that if particles become electrostatically charged while being pneumatically conveyed, then their particle velocity could be affected by the generated electric field. This is an area that has received minimal attention especially that all correlations found in literature aiming at predicting particle velocity in conveying systems do not consider the effects of electrostatic force.

1.12 Thesis Outline

This thesis is composed of six chapters from which four chapters are organized in a manuscript format for publication in refereed journals. Additional supporting information is presented in Appendix A, B, C, D and E.

The second chapter describes the influence of temperature on contact electrification of polyethylene particles in a pressurized, gas-solid fluidized bed. The net specific charge of the particles that are present in the bed and on the column wall, and the entrained particles after one hour of fluidization at different temperatures is discussed. This chapter is a manuscript published in Journal of Powder Technology (*Mohsen Isaac Nimvari, Andrew Sowinski, Poupak Mehrani, Effect of Temperature on Triboelectrification of Polyethylene Particles in a Pilot-Scale Pressurized Gas-Solid Fluidized Bed, Powder Technology, 405, 117524, 2022*).

The third chapter discusses the possible influencing factors on contact electrification of polyethylene particles when temperature is raised. This chapter presents bench-sale shake test experiments performed with various sizes of LLDPE particles at two temperatures. In addition, this chapter presents the measurement of volume resistivity of a number of insulators at two

temperatures. This chapter is a manuscript published in Journal of Powder Technology *(Mohsen Isaac Nimvari, Andrew Sowinski, Poupak Mehrani, Investigation of the Role of Temperature on Contact Electrification of Polyethylene Particles, Powder Technol, 433, 119236, 2024).*

The fourth chapter describes the experiments performed to determine the role of a catalyst on the degree of charge generation and wall fouling during fluidization of LLDPE particles. Experiments were carried out with one type of metallocene catalyst in its active and deactivated form, along with the catalyst base (i.e., dehydrated amorphous silica), and the co-catalyst (i.e., methyaluminoxane). Experimentation involved the pneumatic injection of all aforementioned powders into the LLDPE bed and thus this chapter also presents the charging behavior of all tested powders during their pneumatic conveying. This chapter is a manuscript prepared for publication.

The fifth chapter presents a new simple approach to determine particles velocity using an electrical current signal measured from the conveying tube wall that is generated due to particles electrostatic charging while being pneumatically conveyed. This chapter also describes the effects of electrostatic charge on particles velocity and their flow behaviour. This chapter is a manuscript published in Journal of Powder Technology (*Mohsen Isaac Nimvari, Milad Taghavivand, Kwangseok Choi, Andrew Sowinski, Poupak Mehrani, Velocity Measurement of Pneumatically Conveyed Particles Via a Simple Current Signal Technique and the Influence of Electrostatic Charge, Powder Technology, 411, 118018, 2023*).

The final chapter, chapter six, presents the overall conclusions of this research and provides recommendations for future works.

References

[1] G. Hendrickson, Electrostatics and gas phase fluidized bed polymerization reactor wall sheeting, Chem. Eng. Sci. 61 (2006) 1041–1064.

[2] Y. Hu, D. Wang, J. Liu, J. Gao, A case study of electrostatic accidents in the process of oil-gas storage and transportation, J. Phys. Conf. Ser. 418 (2013) 1–5.

[3] M.U. Ghori, E. Šupuk, B.R. Conway, Tribo-electrification and powder adhesion studies in the development of polymeric hydrophilic drug matrices, Materials (Basel). 8 (2015) 1482–1498.

[4] J. Cross, Electrostatics: Principles, Problems and Applications, 1987.

[5] L.-S. Fan, C. Zhu, Principles of Gas-Solid Flows, Cambridge Series in Chemical Engineering, 1998.

[6] D.J. Lacks, A. Levandovsky, Effect of particle size distribution on the polarity of triboelectric charging in granular insulator systems, J. Electrostat. 65 (2007) 107–112.

[7] S. Matsusaka, H. Maruyama, T. Matsuyama, M. Ghadiri, Triboelectric charging of powders: A review, Chem. Eng. Sci. 65 (2010) 5781–5807.

[8] J. Callaway, Energy band theory, Academic Press, 1964.

[9] S.J. Ling, J. Sanny, W. Moebs, University Physics, OpenStax, 2016.

[10] A. Kahn, Fermi level, work function and vacuum level, Mater. Horizons. 3 (2016) 7–10.

[11] C. Kittel, Introduction to Solid State Physics, 8th edition, Wiley Sons, New York, NY. (2004).

[12] H. Young, R. Freedman, University Physics with Modern Physics, 15th ed., Pearson, 2019.

[13] A.F. Diaz, D. Wollmann, D. Dreblow, Contact Electrification: Ion Transfer to Metals and Polymers, Chem. Mater. 3 (1991) 997–999.

[14] D.J. Lacks, T. Shinbrot, Long-standing and unresolved issues in triboelectric charging, Nat. Rev. Chem. 3 (2019) 465–476.

[15] S.R. Waitukaitis, V. Lee, J.M. Pierson, S.L. Forman, H.M. Jaeger, Size-dependent same-material tribocharging in insulating grains, Phys. Rev. Lett. 112 (2014) 1–5.

[16] L.S. McCarty, G.M. Whitesides, Electrostatic charging due to separation of ions at interfaces: Contact electrification of ionic electrets, Angew. Chemie - Int. Ed. 47 (2008) 2188–2207.

[17] H.T. Baytekin, B. Baytekin, J.T. Incorvati, B.A. Grzybowski, Material transfer and polarity reversal in contact charging, Angew. Chemie - Int. Ed. 51 (2012) 4843–4847.

[18] J. Lowell, A.R. Akande, Contact electrification—why is it variable?, J. Phys. D. Appl. Phys. 21 (1988) 125–137.

[19] A.F. Diaz, Contact Electrification of Materials: The Chemistry of Ions on Polymer Surfaces, J. Adhes. 67 (1998) 111–122.

[20] A.F. Diaz, R.M. Felix-navarro, A semi-quantitative tribo-electric series for polymeric materials: the influence of chemical structure and properties, 62 (2004) 277–290.

[21] L.S. Mccarty, A. Winkleman, G.M. Whitesides, Ionic Electrets: Electrostatic Charging of Surfaces by Transferring Mobile Ions upon Contact, 12 (2007) 4075–4088.

[22] F. Galembeck, T.A.L. Burgo, L.B.S. Balestrin, R.F. Gouveia, C.A. Silva, A. Galembeck, Friction, tribochemistry and triboelectricity: Recent progress and perspectives, RSC Adv. 4 (2014) 64280–64298.

[23] L.S. Mccarty, A. Winkleman, G.M. Whitesides, Electrostatic Self-Assembly of Polystyrene Microspheres by Using Chemically Directed Contact Electrification **, (2007) 206–209.

[24] P.E. Shaw, C.S. Jex, Tribo-electrocoty and Friction, 1928.

[25] R.F. Gouveia, F. Galembeck, Electrostatic charging of hydrophilic particles due to water adsorption, J. Am. Chem. Soc. 131 (2009) 11381–11386.

[26] K.-I. Tanoue, A. Ema, H. Masuda, Effect of Material Transfer, J. Chem. Eng. Japan. 32 (1999) 544–548.

[27] R.K. Pandey, H. Kakehashi, H. Nakanishi, S. Soh, Correlating Material Transfer and Charge Transfer in Contact Electri fi cation, (2018).

[28] B. Baytekin, H.T. Baytekin, B.A. Grzybowski, What really drives chemical reactions on contact charged surfaces?, J. Am. Chem. Soc. 134 (2012) 7223–7226.

[29] D.J. Lacks, The unpredictability of electrostatic charging, Angew. Chemie - Int. Ed. 51 (2012) 6822–6823.

[30] P.E. Shaw, Experiments on Tribo-Electricity., Proc. R. Soc. Lond. 94 (1917) 16–33.

[31] W.R. Harper, Contact and Frictional Electrification, Morgan Hill, Laplacian, 1998.

[32] D.M. Gooding, G.K. Kaufman, Tribocharging and the Triboelectric Series, Encycl. Inorg. Bioinorg. Chem. (2014) 1–9.

[33] J. Ciborowski, A. Wlodarski, On electrostatic effects in fluidized beds, Chem. Eng. Sci. 17 (1962) 23–32.

[34] M. Fujino, S. Ogata, H. Shinohara, the electric potential distribution profile in a naturally charged fluidized bed and its effects, Int. Chem. Eng. 25 (1985).

[35] P. Mehrani, H.T. Bi, J.R. Grace, Electrostatic charge generation in gas-solid fluidized beds, J. Electrostat. 63 (2005) 165–173.

[36] P. Mehrani, M. Murtomaa, D.J. Lacks, an overview of advances in understanding electrostatic charge buildup in gas-solid fluidized beds, J. Electrostat. 87 (2017) 64–78.

[37] D. Kunii, O. Levenspiel, Fluidization Engineering, 2nd ed., Butterworth—Heinemann Boston, 1991.

[38] J.R. Grace, Fluidized Bed Hydrodynamics Handbook of Multiphase Systems, Chap. 8.1, Hemisphere Publishing Corp., 1982.

[39] G. Gonzlez, N. Prieto, O. Fabio, Fluid Dynamics of Gas - Solid Fluidized Beds, in: Adv. Fluid Dyn., 2012.

[40] D. Geldart, Types of Gas Fluidization, Powder Technol. 7 (1973) 285–292.

[41] B.D. Fulks, S.P. Sawin, C.D. Aikman, J.M. Jenkins, Process for reducing sheeting during polymerization of alpha-olefins, United States Patent, No. 4532311, (1985).

[42] M.G. Goode, D.M. Hasenberg, T.J. McNeil, T.E. Spriggs, Method for Reducing Sheeting During Polymerization of Alpha-Olefns, 4803251, 1989.

[43] F.J. Karol, F.I. Jacobson, Catalysis and the Unipol process, Kodansha Ltd., 1986.

[44] J.R. Chirillo, K.C. Kimbrough, P.E. McHattie, Method for reducing sheeting during polymerization of alpha-olefins, US Patent, No. 4855370, (1986).

[45] R. Hoff, ed., Handbook of Transition Metal Polymerization Catalysts, Second Edi, Wiley, 2010.

[46] Z. Liu, X. He, R. Cheng, M.S. Eisen, M. Terano, S.L. Scott, B. Liu, Chromium catalysts for ethylene polymerization and oligomerization, 1st ed., Elsevier Inc., 2014.

[47] X. Li, R. Cheng, J. Luo, Q. Dong, X. He, L. Li, Y. Yu, J. Da, B. Liu, Experimental and theoretical studies on ethylene polymerization using SiO2-supported silyl chromate type catalysts prepared by a green method, J. Mol. Catal. A Chem. 330 (2010) 56–65.

[48] S.S. Reddy, S. Sivaram, Homogeneous metallocene-methylaluminoxane catalyst systems for ethylene polymerization, Prog. Polym. Sci. 20 (1995) 309–367.

[49] A. Shamiri, M.H. Chakrabarti, S. Jahan, M.A. Hussain, W. Kaminsky, P. V. Aravind, W.A. Yehye, The influence of Ziegler-Natta and metallocene catalysts on polyolefin structure, properties, and processing ability, Materials (Basel). 7 (2014) 5069–5108.

[50] Y.I. Yermakov, V.A. Zakharov, G.A. Nesterov, Catalysis by Supported Complexes, Elsevier, Amsterdam, 1981.

[51] M. Terano, K. Soga, Catalyst Design for Tailor-Made Polyolefins, Kodansha Ltd., Tokyo, 1994.

[52] I.T. Lima, R. Gargano, S. Guerini, E.N.C. Paura, A theoretical study of adsorbed non-metallic atoms on magnesium chloride monolayers, New J. Chem. 43 (2019) 7778–7783.

[53] D. V. Stukalov, V.A. Zakharov, Active site formation in MgCl2-supported ziegler - Natta catalysts. A density functional theory study, J. Phys. Chem. C. 113 (2009) 21376–21382.

[54] F. Poorsank, H. Arabi, N. Ghasemi Hamedani, Silyl diol ester as a new selectivity control agent in MgCl2-supported Ziegler-Natta systems for propylene polymerization: Catalyst structure and polymer properties, RSC Adv. 9 (2019) 7420–7431.

[55] A. Piovano, M. Signorile, L. Braglia, P. Torelli, A. Martini, T. Wada, G. Takasao, T. Taniike, E. Groppo, Electronic Properties of Ti Sites in Ziegler-Natta Catalysts, ACS Catal. 11 (2021) 9949–9961.

[56] X. Guo, Z. Liu, Z. Fan, B. Liu, New Insights into the Nature of Ti(II) and Ti(III) Active Sites in the Heterogeneous Ziegler-Natta Catalyst, J. Phys. Chem. C. 127 (2023) 5720–5730.

[57] D. V. Stukalov, I.L. Zilberberg, V.A. Zakharov, Surface species of titanium(IV) and titanium(III) in MgCl 2-Supported ziegler-natta catalysts. A periodic density functional theory study, Macromolecules. 42 (2009) 8165–8171.

[58] T. Taniike, M. Terano, Reductive formation of isospecific Ti dinuclear species on a MgCl 2 (110) surface in heterogeneous ziegler-natta catalysts, Macromol. Rapid Commun. 29 (2008) 1472–1476.

[59] J. Wang, R. Cheng, X. He, Z. Liu, Z. Tian, B. Liu, A Novel (SiO 2 / MgO / MgCl 2)· TiCl x Ziegler – Natta Catalyst for Ethylene and Ethylene / 1-Hexene Polymerization, Macromol. Chem. Phys. 216 (2015) 1472–1482.

[60] B. Jiang, F. He, P. Yang, Z. Zhang, Y. Weng, Z. Cheng, Z. Fu, Z. Fan, Enhancing stereoselectivity of propylene polymerization with MgCl2-supported Ziegler-Natta catalysts by electron donor: Strong effects of titanium dispersion state, Catal. Commun. 121 (2019) 38–42.

[61] G.-H. Song, C.W. Va, A.S. Rhee, B.M.N. J, G.G. Lowder, T. Victoria, Method for reducing sheeting and static charged during polymerization of ethylene plymers, United States Patent, No. 5391657, (1995).

[62] B.P. Etherton, G.G. Hlatky, J.H. Meas, Olefin polymerization process with fatty amine additives for improved activity and reduced fouling - US Patent - No 6201076, 2001.

[63] C.-I. Kuo, G.G.H. Patel, R.E. Pequeno, B.J. Savatsky, F.D. Hussein, Continuity additive for polyolefin polymerization processes, US Patent, No. 9221936, 2015.

[64] M. Taghavivand, A. Sowinski, P. Mehrani, Triboelectric effects of continuity additives and a silica catalyst support on polyethylene fluidized bed wall fouling, Chem. Eng. Sci. 245 (2021) 116882.

[65] D. Song, P. Mehrani, Mechanism of particle build-up on gas-solid fluidization column wall due to electrostatic charge generation, Powder Technol. 316 (2017) 166–170.

[66] W.O. Moughrabiah, J.R. Grace, X.T. Bi, Effects of Pressure, Temperature, and Gas Velocity on Electrostatics in Gas-Solid Fluidized Beds, Ind. Eng. Chem. Res. 48 (2009) 320–325.

[67] D. Song, F. Salama, J. Matta, P. Mehrani, Implementation of Faraday cup electrostatic charge measurement technique in high-pressure gas-solid fluidized beds at pilot-scale, Powder Technol. 290 (2016) 21–26.

[68] M. Bafrnec, J. Beňa, Quantitative data on the lowering of electrostatic charge in a fluidized bed, Chem. Eng. Sci. 27 (1972) 1177–1181.

[69] J. Guardiola, G. Ramos, A. Romero, Electrostatic behaviour in binary dielectric/conductor fluidized beds, Powder Technol. 73 (1992) 11–19.

[70] J. Revel, C. Gatumel, J.A. Dodds, J. Taillet, Generation of static electricity during fluidisation of polyethylene and its elimination by air ionisation, Powder Technol. 135–136 (2003) 192–200.

[71] A. Sowinski, A. Mayne, P. Mehrani, Effect of fluidizing particle size on electrostatic charge generation and reactor wall fouling in gas-solid fluidized beds, Chem. Eng. Sci. 71 (2012) 552–563.

[72] N. Sridhar, Role of Dielectric Strength of Gases on the Degree of Solids Electrostatic Charging and Fouling in Fluidization and Pneumatic Conveying Systems, University of Ottawa, 2023.

[73] W.O. Moughrabiah, J.R. Grace, X.T. Bi, Effects of Pressure, Temperature, and Gas Velocity on Electrostatics in Gas-Solid Fluidized Beds, Ind. Eng. Chem. Res. 45 (2009) 320–325.

[74] F. Fotovat, K. Gill, J.R. Grace, X.T. Bi, Impact of column material on electrostatics and entrainment of particles from gas-solid fluidized beds, Chem. Eng. Sci. 167 (2017) 120–134.

[75] T.A. Alsmari, J.R. Grace, X.T. Bi, Effects of particle properties on entrainment and electrostatics in gas-solid fluidized beds, Powder Technol. 290 (2016) 2–10.

[76] A. Giffin, P. Mehrani, Effect of gas relative humidity on reactor wall fouling generated due to bed electrification in gas-solid fluidized beds, Powder Technol. 235 (2013) 368–375.

[77] S. Jantač, L. Konopka, J. Kosek, Experimental study of triboelectric charging of polyethylene powders: Effect of humidity, impact velocity and temperature, Adv. Powder Technol. 30 (2019) 148–155.

[78] W.D. Greason, Investigation of a test methodology for triboelectrification, J. Electrostat. 49 (2000) 245–256.

[79] I.A. Harris, M.X. Lim, H.M. Jaeger, Temperature dependence of nylon and PTFE triboelectrification, Phys. Rev. Mater. 3 (2019) 1–10.

[80] S. Lin, L. Xu, C. Xu, X. Chen, A.C. Wang, B. Zhang, P. Lin, Y. Yang, H. Zhao, Z.L. Wang, Electron Transfer in Nanoscale Contact Electrification: Effect of Temperature in the Metal–Dielectric Case, Adv. Mater. 31 (2019) 1–9.

[81] T.A. Alsmari, J.R. Grace, X.T. Bi, Effects of superficial gas velocity and temperature on entrainment and electrostatics in gas-solid fluidized beds, Chem. Eng. Sci. 123 (2015) 49–56.

[82] S. Ali, Y. Ji, Q. Zhang, H. Zhao, W. Chen, D. Wang, L. Meng, L. Li, Preparation of polyethylene and ethylene/methacrylic acid copolymer blend films with tunable surface properties through manipulating processing parameters during film blowing, Polymers (Basel). 11 (2019).

[83] A. Sowinski, P. Mehrani, Impact of addition of a catalyst or its support on reactor wall coating due to electrostatic charging during fluidization of polyethylene, Ind. Eng. Chem. Res. 54 (2015) 3981–3988.

[84] M. Taghavivand, Role of Catalyst Support and Continuity Additives on the Degree of Electrostatic Charging and Reactor Fouling in Polyethylene Gas-solid Fluidized Bed Reactors, University of Ottawa, 2021.

[85] G.E. Klinzing, F. Rizk, R. Marcus, L.S. Leung, Pneumatic Conveying of Solids, Springer, 2010.

[86] G.E. Klinzing, Historical review of pneumatic conveying, KONA Powder Part. J. 2018 (2018) 150–159.

[87] H. Masuda, S. Matsusaka, H. Shimomura, Measurement of mass flow rate of polymer powder based on static electrification of particles, Adv. Powder Technol. 9 (1998) 169–179.

[88] E.E. Smeltzer, M.L. Weaver, G.E. Klinzing, Individual electrostatic particle interaction in pneumatic transport, Powder Technol. 33 (1982) 31–42.

[89] K. Saleh, A. Traore Ndama, P. Guigon, Relevant parameters involved in tribocharging of powders during dilute phase pneumatic transport, Chem. Eng. Res. Des. 89 (2011) 2582–2597.

[90] R. Naveh, N.M. Tripathi, H. Kalman, Experimental pressure drop analysis for horizontal dilute phase particle-fluid flows, Powder Technol. 321 (2017) 355–368.

Chapter 2 – Effect of Temperature on Triboelectrification of Polyethylene Particles in a Pilot-Scale Pressurized Gas-Solid Fluidized Bed

Abstract

In this work, the influence of temperature on electrostatic charging behaviour of polyethylene (PE) particles and their degree of fouling in a pilot-plant fluidized bed was studied. PE resin received from a commercial reactor was fluidized in a 0.15 m stainless-steel column at two pressures of 101 and 2600 kPa while the operating temperatures varied from 24 to 58ºC. The amount of wall fouling, and particles charge distribution in various regions of the bed were measured. At atmospheric pressure, the fouling declined by approximately 30%, when the average bed temperature was doubled from 24ºC. At 2600 kPa, a similar trend was observed although the influence of temperature was significantly greater, with 72.5% decline at the highest temperature tested. The particles within the bulk of the bed acquired less net specific charge (Q/m) at higher temperatures, signifying a lower electrostatic charge generation within the bed with the increase in temperature.

2.1 Introduction

The nature of fluidization process is accompanied with continuous particle-particle and particle-fluidization column wall contacts which could result in electrostatic charge generation of the fluidized particles. The electrostatic charge build-up within the fluidized bed in turn can cause considerable operational challenges such as particle agglomeration and accumulation of particles on the fluidized bed walls. Such adverse effects can be seen in some commercial reactors including gas-phase polymerization fluidized bed reactors to produce polyethylene. In such reactors, the buildup of catalyst and polyethylene particles on the reactor walls and in turn the lack of adequate heat removal results in the formation of *wall sheets* in various locations of the reactor [1]. Wall sheeting could cause a reduction in fluidization quality and in some cases reactor shutdown for cleaning. Attempts have been made to quantify electrostatic charges and to develop suitable charge reduction or elimination techniques in gas-solid fluidized beds including that of the polyethylene reactors [2–6]. Nevertheless, operational challenges due to electrostatic charging still persist, particularly in polyethylene industry, hence necessitating better understanding of fluid bed electrification under commercial operating conditions.

In general, a number of parameters have been found to influence the extent of electrostatic charge generation in gas-solid fluid beds including fluidizing gas velocity, relative humidity, material of the column and fluidized particles, particle size, and operating pressure [6–12]. To better understand commercial fluid bed electrification, investigations must be conducted at relevant operating conditions. For instance, commercial polyethylene reactors are typically operated at 1800-2400 kPa and 80-110ºC [3], thus requiring studies at such pressures and temperatures. Although electrostatic charging behavior of polyethylene particles fluidized under elevated pressures (up to 2600 kPa) has been previously investigated in this research group [13], but the operating temperature has received minimal attention.

In relation to the influence of temperature on the electrostatic charging behavior of solids in general, a few bench-scale works are reported [14–17]. Greason [14] investigated the effect of humidity and temperature on the degree of electrostatic charging of a 0.0127 m stainless steel ball. The ball had rolling contact with the inner surface of a tube made of different insulators (quartz, glass, polycarbonate, acrylic, PTFE, type 6/6 nylon). All tests were conducted in a test chamber at a controlled range of temperature (10-30°C) and relative humidity (10-70%). It was

shown that at relative humidity percentages (RH%) less than 60%, by increasing temperature, the charge generated due to metal-insulator contact decreased. The author related this observation to the effective resistance of materials in which as the resistivity decreases with increasing temperature, the charge leakage to the ground increases. Harris et al. [15] investigated the triboelectrification of nylon and PTFE when 30×30×3.2 mm pieces of the two insulators were brought into contact. The PTFE disc was placed inside a Faraday cup while the nylon disc was brought into contact with it. The charge transferred between the two surfaces was read by an electrometer connected to the Faraday cup. All the experiments were performed in a controlled environment with relative humidity of 42-44% and at various temperatures (24-78°C). They observed that the saturation charge on the surface of the two insulators decreased by increasing the temperature (e.g., saturation charge at 24°C was approximately double of that at 78°C). Jantac et al. [16] studied the triboelectrification of 800–1000 micron polyethylene particles and 500-800 micron glass beads at two temperatures of 22 and 90°C. They shook these particles in an aluminum box which was placed in a temperature and relative humidity-controlled environment (glove bag). They observed that at 35% relative humidity, the charge of polyethylene particles was greater when the temperature of the particles and the apparatus was 90°C but for glass beads the trend was inverse. They suggested that at higher temperatures, polyethylene particles are softer and thus, their contact surface area during collisions increased. However, for glass beads they referred to Greason [13] work that stated charge leakage from glass beads was higher at elevated temperatures. Lin et al. [17] investigated the effect of temperature on charge transfer between a metal and an insulator by using atomic force microscopy (AFM) and Kelvin probe force microscopy. The metal was the tip of the AFM cantilever (50 nm in diameter) which was coated by Au, and the insulator was a layer of 100 nm SiO_2 in thickness which was deposited on a silicon surface by thermal oxidation. A tapping mode (point by point contact of the tip on the sample surface with a speed of 0.001 s/contact) was used to conduct contact electrification. The temperature was altered from 40ºC to 120ºC, and they observed that electrons tend to transfer from a warmer to a colder surface. Also, a thermoionic-emission, band-structure model was proposed based on the relation between electron's energy level (which depends on temperature) and Fermi energy level. In this model, the material with a larger value of the summation of Fermi energy (which is at 0 K) and the energy of electrons (which is ~kT at a given temperature, k is Boltzman constant) was labeled as an electron donor.

From these studies, it can be concluded that for metal-insulator contacts the particles tend to become more negatively charged with increasing temperatures, regardless of their initial polarity (i.e., if a particle is initially positively or negatively charged, the magnitude of the charge becomes less or more, respectively). However, for insulator-insulator contacts the charge transferred between the two materials reduces with elevation in temperature. Also, it was suggested that temperature can facilitate the transfer of electrons from a material by increasing the energy level of electrons.

With respect to gas-solid fluidization process, only two studies have been found in open literature studying the influence of temperature [8, 11]. Moughrabiah et al. [8] used collision ball probes to measure the cumulative charge of 600 μm linear low-density polyethylene (LLDPE) particles at different axial location inside a stainless-steel fluidization column. At the operating condition of 379 kPa, their results showed that the LLDPE particles cumulative charge over time increased at 20ºC and stayed constant at 60ºC. The same research group using the same experimental apparatus later evaluated the electrostatic charging of a mixture of fine (25-50 μm) and large (425-600 μm) glass beads at 414 kPa while varying the temperatures from 20°C to 75°C [11]. They showed that by increasing temperature, electrostatic charge measured at different locations of the bed decreased, and for temperatures above 70°C, a polarity change was observed. In the same study, the authors also observed that the charge of entrained glass beads declined as the temperature increased while the particles mass flux did not have a noticeable change.

Overall, there is limited knowledge available about the effect of temperature on solids charging behavior especially in relation to fluidization systems. In works by Moughrabiah et al [8] and Alsmari et al [11], collision ball probes were used for particles electrostatic charge measurement, which do not provide any information concerning the fluid bed wall fouling generated due to the charged fluidized particles. Moreover, their experiments were performed at low and constant pressures that were away from some industrial operating conditions. Hence, in this study we aimed at investigating the effect of temperature on the degree of electrostatic charge build-up within a pilot-scale fluidized bed at elevated temperature and pressure operating conditions, and for the first time the change in mass and the net charge of particles fouled on the fluidization column wall as well as the bulk of the bed are reported.

2.2 Materials and methods

In this work, a pilot plant pressurized fluidization system was utilized. A detailed description of the system and charge measurement technique is presented elsewhere [13–18]. The fluidized bed was a stainless-steel column with an inner diameter of 0.15 m and a total height of 5 m (2.5 m fluidization section) containing a perforated distributor plate. The apparatus was modified for this work to enable heating the fluidizing gas to temperatures up to 60ºC (Fig. 2-1). Operation above ambient temperature was achieved by band heaters placed on the gas pipes at the inlet of the fluidization column and around the column up to the height of 0.75 m. The temperature of the fluidizing gas was monitored by two thermocouples. As shown in Fig. 2-1, one thermocouple was located below the distributor plate (T_1), and other one (T_2) was placed at 0.75 m above the distributor plate (i.e., 0.35 m above the static bed height).

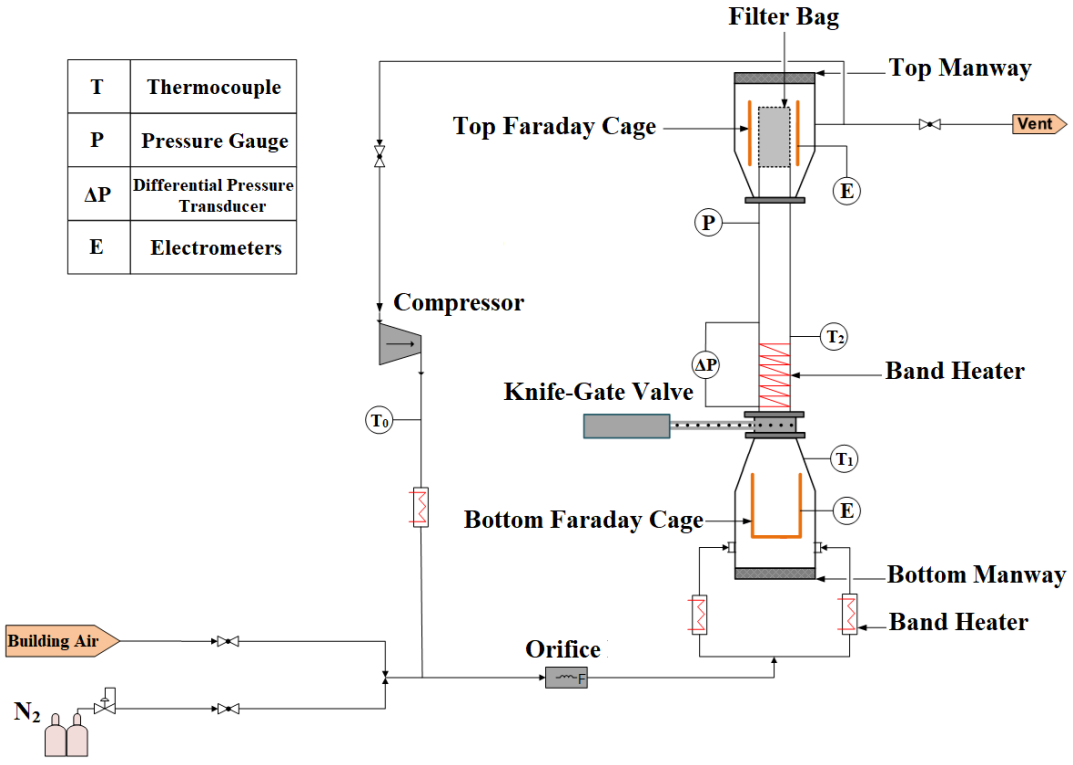

Fig. 2-1. Schematic of the pilot-scale pressurized fluidization system.

The fluidized bed was operated up to 2600 kPa using building air and/or compressed air cylinders. In atmospheric experiments, building air with RH% of <3% was used as the fluidization gas, which entered the column at the bottom and was vented at the top. At higher

pressures, the system was first filled with air from gas cylinders to a desired operating pressure in a closed loop. In this mode, a centrifugal compressor with a variable speed drive recirculated the gas within the system at a desired fluidization superficial gas velocity. The plate heat exchanger located after the compressor acted as a cooler for ambient temperature operations using chilled water as a cooling medium, and as a heater for higher temperature operations using hot water as a heating medium. The gas flow rate was measured using an orifice plate meter, and the operating pressure by a gauge pressure transducer mounted on the fluidization column. For each operating pressure, the minimum fluidization velocity (U_{mf}) was determined experimentally by measuring the pressure drop across the bed at various superficial gas velocities. It should be noted that the effect of temperature on the minimum fluidization velocity and hydrodynamics of the bed was negligible in the range of the operating temperatures tested in this work.

For experiments above ambient temperatures, first, all heaters were turned on to warm up the system for 30 minutes. Then, particles that were kept in an oven overnight were poured into the column to a static bed height of approximately 30 cm. This was followed by mounting the top Faraday cage, closing the top manway, and pressurizing the system. A very low flow rate of gas with a velocity of approximately $0.25U_{mf}$ was then passed through the system for 30 minutes to warm the fluidizing gas. The fluidization period was then commenced by increasing the fluidizing gas velocity to $1.5U_{mf}$ (i.e., bubbling flow regime) and continued for 60 minutes. Each operating condition was repeated 2 to 4 times to confirm the reproducibility of results. It is noteworthy to mention that maintaining the operating temperature at an exact value for repeated experiments was challenging, thus individual results were collected for each run and grouped into three categories of low-range (24-28°C), mid-range (42-44°C) and high-range (48-58°C) temperatures.

To determine the particles electrostatic charge, two Faraday cages were used, located at the top and bottom of the fluidization column, and both directly connected to digital Keithley Model 6514 electrometers. The top Faraday cage measured the charge of the entrained particles (referred to as *Fines*) which were captured by a filter bag at its center. After a fluidization period of 60 minutes, the filter bag was removed to measure the mass of the Fines. To determine the charge and mass of the fluidized particles (referred to as *Bulk*), the distributor plate was opened allowing the particles to drop into the bottom Faraday cage. At this point, the inner wall of the

column was inspected for any particle accumulation and images were taken from the fouled layer. Then, a narrow tube was inserted into the column from the top and a very small air flow was used to gradually dislodge the particles accumulated on wall (referred to as *Fouling*) to the bottom Faraday cage to measure their mass and net charge. As shown in Fig. 2-2, the Fouling along the column wall consisted of three regions: (1) from distributor plate up to the static bed height (referred to as *Fouling-Bottom*); (2) from the static bed height to 0.30 m above that (referred to as *Fouling-Top*); and (3) the freeboard region which extended to the exit of the column (referred to as *Freeboard*).

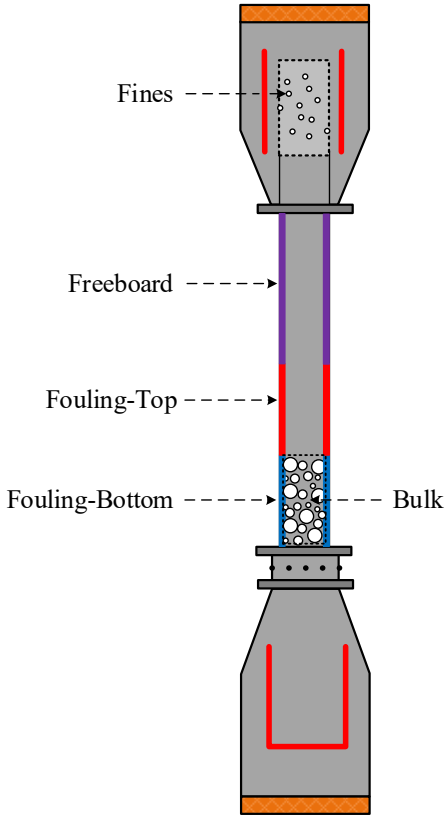

Fig. 2-2. Schematic of the different locations that particles are present.

In this work linear low-density polyethylene (LLDPE) resin received from commercial reactors was fluidized. The properties of the particles and the fluidizing gas at different operating conditions are summarized in Table 2-1. The charge of the particles prior to their placement in the fluidization column (i.e., initial charge) was measured using a bench-scale Faraday cage.

Table 2-1. Properties of PE particles and the fluidizing gas.

Particles	
Type	LLDPE resin (received directly from industry)
Size distribution (µm)	20-2000
Mean diameter (µm)	820
Density (kg/m^3)	917
Initial charge (nC/g)	-0.175±0.05
Gas	
Type	Dry air from a high-pressure cylinder
Bed Temperature (°C)	24-58ºC
Pressure (kPa)	101, 2600
Superficial Velocity (m/s)	1.5 U_{mf} (bubbling flow regime)
U_{mf}@ 101 kPa (m/s)	0.085
U_{mf}@ 2600 kPa (m/s)	0.15

2.3 Results and discussion

The electrostatic charge of particles present at various regions of the bed was measured after fluidization at different operating conditions, and the results are shown in Fig. 2-3 and Fig. 2-4 in the form of particles' net *Q/m*. It is important to note that Fig. 2-3 and Fig. 2-4 present separate and individual result obtained from repeated experiments. Fig. 2-3 and Fig. 2-4 clearly point to the presence of bi-polar charging for all conditions tested in this work where *Bulk* and *Fouling-Bottom* had a net negative polarity while the particles in the *Fouling-Top* and *Freeboard* layer had a net positive polarity. The reason that some particles acquired a net negative polarity is that the work function of the stainless-steel column wall is lower than that of PE particles (4.5 eV vs. 5.3 eV) [19]. Hence, PE particles would gain a negative charge polarity in contact with the stainless-steel wall. The charged particles in the Bulk of the bed would then begin migrating to the column wall depending on their charge magnitude and polarity. In this case, the net negative polarity of the fluidized particles would induce an image of that charge (in opposite polarity) on the metallic column wall. In turn, this would result in accumulation of negatively charged particles on the wall. Subsequently, the electrostatic force originated by the first layer on the wall, attracts or repels the particles in the *Bulk* with an opposite or a same polarity, respectively. Thus, additional particle layers can form, depending on the charge magnitude and polarity of the first layer and the particles present in the *Bulk* of the bed. Fig. 2-5 shows an image of the layers formed on the wall.

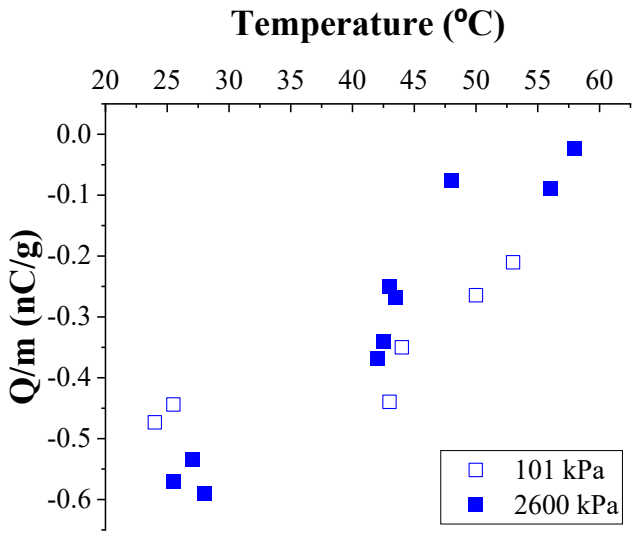

Fig. 2-3. The net specific charge of *Bulk* particles at different operating temperatures and pressures.

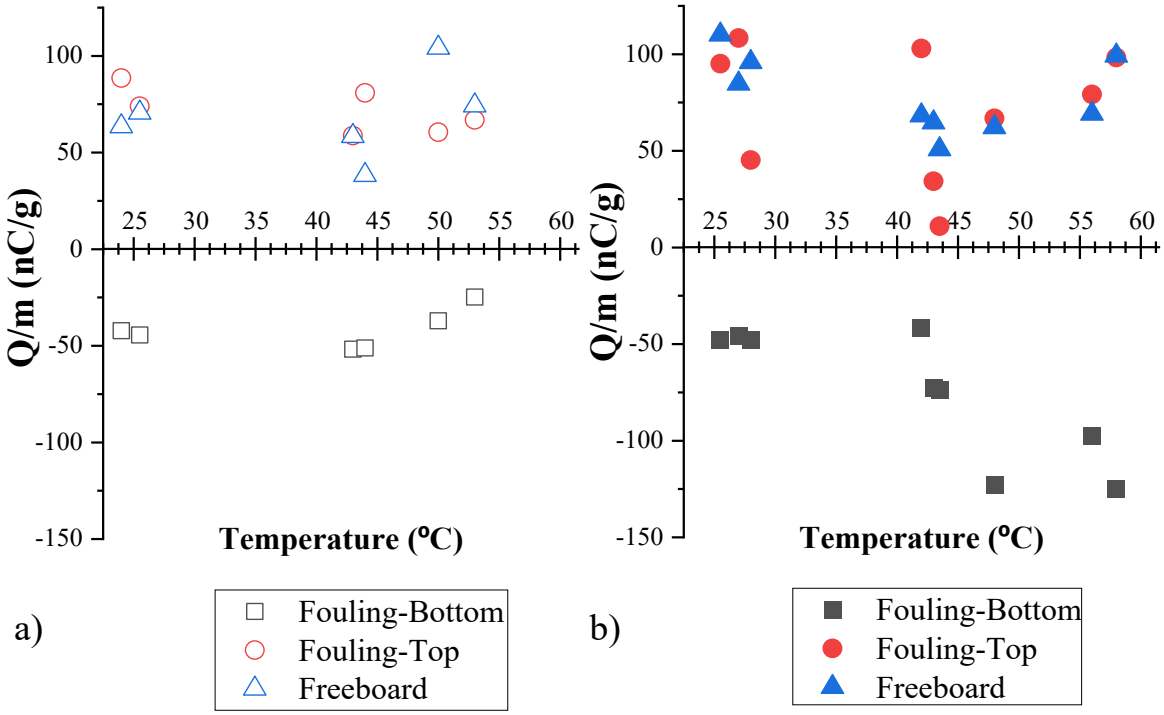

Fig. 2-4. The net specific charge of particles fouled in different regions of the column wall at various operating temperatures and (a) 101 kPa and (b) 2600 kPa.

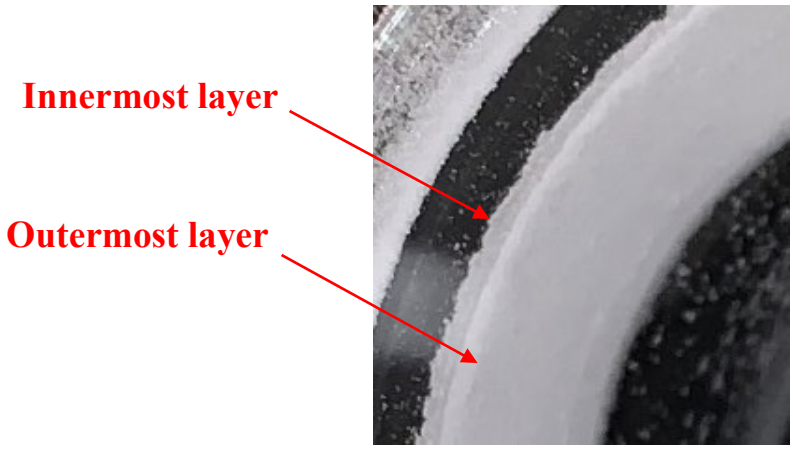

Fig. 2-5. An example of particle layer formation on the column wall.

Another factor that can influence the multi-layer fouling formation on the column wall is the size of the particles that in turn affects the balance between gravitational, drag and electrostatic forces. Larger sized particles tend to be present in the *Bulk* region, owing to their greater gravitational force. However, fine particles are most likely to leave the column during fluidization if their terminal velocity is less than their superficial gas velocity and/or adherence to the column wall due to their greater surface to mass ratio resulting in their greater electrostatic charge. Samples collected from different regions (i.e., *Bulk* and *Fouling*) were analyzed for the size distribution of particles using a Malvern Mastersizer 2000, and the results are shown in Table 2-2. No significant variation in the range of the size of the particles was observed under different operating conditions; and thus, results presented here include range of size detected per region. It is evident that particles smaller than 500 µm were attracted to the fluidization column while those larger remained within the Bulk of the bed.

Table 2-2. Particle size distribution range of samples collected before (initial) and after fluidization from different regions of the bed for all operating conditions tested.

Region	**Size (µm)**		
	d_{10}	d_{50}	d_{90}
Initial	320±25	682±47	1070±174
Bulk	350±28	656±44	1132±143
Fouling-Bottom	212±23	358±37	589±86

Fig. 2-6 shows the results of the total amount of wall fouling as well as its distribution along the fluidization column wall, and Fig. 2-7 illustrates the images of the inner column wall. Overall, with respect to the operating pressure it is evident that a greater degree of fouling occurred at the

elevated pressure. A previous study in our research group on the effect of fluidization pressure [18] concluded that as the operating pressure increased, from atmospheric to 2600 kPa, the size of gas bubbles decreased while their frequency was increased. Such behaviour would then result in more particle mixing in the bed (i.e., more particle-particle and particle-wall contacts), and in turn higher degree of electrostatic charging and more fouling at elevated pressures.

(a)

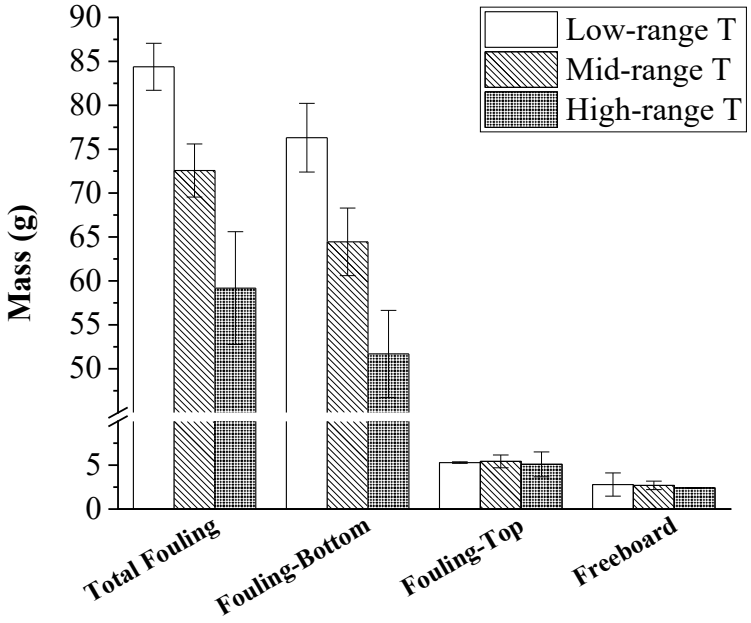

(b)

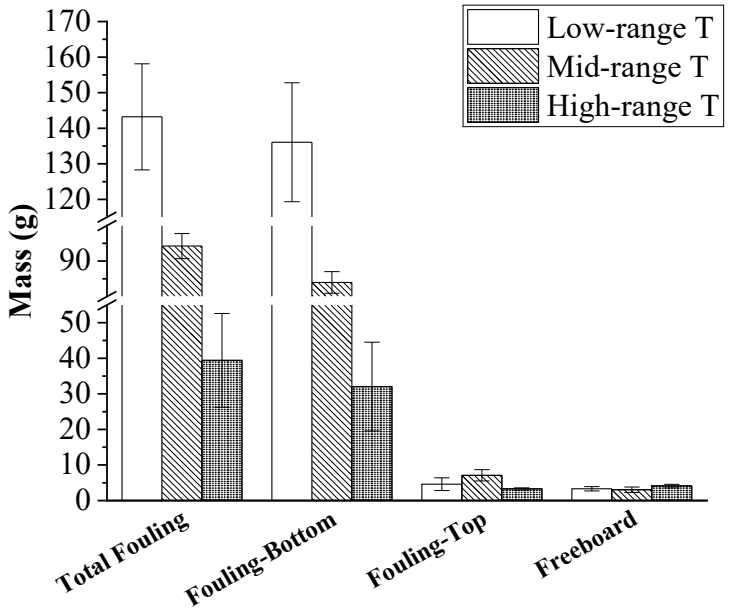

Fig. 2-6. Total amount of wall fouling and its distribution within the column at different operating temperatures. (a) 101 kPa and (b) 2600 kPa.

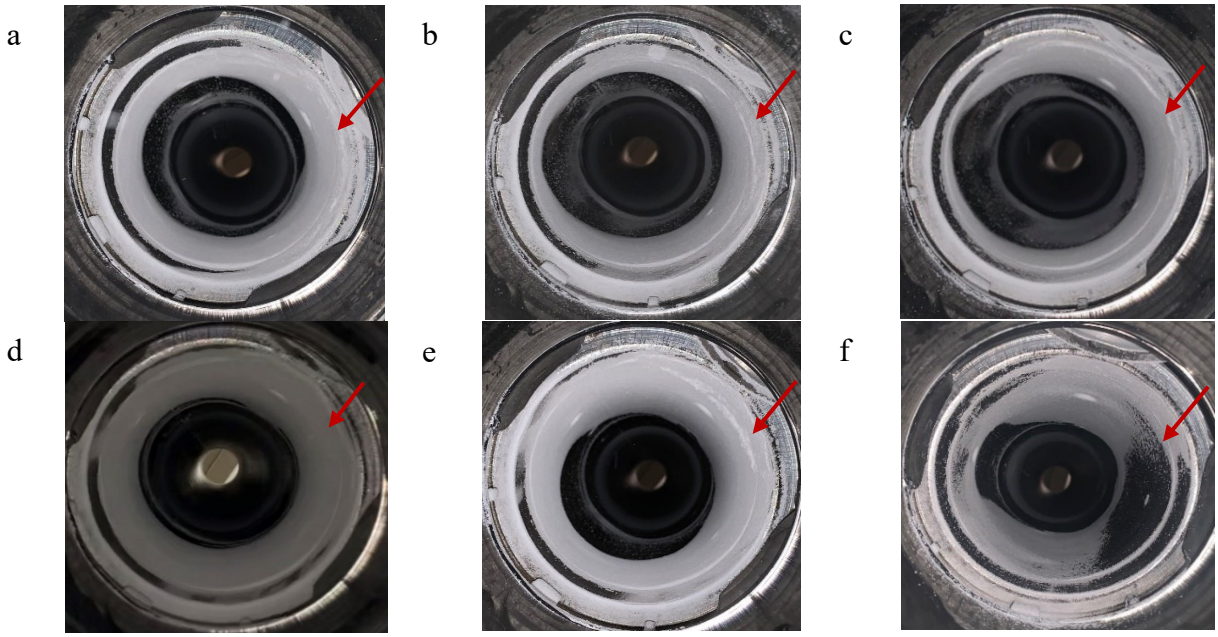

Fig. 2-7. Images taken from inner column wall at different operating conditions. The red arrow shows the *Fouling-bottom* layer (from the distributor plate up to the static bed height). (a) 101 kPa, low-range T, (b) 101 kPa, mid-range T, (c) 101 kPa, high-range T, (d) 2600 kPa, low-range T, (e) 2600 kPa, mid-range T, (f) 2600 kPa, high-range T.

Evaluation of all results demonstrates that the operating temperature had a significant influence on the total wall fouling whereby increasing the temperature, reduced the total wall fouling. Interestingly, a similar influence and trend was observed for the net specific charge of particles in the Bulk for both operating pressures (Fig. 2-3). Moreover, most of the fouled particles were present in the *Fouling-Bottom* region in which they were in contact with the *Bulk* particles. Hence, the reason for any change in the amount of wall fouling with respect to temperature must be due to changes in particles' charge magnitude in the *Bulk* region.

As discussed earlier, the formation and growth of the wall fouling depends on the electrostatic forces between particles and column wall. The presence of less image force on the wall due to a lower net specific charge of *Bulk* particles at higher temperatures could be originated either from an overall decline in electrostatic charge generation or from an increase in magnitude of positively charged particles (i.e., presence of more bi-polar charging). The latter would promote the amount of fouling by the stronger attraction of positively charged particles to the wall in the absence of repulsive force of positive polarity on the wall caused by the image charge of *Bulk* particles. However, formation of positively charged particle layer was not observed in the *Fouling-Bottom* region. Therefore, it is concluded that temperature participated in the reduction

of *Q/m* of Bulk particles by lessening charge transfer during particle-particle and particle-wall collisions. Furthermore, as can be seen in Fig. 2-4, regardless of the operating condition, the magnitude of *Q/m* in all fouling regions did not vary with the exception of *Fouling-Bottom* at 2600 kPa condition at which the net *Q/m* increased with temperature. Since *Q/m* is a ratio of particles' charge to mass, depending on the variation of these values, *Q/m* could increase, decrease, or remain constant. The average Q of the *Fouling-Bottom* region declined by approximately 42.55% (from -6402.98 nC to -3678.14 nC) as temperature increased. Interestingly, the reduction in the mass of fouling in this region that dropped by 72.48% in average, resulted in a higher value for the *Q/m*. For atmospheric condition, the magnitude of Q also declined, but the mass of fouling changed with a similar percentage to keep the *Q/m* constant.

Another indication of less electrostatic charge generation within the bed is the profile of entrained particles' (*Fines*) cumulative charge over time as shown in Fig. 2-8. This figure illustrates that during the first 20 minutes of the fluidization where most of the fine particles (with d_{50}= 86±6 μm) were entrained, the particles had significantly lower charge at the highest pressure (2600 kPa) and the high-range temperature condition. Examination of results in Fig. 2-3 implies that the *Bulk Q/m* for this operating condition is even smaller (-0.06±0.035 nC) than the initial charge of the particles (-0.175±0.05 nC/g). This is an indication of not only a less charge generation but also a change in the charging behaviour of particles at high temperatures. Alsmari et al. [11] also reported a similar change in charging behaviour of glass bead particles when they increased the temperature of a fluidized bed from ambient to 70-75ºC, where they observed even an opposite charge polarity at higher temperature conditions. Conversely, Jantac et al. [16] reported a higher charge generation for PE particles shaken at higher temperatures.

As discussed earlier, the proposed theories of the effect of temperature on electrostatic charge generation reported in literature include variations in the material resistivity, particles shape (i.e., deformation of particles), or energy level of electrons. It is noteworthy to mention that none of the reported works have made direct measurement of these parameters. In this work, we also did not measure the variation of these parameters; however, we did not observe the deformation of particles to result in a higher charge transfer (i.e., higher *Q/m*) that was suggested by Jantac et al. [16]. Since the *Q/m* decline was more significant at high-pressure experiments in which the dominating type of contact is particle-particle collisions (due to smaller gas bubbles), we

conclude that temperature is more influential on particle-particle collisions rather than particle-wall contacts. This conclusion is in agreement with Jantac et al. [16] experiments where they only increased the temperature of the contacting wall and not the tested particles and reported no change in charge transfer. To validate our conclusion, a shake test is recommended to investigate the influence of temperature on electrostatic charge generation for each type of contact (particle-particle or particle-wall). Furthermore, the measurement of the resistivity of the various materials and the magnitude of its change at different temperatures are required in the future work to further determine the significance of this parameter.

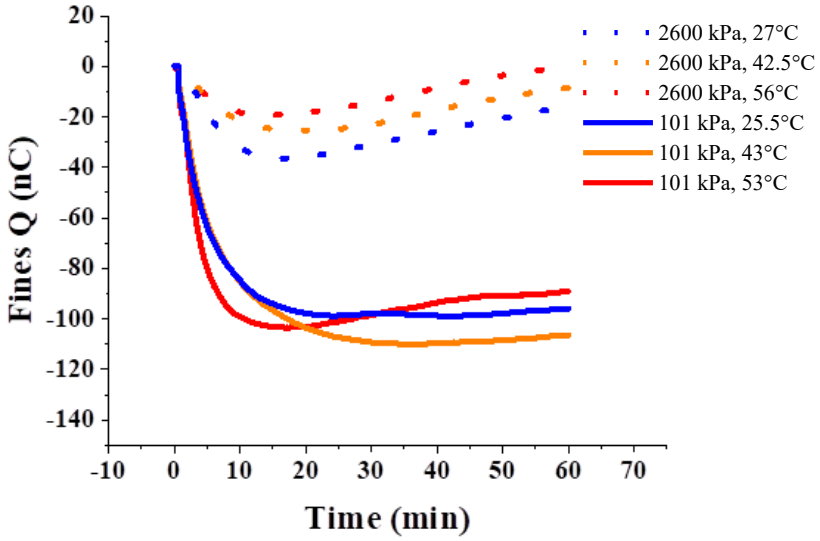

Fig. 2-8. Cumulative charge of *Fines* measured at different operating conditions.

2.4 Conclusion

The influence of operating temperature on the extent of contact electrification of LLDPE particles in a pilot-scale fluidized bed was investigated. It is concluded that for the range of temperature tested (24 to 58°C), the degree of electrostatic charge generation in the fluidized bed was affected which in turn influenced the mass of fouled particles on the column wall. Results showed that at elevated temperatures, net specific charge of fluidized particles in the *Bulk* declined which is a clear indication of the effect of temperature on particles' degree of contact electrification. This in turn reduced the extent of particles migration and fouling on the column wall. To better understand the potential reasons behind the decline of the particles' net specific

charge at elevated temperatures, our future work will focus on performing bench-scale shake tests under a controlled environment (i.e., controlled temperature and relative humidity) to further investigate the effect of temperature on each type of contact (particle-particle vs particle-wall), as well as the measurement of the resistivity of particles at various temperatures.

Acknowledgement

The authors are grateful for the financial support from Univation Technologies, LLC (USA) and the Natural Sciences and Engineering Research Council of Canada (NSERC).

References

[1] G. Hendrickson, Electrostatics and gas phase fluidized bed polymerization reactor wall sheeting, Chem. Eng. Sci., 61 (2006) 1041–1064.

[2] B. D. Fulks, S. P. Sawin, C. D. Aikman, and J. M. Jenkins, Process for reducing sheeting during polymerization of alpha-olefins, United States Patent, No. 4532311, 1985.

[3] W. V. Mark G. Goode, St. Albans; Daniel M. Hasenberg; Thomas J. McNeil, both of Hurricane; Thomas E. Spriggs, Cross Lanes, Method for Reducing Sheeting During Polymerization of Alpha-Olefns, United Stated Patent, No. 4803251, 1989.

[4] K. H. Goode, M.G., Williams, C.C., Hussein, F.D., McNeil, T.J., Lee, Satic Control In Olefin Polymerization, United States Patent, No. 6111034, 2000.

[5] T. Gyung-Hu Song, Charleston W. Va, Aaron S. Rhee, Belle Mead N. J, Gerald G. Lowder, Victoria, Method for reducing sheeting and static charged during polymerization of ethylene plymers, United States Patent, No. 5391657, 1995.

[6] P. Mehrani, M. Murtomaa, and D. J. Lacks, An overview of advances in understanding electrostatic charge buildup in gas-solid fluidized beds, J. Electrostat., 87, (2017) 64–78.

[7] J. Guardiola, V. Rojo, and G. Ramos, Influence of particle size, fluidization velocity and relative humidity on fluidized bed electrostatics, J. Electrostat., 37, (1996) 1–20.

[8] W. O. Moughrabiah, J. R. Grace, and T. B. Xiaotao, Effects of Pressure, Temperature, and Gas Velocity on Electrostatics in Gas-Solid Fluidized Beds, Ind. Eng. Chem. Res., 45 (2009) 320–325.

[9] A. Sowinski, A. Mayne, and P. Mehrani, Effect of fluidizing particle size on electrostatic charge generation and reactor wall fouling in gas-solid fluidized beds, Chem. Eng. Sci., 71 (2012) 552–563.

[10] W. O. Moughrabiah, J. R. Grace, and T. B. Xiaotao, Electrostatics in gas-solid fluidized beds for different particle properties, Chem. Eng. Sci., 75 (2012) 198–208.

[11] T. A. Alsmari, J. R. Grace, and X. T. Bi, Effects of superficial gas velocity and temperature on entrainment and electrostatics in gas-solid fluidized beds, Chem. Eng. Sci., 123 (2015) 49–56.

[12] F. Fotovat, K. Gill, J. R. Grace, and X. T. Bi, Impact of column material on electrostatics and entrainment of particles from gas-solid fluidized beds, Chem. Eng. Sci., 167 (2017) 120–134.

[13] D. Song, F. Salama, J. Matta, and P. Mehrani, Implementation of Faraday cup electrostatic charge measurement technique in high-pressure gas-solid fluidized beds at pilot-scale, Powder Technol., 290 (2016) 21–26.

[14] W. D. Greason, Investigation of a test methodology for triboelectrification, J. Electrostat., 49, (2000) 245–256.

[15] I. A. Harris, M. X. Lim, and H. M. Jaeger, Temperature dependence of nylon and PTFE triboelectrification, Phys. Rev. Mater., 3 (2019) 1–10.

[16] S. Jantač, L. Konopka, and J. Kosek, Experimental study of triboelectric charging of polyethylene powders: Effect of humidity, impact velocity and temperature, Adv. Powder Technol., 30 (2019) 148–155.

[17] Shiquan Lin, Liang Xu, Cheng Xu, Xiangyu Chen, Aurelia C. Wang, Binbin Zhang, Pei Lin, Ya Yang, Huabo Zhao, and Zhong Lin Wang, Electron Transfer in Nanoscale Contact Electrification: Effect of Temperature in the Metal–Dielectric Case, Adv. Mater., 31 (2019) 1–9.

[18] A. Sowinski, F. Salama, and P. Mehrani, New technique for electrostatic charge measurement in gas-solid fluidized beds, J. Electrostat., 67 (2009) 568–573.

[19] D. Song, P. Mehrani, Mechanism of particle build-up on gas-solid fluidization column wall due to electrostatic charge generation, Powder Technol., 316 (2017) 166–170.

Chapter 3 – Investigation of the role of temperature on contact electrification of polyethylene particles

Abstract

This work investigates the role of temperature on contact electrification of polyethylene particles. Particles were shaken at ambient temperature and 60ºC in two stainless steel cups with one having its wall coated with polyethylene particles. Particles in contact with a bare wall did not show a variation in charge transfer when temperature increased; however, contacts with an insulating coated wall resulted in a lower charge generation. A volume resistivity cell was designed and built to measure changes in volume resistivity with temperatures. Although reliable data for particles was not obtained, volume resistivity of different insulating films declined at 60ºC. It was concluded that this drop could increase the mobility of charge carriers and facilitate the electrostatic charge dissipation between particles or to the ground, resulting in a lower charge build-up on particles. This work recommends investigating the role of temperature when ion and material transfer mechanisms are at play.

3.1 Introduction

Electrostatic charge generation is a very complex phenomenon which its mechanism has been a topic of debate among researchers. It has been proposed that three main mechanisms are responsible for contact electrification, namely electron transfer, ion transfer and material transfer. For conductive materials, electrons are transferred from one material to another depending on their work function. According to this mechanism, a metal with a lower work function donates electron to a metal with a higher work function. Although the electron transfer mechanism is valid for metal-metal contacts, it may also be applicable in metal-insulator and insulator-insulator contacts [1]. In these cases, *effective work function* is proposed with the same definition used for conductors. The charge carriers in ion transfer mechanism are naturally ions. Mobile ions which are loosely bound to the ionic materials dissociate and land on the contacting material [2–8]. It is hypothesized that ion transfer to be the main mechanism to transfer charge for an ionic material. Based on this principle, the charge polarity can be manipulated by mobilizing or immobilizing one of the ions on the surface. Also, it has been proposed that surface of materials can lose and donate OH^- and H^+ groups for charge transfer according to their acidity and basicity [9]. Even for non-ionic polymers, OH^- and H^+ ions are assumed to be supplied by the moisture in environment. The moisture present in the environment or on the surface of a material carries excess charge which can be adsorbed or desorbed, and results in charge accumulation or dissipation [10]. Also, it has been claimed that adsorption of water molecules increases the surface conductivity of materials, and thus, improves charge transfer [6]. The collision and friction between two materials can also result in a transfer of fractured materials or impurities on each surface. In such cases, the charge of the transferred material is added to the net charge of the contacting material [11–13]. Pandey et al. [13] also suggested that bond cleavage during contact results in charge generation, and transfer of these fractions leads to a significant charge transfer.

Many parameters have been identified to influence the polarity and magnitude of the generated charge on the surface of materials. They include chemistry of the surfaces in contact [6,14], humidity [15–17], impact velocity [16,18], surface curvature and roughness [19–22], pressure [23,24], temperature [16,25–27], etc. As temperature rises, experimental observations indicate that the electrostatic charge generated on the surface of materials decreases [16,24–29]. Greason [25] investigated the effect of temperature and air relative humidity on contact electrification of a

1.27×10^{-2} m in diameter stainless steel ball when it was rolled against the inner wall of different insulating cylinders with an inner diameter of 4.75×10^{-2} m. The charge developed on the ball was measured at temperatures of 10 to 30°C and relative humidity of 10 to 70%. At any relative humidity below 60%, increasing temperature resulted in a lower charge accumulation on the ball. Greason [25] then proposed a model to describe the rate of net charge build-up after contact which was dependent on material volume and surface resistivity. Based on the model, it was concluded that the decline in the electrical resistance of the insulating materials could be the answer for a lower charge generation at higher temperatures. However, no experimental measurement was conducted to support this idea or show the extent of the influence. Jantac et al. [16] studied the role of temperature and relative humidity in contact charging of polyethylene (PE) particles with $0.8\text{-}1\times10^{-3}$ m diameters in two different apparatuses. In a sliding apparatus, particles rolled on an aluminum slide and fell into a Faraday cup, and in a shaking apparatus, particles were shaken in an aluminum box, and their charge was measured using a Faraday cup. Both apparatuses were inside a glovebox and relative humidity was controlled by a flow of nitrogen and a humidifier. In the experiments with the sliding apparatus, the temperature of the slide was increased to 90ºC, and a marginally higher saturation charge was observed. However, when the temperature of the particles was brought to 90ºC, the saturation charge was doubled. Results for the shaking apparatus showed a similar trend for PE particles, however glass particles experienced a lower saturation charge at relative humidity of 10% which was attributed to the reduction in resistivity of the glass particles according to Greason [25]. Jantac et al. [16] suggested that the pronounced charge of PE particles at elevated temperatures could be due to the increase in energy of surface electrons or particles' softening providing a more contact surface during collisions. They did not provide any data about the surface deformation in their experiments. In the work by Lin et al. [27], they studied the charge transfer between a metal and an insulator using atomic force microscopy (AFM) and Kelvin probe force microscopy (KPFM). The metal was an Au-coated tip of the AFM cantilever that had a diameter of 50×10^{-9} m and was tapping a 100×10^{-9} m in thickness SiO_2, Al_2O_3, AlN or Si_3N_4 on a high doped silicon wafer with a speed of 0.001 s/contact to conduct contact electrification. The whole apparatus was placed in a chamber filled with Ar. Their apparatus was used to individually control the temperature of the tip and the sample from 40 to 130ºC, and hence experiments were performed where one surface could have a higher temperature than another. Based on their experiments, they proposed a

thermionic-emission model which depends on the energy level of electrons and Fermi energy level. In their model, temperature can change the energy level of electrons (and thus the work function) where an electron donor is the material that has a higher energy level. For instance, the charge transfer between AlN and the tip stayed constant by increasing the temperature of both surfaces; however, as the temperature of the tip was raised, the charge transfer increased significantly. They also observed that charge dissipation was faster with an increase in the temperature of the materials.

With the underlying mechanisms of contact electrification being still under debate, the mechanism of how temperature influences the extent of charge transfer necessitates further research. For instance, the majority of the reported research is focused on the electron transfer mechanism, with no reference found where ion transfer or material transfer mechanisms are in play. The aim of this work was to study the influence of temperature on contact electrification of polyethylene particles and to determine the role of volume resistivity. This study is the continuation of our previous work [26] where similar particles showed a decline in electrostatic charge generation and amount of wall fouling in a gas-solid fluidized bed operated at temperatures up to 60ºC compared to ambient temperatures at atmospheric and 2600 kPa pressures. Particles that fouled on the fluidization column wall and those stayed in the bulk of the bed had a mean diameter of 360 µm and 650 µm, respectively. Therefore, a similar particle size range was selected for the purpose of this study.

3.2 Material and method

The particles used in this work were a commercially produced linear low-density polyethylene (LLDPE) resin, and their properties are detailed in Table 3-1. The objective was to investigate the charging behaviour of these particles at 23ºC and 60ºC. To accomplish this, shake tests were conducted in an OHAUS orbital shaker (model ISLD04HDG) equipped with adjustable temperature control up to 65°C (Fig. 3-1). Measurements of the particle charge were taken before and after shaking using a Faraday cup connected to a digital Keithley electrometer (Model 6514). To minimize the initial charge of the samples, prior to placing them in the shaker, an SMC ionizer (model 1ZF10R) was employed to effectively reduce the initial charge of the particles. All aforementioned equipment was placed in a glove box filled with nitrogen in order to perform the experiments under a controlled temperature and relative humidity (4±1%) environment.

The experiments involved two cylindrical cups; one cup (ID: 6×10^{-2} m, height: 4.4×10^{-2} m) was made of stainless steel while the second stainless steel cup (ID: 7×10^{-2} m, height: 5×10^{-2} m) inner wall was coated with PE resin. The bare stainless steel (SS) cup was of a similar material as the column material for fluidization runs in our previous work [26] and was used to represent particle-wall contacts. The coated cup was made to give a better understanding when the inner fluidization column wall was fouled with particles, and particles in the bulk of the bed collided with the particles on the wall. Therefore, the coated cup was prepared by adhering the same LLDPE resin sieved to have a size of 360 μm in average to an aluminum tape. Then, the aluminum tape was affixed to the inner wall of a stainless-steel cup. Importantly, the coated particles were significantly smaller than the particles used in the shake tests, ensuring that only the coated particles came into contact with the cup's inner surface. The coated particles were from the same resin used in the fluidization experiments having an average particle diameter similar to the particles that had fouled on the fluidization column wall. The shake tests were conducted using particles with various narrow size distributions, as listed in Table 3-1. Most of the particles within the fluidized bed had a mean size larger than 600 μm. Hence, for the purpose of this study, particles within this size range were selected for the experiments.

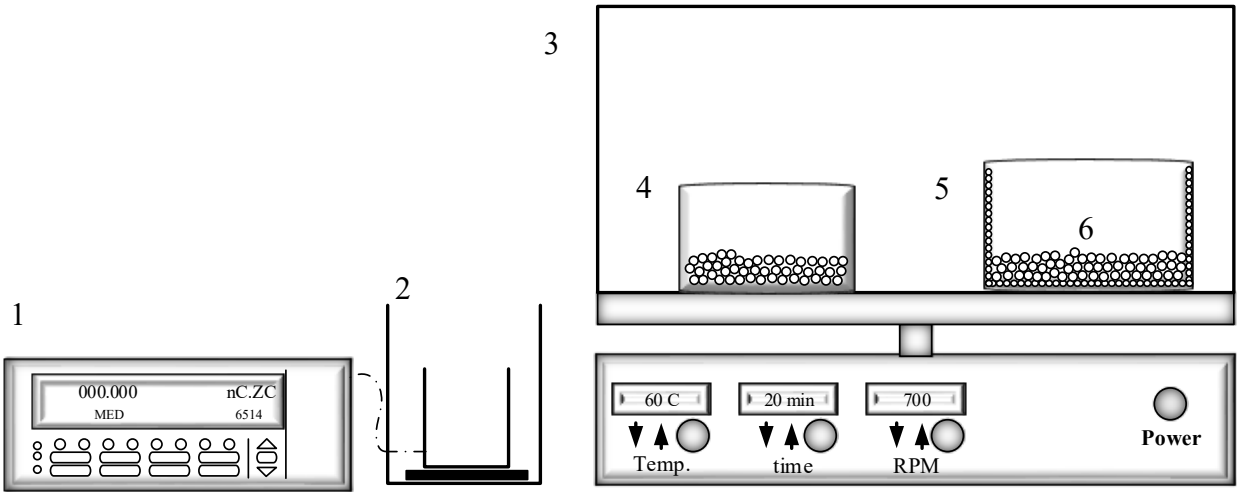

Fig. 3-1. A schematic of the apparatus inside the glove box filled with N_2, 1- Electrometer, 2- Faraday cup, 3- Shaker, 4- SS cup, 5- Coated cup, 6- PE particles.

Table 3-1. Operating conditions of the shake tests used in this study.

Particle Type	Particle Density (kg/m^3)	Particles Size Range (µm)	Mean Particle Diameter (µm)	Particles Mass per trial (g)
Linear low-density PE	917	1400<PE<1700	1550 µm	2
		1000<PE<1400	1250 µm	
		850<PE<1000	925 µm	
		600<PE<850	725 µm	
		300<PE<425	360 µm	

At the beginning of each experiment, both cups were neutralized to remove any residual charge by grounding them and using the ionizer. This step was particularly important for the coated cup, as insulating materials can retain electrostatic charge on their surfaces, potentially affecting the magnitude and direction of charge transfer. Upon placing particles in each cup, the ionizer was used again so that the initial charge of particles would become minimal. Nevertheless, the net specific charge measured after neutralizing the particles was on average -0.25±0.05 nC/g. For experiments at 60°C, the shaking process commenced 45 min after neutralizing the particles in order to allow the particles and the cup to reach the desired temperature. Preliminary testing showed no variation in particles charge for shaking times greater than 20 min at a speed of 700 RPM, and thus this duration was chosen for all the experiments. Upon completion of the shaking period, the particles charge was measured by transferring them into a Faraday cup. All the tests were replicated at least 4 times to ensure reproducibility, and the error bars represent standard deviation.

3.3 Volume Resistivity

A volume resistivity measurement cell was built in-house according to ASTM D257 guidelines (Fig. 3-2). This cell consists of three electrodes: a potential electrode where a high potential difference is applied, a current electrode to measure the current passing through the sample, and a guard electrode that is grounded. This measurement cell was utilized to measure volume resistivity of different samples at 23°C and 60°C. For measurements at 60°C, the cell was left inside the shaker to allow both the cell and the sample to reach the desired temperature.

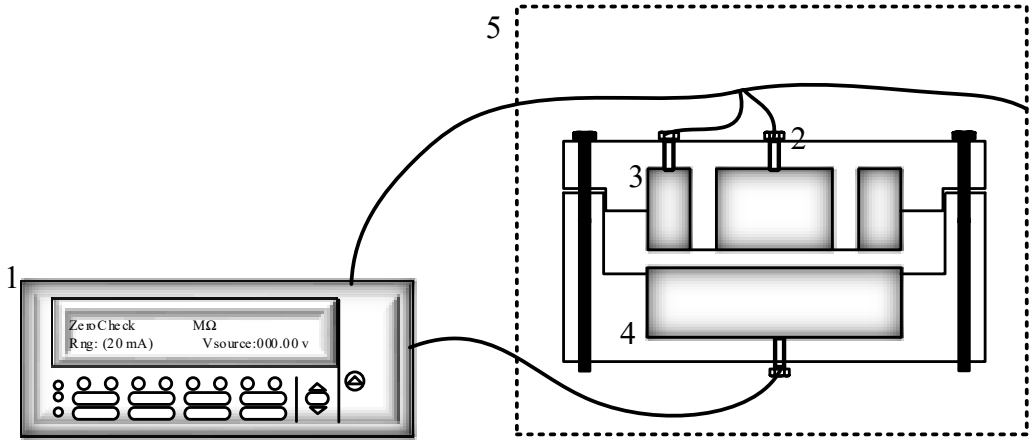

Fig. 3-2. Volume resistivity cell and the connections. 1- Electrometer, 2- Current electrode, 3- Guard electrode, 4- Potential electrode, 5- A grounded copper cylinder that prevents any interference from environment.

Since the aim was to measure the volume resistivity of samples of PE resin at the two operating temperatures used in the shake test, it was necessary to first make a measurement with an empty cell. The purpose of this measurement was to make sure that current does not go through the void spaces between the PE particles. This would confirm that volume resistivity of air is higher than that of PE particles which was the case at ambient temperature. However, as the temperature increased, the volume resistivity of air decreased. Consequently, during empty-cell measurements conducted at 60°C, it was observed that the volume resistivity of the particles could not be measured due to current signals passing through the air within the cell. To address this issue, it was decided to utilize a thin film instead of powders for the volume resistivity measurements. Three films made of insulating material were tested with properties shown in Table 3-2.

Table 3-2. Insulating film used in volume resistivity measurements.

Material	**Thickness (mm)**
Nylon 6/6	0.794
LDPE	1.59
LLDPE	0.07

For PE particles at 23°C, the particles were poured into the measurement cell until a certain height was reached. To ensure accurate current signal measurements, the cell was then placed inside a grounded shield to prevent potential electrical interference from the surrounding environment. A potential difference of 5000 VDC was applied to the potential electrode of the cell. The current flowing through the sample was measured using a digital Keithley electrometer

(Model 6517A), which had a sensitivity of 10 aA (10×10^{-18} A). The resistivity of the sample was calculated by using the following equation:

$$R = \frac{V}{I} \qquad \text{Eq. (3-1)}$$

In Eq. (3-1), V is the applied potential difference in V, I is the measured current in A, and R is the resistance of the sample in Ω. Since resistivity depends on the dimensions of the sample, volume resistivity, $\rho\ [\Omega.m]$, was defined as:

$$\rho = RS, \text{ and } S = A/L \qquad \text{Eq. (3-2)}$$

Where A is the corrected surface area (m^2) of the current electrode according to ASTM D257, and L is the thickness of the sample in m.

Fig. 3-3 shows a typical current signal obtained when a potential difference of 5000 VDC was applied to the sample. The current signal exhibits a sudden decline in the absorption current region which according to Lee et al. [30] could be due to the electric polarization within the sample. After a certain duration, the current reaches a steady state condition. The volume resistivity was subsequently calculated using the steady state current.

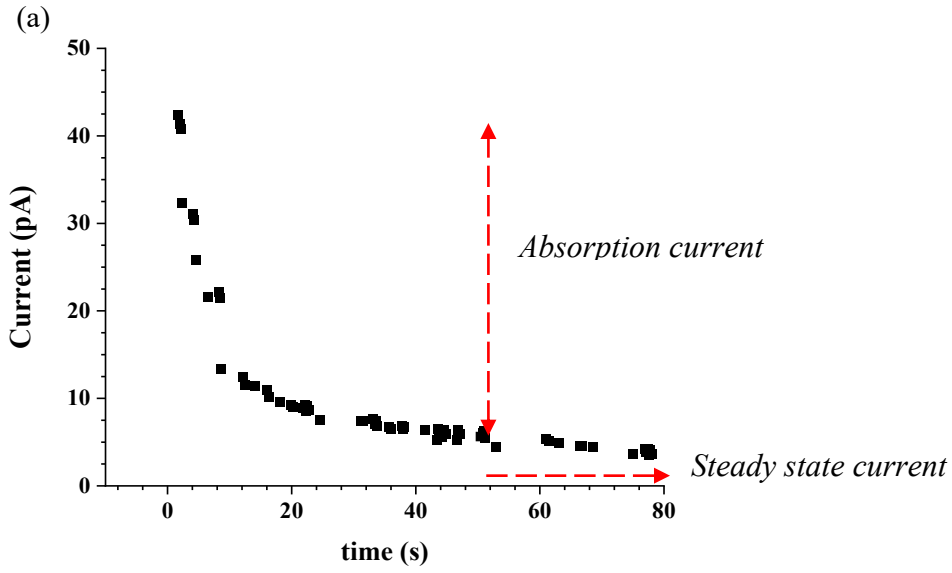

Fig. 3-3 Current signal measurement over time from the volume resistivity measurement cell. Sample: LDPE film, temperature: 23°C, potential difference: 5000 VDC.

3.4 Results and discussion

3.4.1 Shake test

After 20 min shaking of PE particles at 23°C and 60°C, the final generated electrostatic charge was measured. During a shake test, electrostatic charge is generated due to particles colliding with each other and with the wall of the cup. Since a Faraday cage measures the net charge of particles, the charge originated from particle-particle contacts cannot be determined. Therefore, the reported results represent the net charge generated only from particle-wall contacts. As depicted in Fig. 3-4, regardless of the temperature, PE particles acquired a net negative polarity in contact with the stainless-steel cup wall which is in accordance with the differences in the work functions of the two materials [31]. Results illustrate that the difference in the electrostatic charging of particles was negligible between 60 ºC and 23 ºC. These findings are consistent with those reported by Lin et al. [27], which demonstrated that contact electrification of insulators in contact with a conductive material is not notably influenced by increasing the temperature of both materials. Based on electron transfer mechanism, Lin et al. [27] proposed that when the surface temperature of both the conductor and the insulator in contact increases, there will be no change in the difference in the energy level of electrons, and therefore, no change in charge transfer will occur.

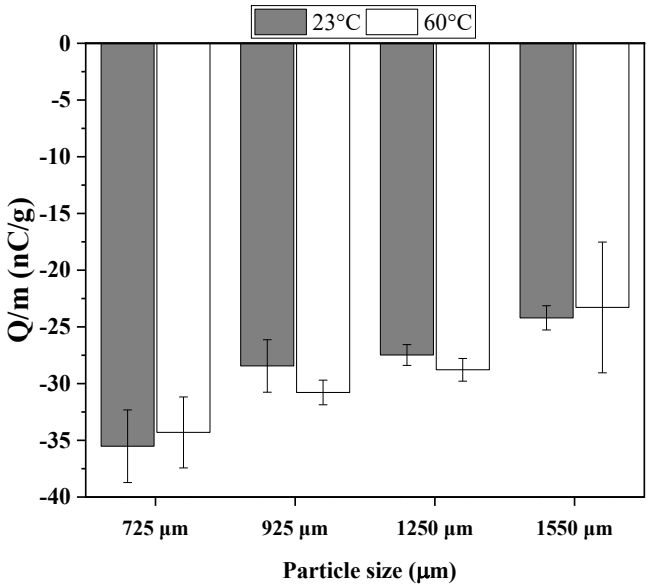

Fig. 3-4 The net specific charge of the PE particles shaken in the SS cup at different temperatures.

In Fig. 3-5, it is observed that when the temperature increased from ambient to 60ºC, most of the particles in contact with the coated cup acquired a reduced net specific charge. Since the particles acquired a net negative polarity, particles on the cup wall must have obtained a positive polarity. The decline in net specific charges seen here is in agreement with our previous work in which similar particles were fluidized at temperatures up to 60ºC, and the Q/m of particles in the bulk of the bed declined at higher temperatures [26].

Three proposed mechanisms reported in literature that may explain the influence of temperature include change in energy level of electrons, softening of particles, and change in volume resistivity. The change in energy level of electrons was found to be valid for metal-insulator contacts, as demonstrated in Fig. 3-4. However, results in Fig. 3-5 imply that insulator-insulator contacts result in lower charge generation, even when the temperatures of the cup and particles are similar. Although particle softening could potentially lead to an increase in the level of charge transfer, as suggested by Jantac et al. [16], this phenomenon was not observed in the present study.

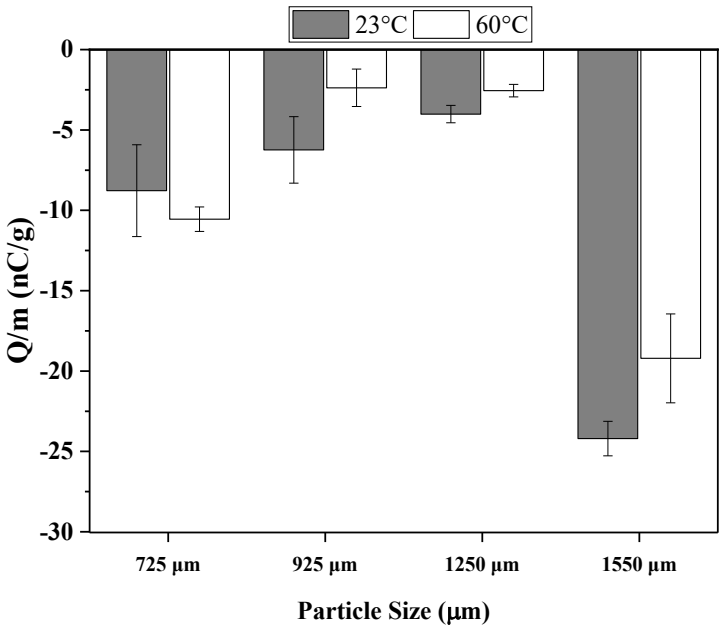

Fig. 3-5 The net specific charge of the particles shaken in the coated cup at different temperatures.

3.4.2 Volume resistivity

At ambient temperature, the average volume resistivity of Nylon, LDPE, LLDPE, and the PE resin used in the shake test, were 6.8×10^{14}, 3.79×10^{16}, 1.25×10^{17} and 2.52×10^{16} Ω.cm, respectively. After increasing temperature to 60°C, Fig. 3-6 illustrates that the volume resistivity of the insulating film was approximately 180, 2 and 13 times smaller than that at ambient temperature for Nylon, LDPE and LLDPE, respectively.

In metals, an increase in temperature leads to increased atomic vibration, which impedes the mobility of free electrons in the material, resulting in a higher resistivity [32]. However, in insulators, there are no free electrons in the conduction band, and as the resistivity of a material declines, it could imply that charge carriers have more mobility as the result of a higher temperature, and thus, a higher charge dissipation will occur between particles charged with different polarities, between negative and positive sites on the surface of the particles or to the ground. Hence, a lower net specific charge will be generated after contact electrification.

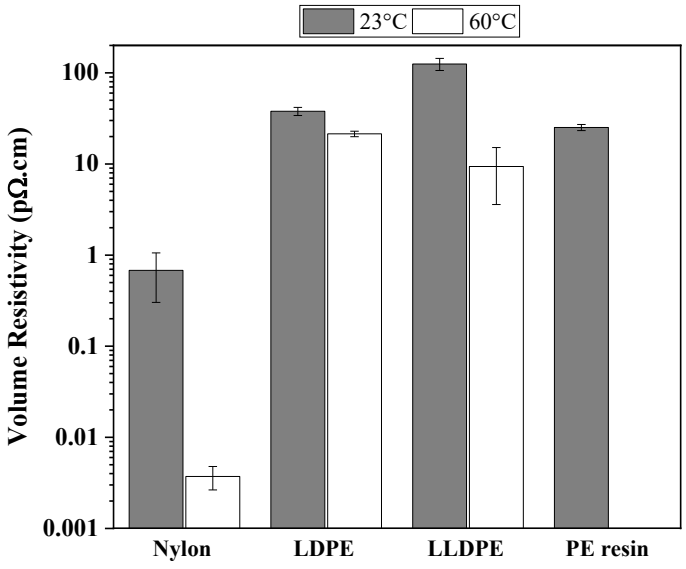

Fig. 3-6 Volume resistivity of various insulating films and PE resin at 23 and 60°C.

3.4.3 Discussion

The mobility of charge carriers, including electrons and mobile ions, can be analyzed by examining the current signal data obtained during volume resistivity measurement. To analyze

the data, a curve fitting approach, as proposed by Robinson [33], could be employed using the following equation:

$$I_{(t)} = I_{ss} + \frac{I_1}{\left(1 + \frac{t}{\tau_1}\right)^2} \qquad \text{Eq. (3-3)}$$

In Eq. (3-3), I is the measured current at a given time (A), I_{ss} is the steady state current (A), I_1 is the charge carrier number (A), τ_1 is the time constant utilized to calculate charge carrier mobility (s), and t is time (s). Charge carrier mobility can also be estimated by the following equation [33]:

$$b \approx \frac{d^2}{\tau_1 V} \qquad \text{Eq. (3-4)}$$

Where d is the gap between electrodes (m), and V is the applied potential difference to the measurement cell (V).

Fig. 3-7 shows the current signal data for the LDPE film at 23 and 60°C when a 5000 VDC potential difference was applied to the sample for 80 s. Using Eq. (3-3) to curve fit the data, the time constant τ for each operating temperature was determined. Even though the measurement time was not sufficiently enough for the current to reach complete steady state, the calculated τ which corresponds to the rate of decline in the absorption current at 23°C was approximately 85% lower than that at 60°C which is evident from Fig. 3-7b. According to Eq. (3-4) a lower time constant results in a higher charge mobility, leading to increased charge dissipation on the particles.

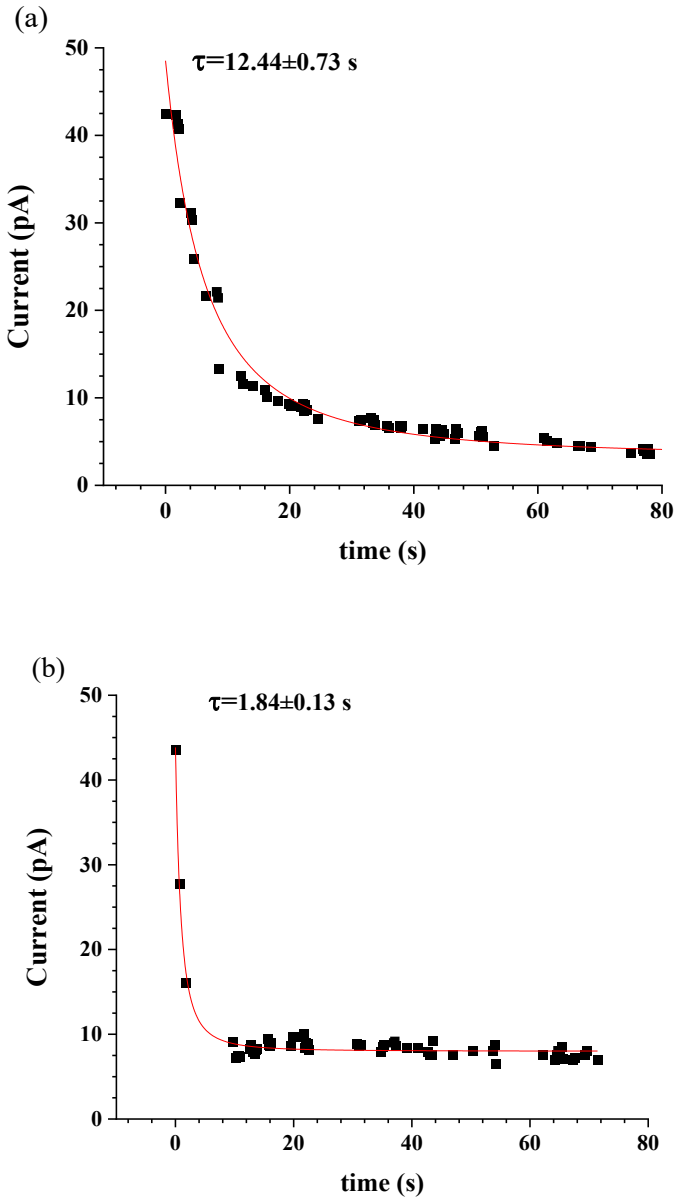

Fig. 3-7 Current versus time during volume resistivity measurements for LDPE film, (a) 23°C and (b) 60°C. The solid line shows the best curve fitted line based on Eq. (3-3).

In addition to volume resistivity, the maximum charge that a particle can possess is proportional to the breakdown voltage of the surrounding gas at which gas ionization occurs [34]. The formed gas ions can be deposited on the surface of the charged particles and reduce the accumulated surface electrostatic charge, a phenomenon known as gas dissipation. It has been recognized that the breakdown voltage of a gas depends on temperature [35–37]. Research findings from Uhm et al. [35] indicate that the breakdown voltage of air dropped by approximately 20% when temperature was raised from ~24°C to ~100°C. Hence, it could be concluded that another

potential factor contributing to the observed results in the shake tests is the fact that more charge dissipation occurred through gas due to a lower breakdown voltage of air at 60°C.

In summary, the two main reasons for a lower electrostatic charge generation at higher temperatures could be attributed to the changes in materials volume resistivity and breakdown voltage of the surrounding gas. A lower volume resistivity is claimed to facilitate charge dissipation between particles or through the ground whereas a lower breakdown voltage helps dissipate electrostatic charge to the nearby gas. Since in the experiments conducted, both factors could influence the results simultaneously, it is impossible to distinguish the significance of each factor. For the SS cup, particles did not exhibit a noticeable change in their charging behavior when temperature increased which could imply that the potential decline of breakdown voltage and its influence on the final net specific charge was negligible. Furthermore, according to electron transfer mechanism, when both objects are heated to a similar temperature, there should be no change in the energy levels of electrons, and thus, no change in charge transfer between two objects which was valid for metal-insulator contacts as shown in Fig. 3-4. However, this mechanism was not valid for insulator-insulator contacts where the mobility of the charge carriers differed at higher temperatures. For the coated cup, since the effect of breakdown voltage in our experiments is ruled out, the charge transfer could be influenced only by charge dissipation between particles or to the ground as a result of a change in volume resistivity. This could suggest that volume resistivity was playing a larger role in lowering the charge generated at higher temperatures for insulator-insulator contacts. It should be noted that other mechanisms such as ion transfer and material transfer could possibly influence the contact electrification of particles at higher temperature which are out of the scope of this study. This brings us to the fact that ion and material transfer mechanisms require more investigation, particularly regarding the effect of temperature.

3.5 Conclusion

This study aimed to investigate the influence of temperature on contact electrification of PE particles and other insulating materials. Shake tests were conducted to analyze the electrostatic charge generation of different types of contacts including insulator-insulator and metal-insulator contacts, under two operating temperatures of 23 and 60°C. The results showed that for metal-insulator contacts increase in temperature had a negligible influence on the extent of charge

generation, which aligns with the electron transfer mechanism. However, increasing temperature suppressed the build-up of electrostatic charge during insulator-insulator contacts. Results showed that volume resistivity of the tested insulators was inversely proportional to temperature, resulting in a higher charge carrier mobility and charge dissipation to the ground while temperature increased. Breakdown voltage of the surrounding gas was claimed to be another factor influencing contact electrification even though it had negligible effect in the tested temperature range. Among the three main mechanisms for charge transfer, the focus has only been on electron transfer mechanism while ion transfer and material transfer mechanisms could also be affected by temperature which necessitates further research.

Acknowledgement

The authors would like to thank Univation Technologies, LLC (USA) and Natural Sciences and Engineering Research Council of Canada (NSERC) for their financial support. We also acknowledge the assistance from Dr. Kelly Robinson from Electrostatic Answers.

References

[1] S. Matsusaka, H. Maruyama, T. Matsuyama, M. Ghadiri, Triboelectric charging of powders: A review, Chem. Eng. Sci. 65 (2010) 5781–5807.

[2] A.F. Diaz, D. Wollmann, D. Dreblow, Contact Electrification: Ion Transfer to Metals and Polymers, Chem. Mater. 3 (1991) 997–999.

[3] A.F. Diaz, Contact Electrification of Materials: The Chemistry of Ions on Polymer Surfaces, J. Adhes. 67 (1998) 111–122.

[4] A.F. Diaz, R.M. Felix-navarro, A semi-quantitative tribo-electric series for polymeric materials : the influence of chemical structure and properties, 62 (2004) 277–290.

[5] L.S. Mccarty, A. Winkleman, G.M. Whitesides, Ionic Electrets : Electrostatic Charging of Surfaces by Transferring Mobile Ions upon Contact, 12 (2007) 4075–4088.

[6] L.S. McCarty, G.M. Whitesides, Electrostatic charging due to separation of ions at interfaces: Contact electrification of ionic electrets, Angew. Chemie - Int. Ed. 47 (2008) 2188–2207.

[7] F. Galembeck, T.A.L. Burgo, L.B.S. Balestrin, R.F. Gouveia, C.A. Silva, A. Galembeck, Friction, tribochemistry and triboelectricity: Recent progress and perspectives, RSC Adv. 4 (2014) 64280–64298.

[8] D.J. Lacks, T. Shinbrot, Long-standing and unresolved issues in triboelectric charging, Nat. Rev. Chem. 3 (2019) 465–476.

[9] P.E. Shaw, C.S. Jex, Tribo-electrocoty and Friction, 1928.

[10] R.F. Gouveia, F. Galembeck, Electrostatic charging of hydrophilic particles due to water adsorption, J. Am. Chem. Soc. 131 (2009) 11381–11386.

[11] K.-I. Tanoue, A. Ema, H. Masuda, Effect of Material Transfer, J. Chem. Eng. Japan. 32 (1999) 544–548.

[12] H.T. Baytekin, B. Baytekin, J.T. Incorvati, B.A. Grzybowski, Material transfer and polarity reversal in contact charging, Angew. Chemie - Int. Ed. 51 (2012) 4843–4847.

[13] R.K. Pandey, H. Kakehashi, H. Nakanishi, S. Soh, Correlating Material Transfer and Charge Transfer in Contact Electri fi cation, (2018).

[14] M. Taghavivand, A. Sowinski, P. Mehrani, Triboelectric effects of continuity additives and a silica catalyst support on polyethylene fluidized bed wall fouling, Chem. Eng. Sci. 245 (2021) 116882.

[15] A. Giffin, P. Mehrani, Effect of gas relative humidity on reactor wall fouling generated due to bed electrification in gas-solid fluidized beds, Powder Technol. 235 (2013) 368–375.

[16] S. Jantač, L. Konopka, J. Kosek, Experimental study of triboelectric charging of polyethylene powders: Effect of humidity, impact velocity and temperature, Adv. Powder Technol. 30 (2019) 148–155.

[17] R.D. Cruise, K. Hadler, S.O. Starr, J.J. Cilliers, The effect of particle size and relative humidity on triboelectric charge saturation, J. Phys. D. Appl. Phys. 55 (2022).

[18] H. Watanabe, M. Ghadiri, T. Matsuyama, Y.L. Ding, K.G. Pitt, H. Maruyama, S. Matsusaka, H. Masuda, Triboelectrification of pharmaceutical powders by particle impact, Int. J. Pharm. 334 (2007) 149–155.

[19] Z. Chen, Y. Lu, R. Manica, Q. Liu, Curvature effects on liquid–solid contact electrification, Nano Energy. 89 (2021) 1–8.

[20] C. Xu, B. Zhang, A.C. Wang, H. Zou, G. Liu, W. Ding, C. Wu, M. Ma, P. Feng, Z. Lin, Z.L. Wang, Contact-electrification between two identical materials: Curvature effect, ACS Nano. 13 (2019) 2034–2041.

[21] M.B. Neagoe, Y.E. Prawatya, T. Zeghloul, L. Dascalescu, Influence of surface roughness on the tribo-electric process for a sliding contact between polymeric plate materials, IOP Conf. Ser. Mater. Sci. Eng. 174 (2017) 6–12.

[22] J.W. Lee, W. Hwang, Theoretical study of micro/nano roughness effect on water-solid triboelectrification with experimental approach, Nano Energy. 52 (2018) 315–322.

[23] D. Song, F. Salama, J. Matta, P. Mehrani, Implementation of Faraday cup electrostatic charge measurement technique in high-pressure gas-solid fluidized beds at pilot-scale, Powder Technol. 290 (2016) 21–26.

[24] W.O. Moughrabiah, J.R. Grace, X.T. Bi, Effects of Pressure, Temperature, and Gas Velocity on Electrostatics in Gas-Solid Fluidized Beds, Ind. Eng. Chem. Res. 48 (2009) 320–325.

[25] W.D. Greason, Investigation of a test methodology for triboelectrification, J. Electrostat. 49 (2000) 245–256.

[26] M.I. Nimvari, A. Sowinski, P. Mehrani, Effect of temperature on triboelectrifcation of polyethylene particles in a pilot-scale pressurized gas-solid fl uidized bed, Powder Technol. 405 (2022) 117524.

[27] S. Lin, L. Xu, C. Xu, X. Chen, A.C. Wang, B. Zhang, P. Lin, Y. Yang, H. Zhao, Z.L. Wang, Electron Transfer in Nanoscale Contact Electrification: Effect of Temperature in the Metal–Dielectric Case, Adv. Mater. 31 (2019) 1–9.

[28] I.A. Harris, M.X. Lim, H.M. Jaeger, Temperature dependence of nylon and PTFE triboelectrification, Phys. Rev. Mater. 3 (2019) 1–10.

[29] T.A. Alsmari, J.R. Grace, X.T. Bi, Effects of superficial gas velocity and temperature on entrainment and electrostatics in gas-solid fluidized beds, Chem. Eng. Sci. 123 (2015) 49–56.

[30] H.G. Lee, J.G. Kim, Volume and surface resistivity measurement of insulating materials using guard-ring terminal electrodes, Energies. 13 (2020).

[31] D. Song, P. Mehrani, Mechanism of particle build-up on gas-solid fluidization column wall due to electrostatic charge generation, Powder Technol. 316 (2017) 166–170.

[32] S.J. Ling, J. Sanny, W. Moebs, University Physics Volume 2, 12th Media Services, 2018.

[33] K. Robinson, Improved Measurement of the Apparent and Steady-State DC Surface Resistivity of Sheets and Films, Proc. Electrost. Soc. Am. Annu. Meet. Electrost. 2011. (2011) 1–5.

[34] J. Cross, Electrostatics: Principles, Problems and Applications, 1987.

[35] H.S. Uhm, S.J. Jung, H.S. Kim, Influence of gas temperature on electrical breakdown in cylindrical electrodes, J. Korean Phys. Soc. 42 (2003) 989–993.

[36] E. Sili, J.P. Cambronne, A New Empirical Expression of the Breakdown Voltage for Combined Variations of Temperature and Pressure, Int. J. Aerosp. Mech. Eng. 6 (2012) 611–616.

[37] X. Liu, Z. Shi, G. Yang, X. Yan, Experimental study on breakdown voltage of high pressure and high temperature helium gas between parallel electrodes, Ann. Nucl. Energy. 110 (2017) 1224–1231.

Chapter 4 – Triboelectrification of a Metallocene Catalyst in an Atmospheric Polyethylene Fluidized Bed

Abstract

The persistent challenge of triboelectrification in gas-solid fluidized bed reactors for polyethylene production prompted this study to investigate the influence of a common type of metallocene catalyst along with its individual components on the contact electrification of linear low-density polyethylene (LLDPE) in a fluidized bed. At ambient temperature and atmospheric pressure, the triboelectrification of a catalyst base (amorphous dehydrated silica), an active and deactivated co-catalyst (methylaluminoxane), an active and deactivated metallocene catalyst, and a metallocene catalyst mixed with two continuity additives were investigated while being pneumatically injected into a LLDPE gas-solid fluidized bed. While at 100 ppm concentrations of the added powders, not a significant influence was observed, at 1000 ppm concentrations, amorphous silica, methylaluminoxane, and deactivated metallocene catalyst exhibited a negative polarity or a reduced net positive charge in the fluidized bed. Notably, the presence of active methylaluminoxane significantly suppressed the magnitude of wall fouling. While presence of an active metallocene catalyst contributed to an increase in the extent of wall fouling, it did not affect the net charge in the bed. Finally, the introduction of a mixture of continuity additives along with the metallocene catalyst effectively mitigated the substantial formation of wall fouling attributed to the catalyst's presence. This study suggests considering methylaluminoxane as a static control agent, as it avoids the adverse effects associated with continuity additives while also enhancing the catalyst's activity. Furthermore, this work confirms that the chemistry of the catalyst in PE production process is influential in changing the bed net charge and in turn the extent of the wall fouling.

4.1 Introduction

Contact electrification or triboelectrification originates from collision among solids, and solids with neighbouring surfaces including the containing vessel walls as well as other surfaces and materials. Contact electrification is potent to pose operational challenges in a variety of industrial processes. For instance, in polymer industry and particularly in polyethylene (PE) production processes, the presence of adverse effects of triboelectrification are identified to be important. In PE manufacturing, a common method involves employing gas-solid fluidized bed reactors, typically operating at pressures reaching 3000 kPa and temperatures up to 110ºC [1]. Within these reactors, PE particles become fluidized by the flow of monomers and comonomers. Catalyst particles are introduced into the reactor to initiate the exothermic polymerization reaction. Within the reactor environment, the multitude of collisions occurring between particles (i.e., catalyst and PE particles) and between particles and the reactor wall leads to the accumulation of electrostatic charge on the particle surfaces. Consequently, the resulting electric field originated from the surface charges prompts particles to stick together, or adhere to the reactor wall, causing the heat of the reaction to not be efficiently dissipated. This in turn leads to the particles to fuse together and melt and form thick layer of molten particles on the reactor wall, known as *sheets* [2–4]. Alternatively, the particles might coalesce into large agglomerates due to adhesion or the merging of fused particles within the reactor bed. The formation of *sheets* can originate from various sources [3]. The PE particles could be adhering to the reactor wall and undergoing gradual growth until they reach sintering temperature and agglomerate. On the other hand, the catalyst particles could adhere to the reactor wall, inducing an increase in wall temperature due to the heat of exothermic polymerization reactions. The latter then prompts PE resins to adhere to the developing *sheets*. *Sheets* have also been observed to form in the expansion region of the fluidized bed reactor which could arise from the entrainment of fine particles, including both PE and catalyst particles [3]. Ultimately, the formation of sheets and particle agglomerates may lead to reactor shutdown, and hence, pose great operational challenges and economic losses.

The concept behind contact electrification of dielectrics remains a subject of ongoing debate because the charge carriers involved in contact electrification could potentially include electrons, ions, or even material components. For conductive materials it is well understood that electrons are responsible for charge transfer and thus depending on the work function of the materials in

contact one may lose or gain electrons [5,6]. Electron transfer can also take place in insulators despite lacking electrons in the conduction band, leading to the definition of an effective work function similar to conductive materials. While measuring work functions in metals is reliable, it is more challenging for insulators due to the influence of restructuring, defects, and adsorbates on their surface states [7]. Conversely, determining the acid-base properties of insulating surfaces is more straightforward and may serve as reliable predictors of the type and extent of contact electrification between insulators [7,8]. Studies indicate a strong link between the work functions of polymers and the constants governing acid-base interactions. This connection proposes that surface acidity and basicity align with surface acceptor and donor states. This suggests that the materials work function could relate their corresponding acid/base values such that higher acid/base ratios (or more electron affinity) imply larger material work functions and thus a more negative charge on the surface [9,10].

In insulators, electron transfer is not always the dominant charge carrier. It has been observed that when the surface of an insulator is functionalized with ionic compounds, the surface appears to possess a charge with the same polarity as the covalently bound ions due to the transfer of the mobile counterions after a contact [11]. Furthermore, the presence of moisture on the surface of materials could also facilitate transfer of charge carriers. For ionic materials a water bridge could be formed at the point of contact where the mobile ions can diffuse through this layer [12]. As for non-ionic materials, it is shown that even hydrophobic materials have moisture on their surface (in the form of localized islands or a thin film) [13]. This thin layer or localized island of water on the surface collects hydroxide in the Stern layer while keeping hydronium solvated, causing the polymers to exhibit a negative zeta potential. Then, when the polymers come into contact, hydroxide and hydronium ions quickly reach equilibrium within the water bridge. The polymer that attracts hydroxide more, develops a net negative charge [11,12]. It is also proposed that presence of moisture on the surface of insulators affects their conductivity, and thus, facilitates the transfer of charges on the surface or to the ground [13,14]. Finally, as two distinct materials come into contact or are rubbed together, it is possible for a small amount of each material to transfer and adhere to the other surface. This process, known as material transfer, can consequently affect the electrostatic charge present on each surface [15,16]. None of the three primary mechanisms – electron transfer, ion transfer, and material transfer – have been proven to be the definitive cause of charge transfer in insulators. Consequently, managing the generation of

electrostatic charge poses a considerable challenge where controlling the level of charge is crucial.

Regardless of the underlying mechanisms of triboelectrification, contact electrification primarily occurs at surfaces of the materials, and thus, understanding the influence of a material's surface properties such as surface chemistry and the chemical structure of molecules becomes critical. For instance, in commercial polyethylene gas-phase process, when the catalyst chemistry is changed the issues of wall sheeting and particle agglomeration are reported to be reduced or become augmented. Such observations clearly point to the fact that the presence and the surface chemistry of catalyst particles could play a pivotal role in the extent of electrostatic charge generation in polyethylene gas-phase reactors. Hence, investigating the role of catalyst and its chemical composition becomes essential in understanding the extent of electrostatic charge development in such systems.

In polyethylene production process, a variety of catalysts are used depending on the desired properties of the produced polymer. Phillips Petroleum developed a commercial process for the heterogenous chromium catalyst discovered in 1951. In general, heterogeneous catalysts are usually supported on materials including silica, aluminum oxide or magnesium chloride. The support is essential for achieving a free-flowing catalyst powder that produces polymer particles with the appropriate size distribution, preventing the formation of fine powder or particle agglomerates, and providing a large surface area for polymerization reaction [17]. Phillips catalyst is capable of producing high-density polyethylene (HDPE) as the most widely used form of polyethylene. Typically, Phillips catalysts are supported on silica, which undergoes impregnation with a chromium compound. Subsequently the catalyst becomes activated by calcination in dry air or oxygen. The chemical structure of this catalyst is depicted in Fig. 4-1 [18,19].

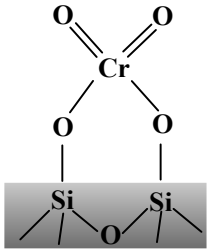

Fig. 4-1. An example of chemical structure for a Phillips catalyst.

Silyl chromate catalysts were initially developed by the Union Carbide Corporation (UCC) to produce HDPE using a gas-phase UNIPOL^{TM} process. The silyl chromate catalysts yield polymer distributions that are broad, extending to both high and low molecular weight ranges and featuring a distinctive high molecular weight tail which indicates a potential second type of active site. This catalyst can be supported on silica, and its chemical structure is illustrated in Fig. 4-2 Fig. 1-17[18,20].

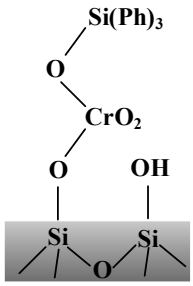

Fig. 4-2. An example of chemical structure for a silyl chromate catalyst.

Another type of catalyst widely used is the Ziegler-Natta (ZN) catalyst. ZN catalysts possess multiple active sites, each with distinct characteristics such as propagation rates, comonomer reactivity ratios, and stereoselectivities. Heterogeneous ZN catalysts consist of titanium trichloride ($TiCl_3$) or titanium tetrachloride ($TiCl_4$) supported on magnesium chloride ($MgCl_2$), aided by co-catalysts like triethylaluminum ($AlEt_3$). Magnesium chloride stands out as the optimal support material due to its close resemblance in atomic size, shape, and coordination number to titanium [21]. Titanium tetrachloride catalysts, when directly bonded to oxide supports like silica or alumina, exhibit limited effectiveness in polymerization [22]. A silica/$MgCl_2$ support offers a solution by providing precise particle size control while maintaining the beneficial properties of an $MgCl_2$ base, crucial for controlling particle morphology [23]. Studies [24–32] show that $TiCl_4$ and $TiCl_3$ possess various actives sites on different lattice planes of $MgCl_2$. Fig. 4-3 shows just on example of mononuclear $TiCl_4$ on (110) $MgCl_2$ and its alkylation by $AlEt_3$ [25].

a)

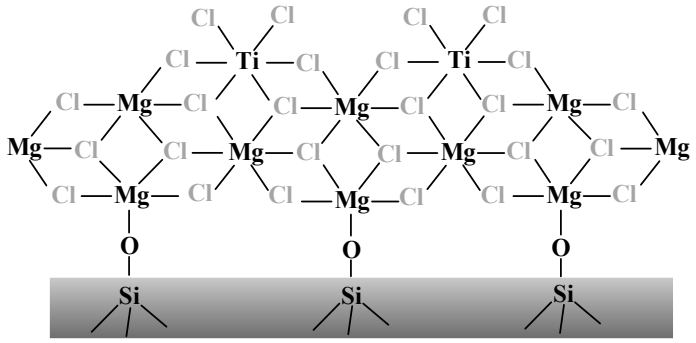

b)

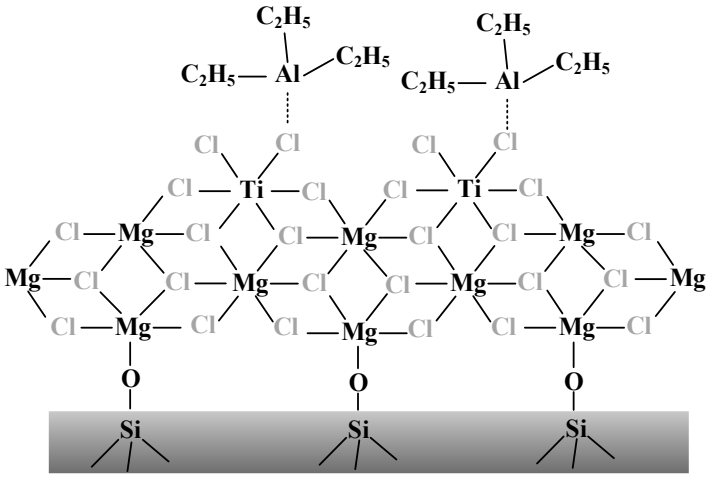

Fig. 4-3. Schematic illustration of an example of mononuclear $TiCl_4$ (a) and active site precursors (b) on the (110) $MgCl_2$ supported on silica.

A metallocene (MCN) catalyst is a specific type of organometallic compound frequently employed in polymerization reactions, especially in the production of specific plastic materials like PE and polypropylene (PP). MCN catalysts are renowned for their exceptional efficiency and precision in controlling the polymerization process, resulting in polymers with precisely defined properties. They offer precise control over the molecular weight, structure, and branching distribution of the polymer [33]. These types of catalysts comprise of a metallocene compound, which is typically a transition metal complex, in combination with a cocatalyst, often an aluminum compound. The metallocene compound itself consists of a cyclopentadienyl ligand bonded to a transition metal like titanium, zirconium, or hafnium. Particularly for ethylene polymerizations, the zirconium catalyst is more active than other catalysts at temperatures above

50ºC [21]. In the context of MCN catalysts, an ion exchange compound, composed of a cation and a non-coordinating anion, is combined with the catalyst (Fig. 4-4). This association results in the metallocene complex, which is a cation paired with a stable anion. Experimental evidence strongly supports the idea that all active centers in MCN catalysts are cationic in nature [17,33,34].

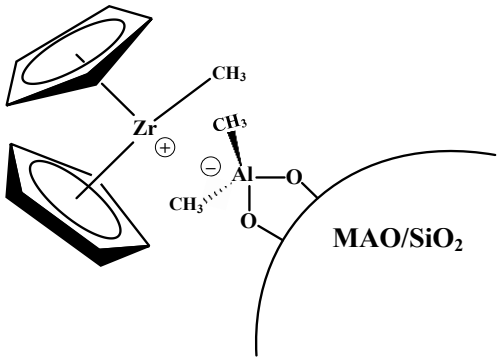

Fig. 4-4. An example of a typical MCN catalyst structure. A metal complex (a cation) on a metallocene catalyst. Silica is the catalyst base and methylaluminuxane (MAO) is the cocatalyst (an anion).

To activate a MCN catalyst, methylaluminoxane (MAO) is utilized. MAO is an oligomer with an oligomerization degree ranging from 5 to 28, characterized by repeat units of [-Al(CH3)-O-]. Although various studies have proposed different structures for MAO, it remains unknown and is often described (Fig. 4-5) as an oligomeric chain, either cyclic or linear, consisting of [-Al(CH3)-O-] units [21,35,36].

a) b)

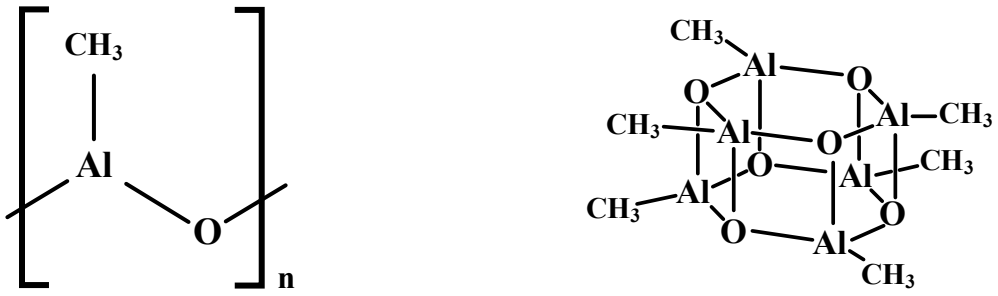

Fig. 4-5. Linear (a) and cage (b) structure of MAO.

In gas-phase reactors like UNIPOL™ process, MCN catalysts need to be supported. MCN catalysts have been effectively supported on various inorganic compounds, including SiO_2, $MgCl_2$, and Al_2O_3. The choice of support and the method of supporting the MCN and MAO significantly influence catalyst performance [17]. Silica is one of the widely used, cost-effective

catalyst supports that provides a high surface area (for enhanced interaction between the catalyst and reactants) and can be easily functionalized to improve catalytic activity or selectivity [37–39]. Fig. 4-6 shows different types of silanol and siloxane groups that could be present on a silica support particle [40].

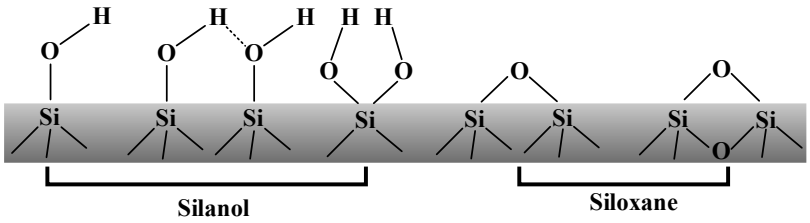

Fig. 4-6. Silanol and siloxane groups on a silica support particle.

In relation to contact electrification of catalysts in commercial polyethylene gas-solid fluidized beds, Table 4-1 summarizes findings from various works reported in literature from commercial reactor operations, describing the type of catalyst used and the charge polarity measured using electrostatic probes. None of these reported works have provided any discussion or results on the relationship between the type of catalyst used and the degree of bed charging observed.

Table 4-1. A summary of findings on the common types of catalyst used in industrial gas-phase polyethylene process and the resulting bed charge polarity measured by electrostatic probe.

PE Density (kg/m^3) Melt Index	**Catalyst Type**	**Charge polarity from probe**	**Finding**
0.918 1 [2]	5.5 parts $TiCl_4$, 8.5 parts $MgCl_2$, 14 parts C_4H_8O (tetrahydrofuran) deposited on 100 parts Silica 955 dried at 800ºC treated with 4 parts triethylaluminium (TEAl) and activated with 35 parts tri-n-hexyl aluminum	+	Adding water and increasing the concentration of H_2 decreased the charge in the bed.
0.918 1 [1]	Same as [2]	+	Adding $AlCl_3$ decreased the positive polarity and/or changed the polarity to a negative value.
	5 parts $TiCl_4$, 8 parts $MgCl_2$, 16 parts C_4H_8O (tetrahydrofuran) and 1.7 parts $AlCl_3$ deposited on 100 parts Silica 955 dried at 600ºC treated with 5 parts TEAl and activated with 32 parts tri-n-hexyl aluminum and 12 parts diethylaluminum chloride	–	

0.918 1 [4]	Same as [2]	+	A sudden increase in ethylene concentration increased the voltage read by the probe from 0 to 6000 V in 10 minutes.
-, -, [41]	$MgCl_2$, $TiCl_3$ (AA), $HfCl_4$, CAB-O-SIL® TS-610	+	Sudden decrease in static charge when the condense mode started
0.925 0.5 [42]	Zr based Metallocene with MAO	±	Bed polarity changed between +75 V to –75 V. Adding water made the polarity negative.
	Titanium based supported on silica containing magnesium chloride, triethyl aluminum, diethyl aluminum chloride, tri-n-hexyl aluminum, and tetrahydrofuran.	+	Adding water dropped the probe reading from +3000 V to zero. The addition of TEAl to the seed bed shifted the bed polarity to a negative value. TMA was used instead of TEAl for metallocene based catalyst since TEAl was known to cause extensive sheeting.
0.918 1-1.2 [43]	Silica Supported Constrained Geometry Metallocene Catalyst (CGC) 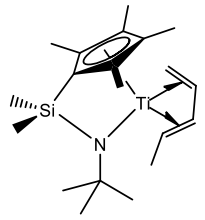 CGC-7	–	Adding aluminum distearate and ethoxylated amine to mitigate fouling.

The understanding of electrostatic charge generation and its impact on gas-solid fluidized beds and in particular industrial gas-phase polyethylene process has been well reported in literature. In relation to this process, several studies, including ours, have investigated the influence of various factors such as fluidization gas velocity, polyethylene particle size and its distribution, gas relative humidity, vessel wall material, fluidization pressure and temperature, as well as addition of static control agents or deactivated catalysts [44–53]. All of these studies have explored the electrostatic charging of polyethylene resin alone (i.e., in the absence of any catalyst or any continuity additives) with the exception of two works conducted by our research group [52,53]. Sowinski and Mehrani [52] investigated the influence of a deactivated metallocene catalyst and its support (i.e., amorphous silica) on the degree of polyethylene fluidized bed wall fouling. It was shown that as 1.0 g of the particles injected into the fluidized bed, they had possessed a large

magnitude of surface charge. Consequently, the resulting higher net charge in the bed promoted the fouling of the polyethylene particles on the column wall. Taghavivand et al. [53] examined the role of introducing different static control agents, known as continuity additives (CA), into a polyethylene fluidized bed. They found that the extent of wall fouling is directly linked to the net specific charge of particles within the bulk of the fluidized bed such that reducing the bulk net charge was identified as a key strategy to mitigate the formation of wall fouling. Furthermore, they found that non-ionic materials as injected into the fluidized bed could be positive or negative inducers in the bed based on their proton affinity whereas for ionic materials the functional groups on their surface govern the induced polarity.

Since there is a lack of understanding on the role of catalyst in formation of sheeting and particles' agglomeration in gas-phase PE reactors, the objective of this study was to examine how the presence of a catalyst along with its other elements, influences the charging behavior of a polyethylene bed. This investigation focused on a common type of metallocene catalyst. In addition, the role of components within the catalyst was individually assessed. This spanned from the catalyst base to the active co-catalyst, and the active catalyst. Since in commercial processes, catalysts are pneumatically introduced into the reactor, a similar technique was utilized in this work in which also made it possible for the electrostatic charge of all the tested samples to additionally be examined while entering the fluidized bed. Hence, this work also aimed at studying the electrostatic charging behavior of the tested catalyst due to its dry pneumatic conveying.

4.2 Materials and Experimental Method

This work utilized an atmospheric gas–solid fluidization system, illustrated in Fig. 4-7, featuring a horizontal solid conveying line. Details regarding the fluidization column and its compartments can be referenced in prior works [54,55]. The stainless-steel fluidization column had a diameter of 0.1 m and height of 1.3 m and was connected to two Faraday cages positioned at the top and at the bottom of the column. Both Faraday cages measured the charge of particles using Keithley 6514 digital electrometers (electrometer 1&2). The upper Faraday cage accommodated a filter bag to capture elutriated particles (referred to as *Fines*) for subsequent charge-to-mass ratio (*Q/m*) and size distribution measurements. To facilitate the collection of fluidizing particles (referred to as *Bulk*) at the conclusion of the fluidization run with a minimal particle handling, a

modified knife gate valve acted as a sliding, perforated, distributor plate. Particles that fouled on the wall were categorized into three regions, from distributor plate to static bed height (*Fouling-Bottom*), from static bed height to expanded bed height (*Fouling-Top*), and from the expanded bed height to the exist of the column was called *Freeboard*. At the end of each experiment, the fouling in each region was dislodged into the bottom Faraday cup by using a stream of dry air to measure the particles' mass and electrostatic charge.

The powder samples were introduced into the fluidization column through a pneumatic conveying line that entered the column at a height of 0.06 m above the distributor plate. The conveying line was a stainless-steel tube and had an inner diameter of 4.57×10^{-3} m (equivalent to ¼ inch tube) that was similar to a typical commercial PE process catalyst injection line. With a total length of 5 meters, the tube included two smooth bends featuring radii of 0.25 m and 0.33 m to direct the injected sample to the fluidization column. The measurement of the initial and final charge of the powders upon their entry and exit from the conveying tube involved connecting the electrically isolated tube directly to a 6514 Keithley digital electrometer (electrometer 3). This allowed for the conversion of the current signal read by the electrometer off the conveying tube into powders' electrostatic charge. Further details about this technique can be found in our prior publications [56,57].

Industrial grade nitrogen with approximately 0% relative humidity and 20±1°C temperature, served as the fluidization gas and the conveying gas. The conveying gas velocity was 15 m/s.

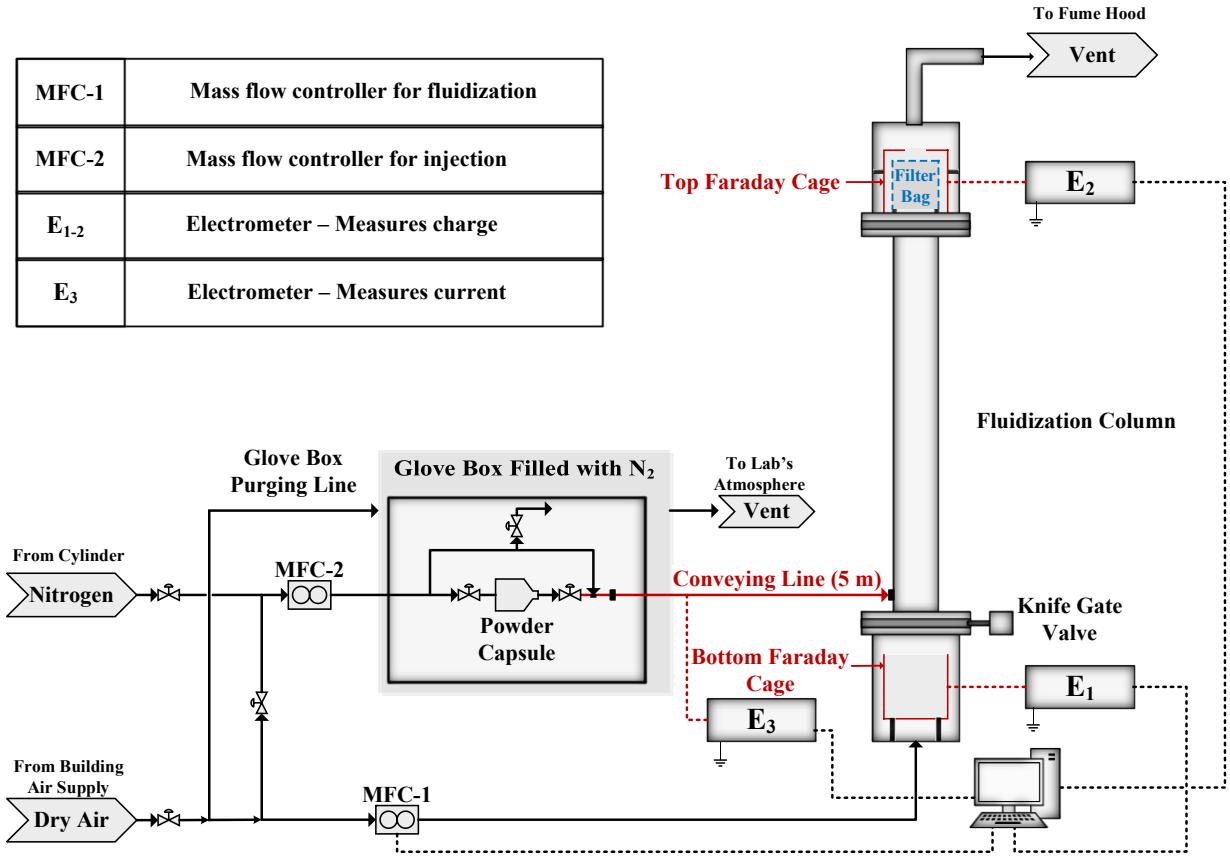

Fig. 4-7. Schematic of the atmospheric fluidization system, pneumatic conveying line, and measurement techniques.

Live and deactivated catalyst samples were prepared by our industrial partner. Each sample was loaded into individual capsules, and then pressurized to 202 kPa using nitrogen. Prior to each experiment, the capsule was attached to the conveying line inside a glove box filled with nitrogen, as depicted in Fig. 4-7. To prevent any alteration in the molecular structure of the samples caused by moisture and oxygen interaction, it was essential to ensure the absence of both elements in the system. Therefore, prior to introducing the PE particles into the fluidization column, the pneumatic conveying line and the column were purged with dry air (RH<2%) for 18 hours. After adding the polyethylene particles into the fluidization column, the bed and conveying tube underwent a nitrogen purge lasting approximately 20 minutes. The fluidization gas velocity was first increased to minimum fluidization velocity (U_{mf}) at which the batch injection of the samples into the bed was performed. Once the sample was introduced, the fluidization gas was raised to 1.5 U_{mf}, corresponding to a bubbling flow regime. The fluidization process spanned 60 minutes, and each experiment was replicated between 2 to 4 times.

4.2.1 Materials

The fluidization particles used in this study were linear low-density polyethylene (LLDPE) directly received from a commercial plant with the properties shown in Table 4-2. The particles were neutralized using an SMC ionizer (model 1ZF10R) before being added to the fluidization column to ensure that their initial charge remained consistent for all experiments.

Table 4-2. Properties and operating conditions related to the fluidizing particles.

Fluidization Particle	Sauter Mean Size	True Density	Mass Loading	U_{mf}	Initial Charge (nC/g)
(LLDPE)	1051 µm	917 kg/m^3	1007 g	0.19 m/s	-0.056±0.18

Table 4-3 outlines the types of samples pneumatically conveyed into the polyethylene bed. MCN catalyst was used since it is one of the common types of catalyst systems widely employed in PE manufacturing industries. This catalyst offers unique advantages and contributes to the production of PE with specific properties tailored to diverse applications. Prior to assessing the active and deactivated MCN catalyst, the influence of individual components of the catalyst including the catalyst base (amorphous silica) and the cocatalyst (methylaluminoxane) supported on silica was examined to pinpoint the contribution of each component to change in magnitude and polarity of contact electrification within the fluidized bed. One approach to mitigating electrostatic charge in PE commercial reactors is to introduce static control agents to the bed via the catalyst injection line alongside the catalyst or through a separate line. They are also referred to continuity additives (CA) as they help industry continue the process of reactors without a need for reactor shutdown due to *Sheeting*. Therefore, analyzing a MCN catalyst mixed with a continuity additive provides valuable insights into how these additives interact within the bed, particularly in contact with PE or catalyst particles. Hence, the MCN catalyst mixed with a continuity additive was also tested. Finally, the study of a deactivated catalyst could also be of interest in a case where some catalyst particles become deactivated because of the presence of any impurities or components that would poison the catalyst in the reactor, or in the catalyst injection lines.

Table 4-3. The samples tested in this study together with their size and mass loadings.

Sample	Acronym	dp_{10}, dp_{50}, dp_{90} (µm)	Mass loading (g)
Dehydrated amorphous silica (catalyst base)	Si	12±2	0.1, 1.0

Active Methyaluminoxame supported on Silica	MAO	45±3 90±5	
Active Metallocene catalyst (Fig. 4-4)	MCN		
Active Metallocene catalyst + Continuity additive (fatty amine + metal stearate, <3wt%)	MCN+CA		
Deactivated MAO	De MAO		
Deactivated MCN	De MCN		

In the initial set of experiments, 0.1 g of samples was introduced into the bed of PE particles. This quantity was determined based on the productivity of the catalyst (i.e., 10000 g-PE/g-cat), representing a concentration of 100 ppm in the reactor. Also, in prior work [53] 0.1 g injection of particles was sufficient to observe the effects of CAs on PE charging behavior within the same system. Furthermore, a mass loading of 1.0 g (i.e., 1000 ppm) was also studied to observe the influence of concentration of the injected powder on the static charging of the PE bed.

4.3 Results and discussion

The electrostatic charging tendency of each powder due to its conveying was first evaluated by determining the polarity and magnitude of the charge gained at the exit of the conveying line. This analysis was followed by testing the particles charge distribution and extent of wall fouling when the bed PE resin was fluidized with and without any powder present.

4.3.1 Pneumatic injections

In pneumatic conveying systems, particles undergo charging resulting from collisions between particles themselves, and between particles and the tube wall. In the case of pulse injection, where particles move at approximately the same velocity (i.e., particles move as a plum), particle-particle contacts become less frequent, and a significant portion of collisions occur with the tube wall. Hence, the final electrostatic charge acquired by the particles largely originated from the contacts of particles with the conveying tube wall.

In this work, all samples were introduced into the fluidized bed through a conveying tube, implying that the charge accumulation primarily originates from interactions with the tube wall surface. Assessing the charge within the pneumatic conveying tube offers insights into how the samples charged when in contact with a conductive substance prior to entering the fluidized bed where PE particles (i.e. an insulator) are present. Fig. 4-8 illustrates the final charge status of the

samples upon their entry into the bed (i.e., at the exit of conveying tube). Each column includes the results for 100 ppm and 1000 ppm concentrations, and error bars indicate standard deviation.

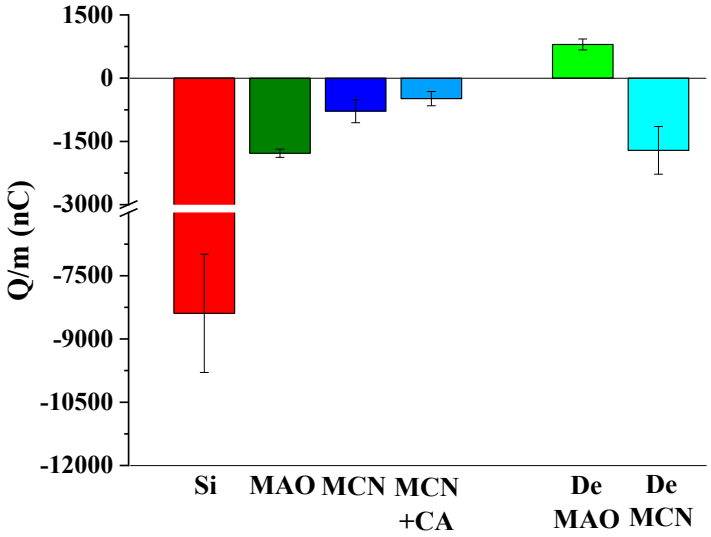

Fig. 4-8. The net specific charge (*Q/m*) of various samples upon existing the conveying tube and entering the fluidized bed.

Silica particles demonstrated a negative polarity and the highest magnitude of charge within the tube. This result is consistent with the differences between the work function values of silica and stainless steel, being 5.2 eV and 4.5 eV, respectively [58,59]. Furthermore, silica particles feature silanol and siloxane groups on their surface, with a pKa that spans from 2.1 to 10.3 [60], indicating their acidic nature, and thus, their tendency to lose protons and acquire negative polarity from the stainless-steel tube upon contact.

MAO particles also exhibited a negative polarity, albeit with a smaller charge magnitude (approximately five times less) than silica. This large difference in the degree of charging suggests that the silica that is located at the core of each particle was effectively covered by MAO. On the other hand, De MAO displayed a positive polarity. This shift in charge polarity could be attributed to the fact that methyl groups were replaced with oxygen after the deactivation process which leads to formation of aluminum oxide on the surface. Aluminum oxide has a work function of 3.8 eV [61], while stainless steel's work function stands at 4.5 eV, leading to the generation of a positive charge on the surface of the De MAO.

MCN catalyst, in comparison, acquired a lower charge than MAO, implying that the majority of the interactions occurred between the tube and the catalyst elements on its surface rather than with the underlying MAO molecules. Furthermore, MCN+CA exhibited a lower charge than the MCN catalyst alone, signifying the potency of CAs in mitigating the catalyst charging (a t-test was also carried out and a p value of less than 0.05 was observed between MCN and MCN+CA results). This could be justified by the fact that in earlier work [53], the pneumatic injections of a fatty amine and a metal stearate in a stainless-steel tube concluded in a charge density of lower than -30 and -200 nC/g, respectively. Therefore, the mixture of MCN catalyst and CAs was expected to reduce the charge build-up because the entire catalyst surface was not in contact with the conveying tube wall. However, in the deactivated form the magnitude of the charge increased substantially.

MCN particles in the deactivated form showed a negative polarity with similar magnitude as MAO particles. This could indicate that the dimerized cyclopentadiene on the surface exhibits a negative charge inducing behaviour in contact with the stainless-steal tube.

4.3.2 Fluidization

Inside a fluidized bed with PE resin of a wide size distribution, various contact scenarios arise. These include interactions between smaller and larger PE particles, contacts among PE particles of similar size, interactions of the incoming powders with PE particles, and the contact of all particles with the fluidization column wall. It is fundamental to assess these diverse possibilities in terms of particles charge transfer, and their tendency to migrate towards the column wall, remain within the bulk of the bed, or become elutriated. Fig. 4-9a illustrates a control volume containing solely PE resin within the fluidization column and the particles' possible locations. In our previous work [59] the particle layer formation on a conductive fluidization column is well discussed. We had concluded that particles in the bulk of the bed could exhibit positive and negative polarities. Due to induction charging, the bulk particles induce their charge onto the conductive stainless-steel column, maintaining the column wall polarity similar to that of the bulk particles. As depicted in Fig. 4-9a, if the net charge of the bed is positive, the initial layer formed on the wall owns a positive polarity due to the Coulomb force between the negatively charged column wall and the positively charged particles in the bulk (Fig. 4-9b). The second layer presents two potential scenarios. In the first scenario, if the charge magnitude of the first

fouled layer is substantial enough, it attracts negatively charged particles from the bulk. Consequently, the second layer adopts a negative polarity (Fig. 4-9c). The second scenario unfolds when the charge within the bulk is significant, causing the induced charge on the column to be potent enough to attract positively charged particles onto the first layer. In this case, the Coulomb force between the first layer and positively charged second layer might not be compelling enough to repel the particles, allowing the formation of the second positive layer on top of the first positive layer (Fig. 4-9d).

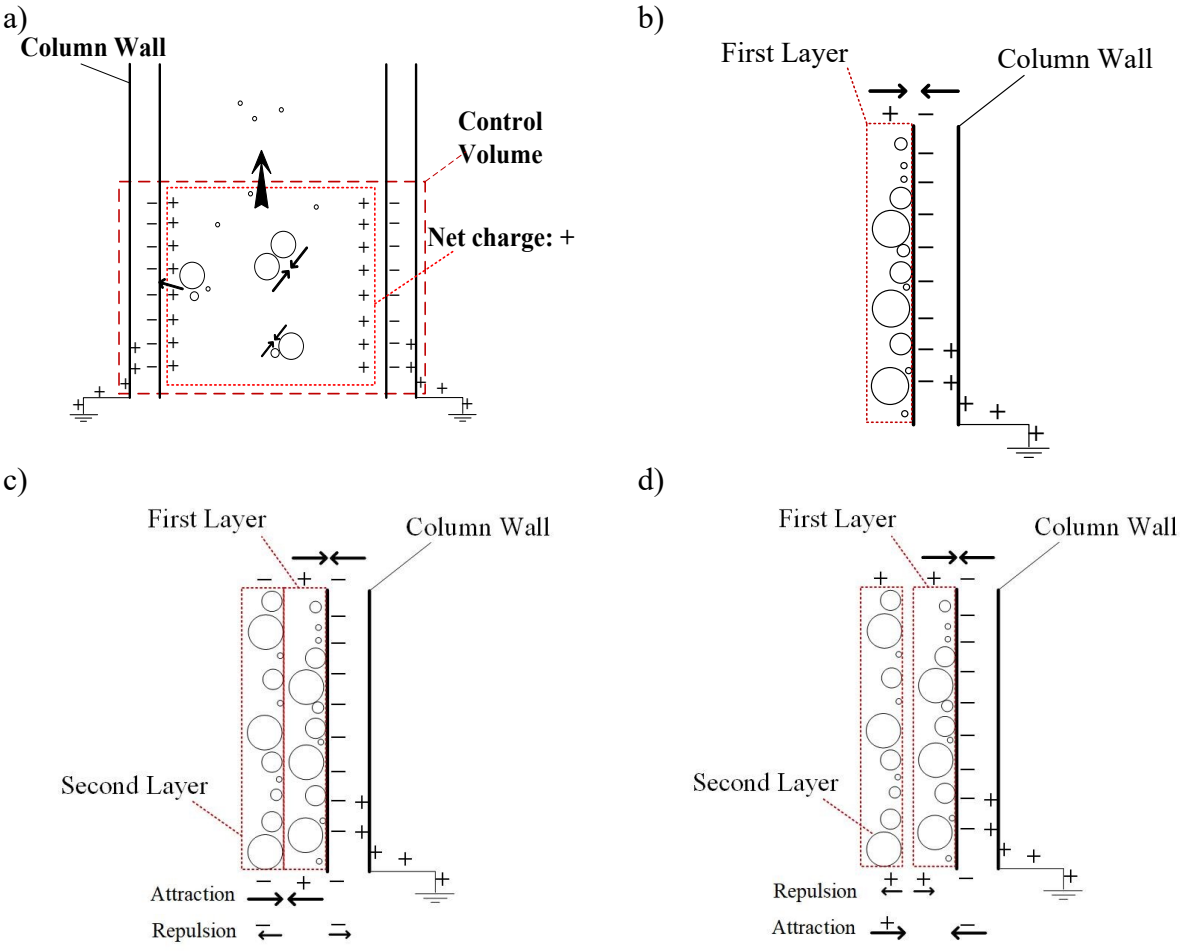

Fig. 4-9. Particle layer formation on a conductive wall of a fluidized bed. a) net charge of particles in the bed and the resulted induced charge on the fluidization column wall, b) first layer wall fouling formation due to the attractive force between the oppositely charged objects, c) second layer wall fouling formation where the attraction between particles is stronger than the repulsion between the bed particles and the wall, d) the second layer formation where the attraction between the particles and the column wall is stronger than the repulsion between

similarly charged particles.

The introduction of the powders of a different chemistry into the PE bed could have various effects on the charge buildup in the system. These additional particles may potentially mitigate or elevate the net charge of the bulk particles, a consequence of their interactions with either PE particles or the stainless-steel column wall. Consequently, this could lead to a reduction or an elevation in the induced charge on the wall. Alternatively, because of their small size, the particles could entrain from the bed without significantly altering the net specific charge of the fluidized particles. Another potential outcome arises if the added powders adhere to the column wall and depending on their charge magnitude and polarity potentially influence the formation of fouled layers.

It should be noted that there is a large size distribution in the polyethylene resin, and thus, particles with smaller size entrain, larger particles tend to stay in *Bulk* while others adhere to the column wall. Table 4-4 outlines the size distribution of particles in different regions of the column after the fluidization period and specifies that particles smaller than 850 μm adhered to the column wall whereas particles smaller than 165 μm were elutriated.

Table 4-4. Size distribution of PE particles which was measured using a Malvern Mastersizer 2000 for different regions of the column after 1 hour of fluidization.

Region	**Particle Size (μm)**		
	d_{10}	d_{50}	d_{90}
Bulk	415±32	783±21	1525±56
Fouling-Bottom	272±16	467±29	851±43
Fines	37±5	86±12	165±25

Particles that entrain during fluidization provide valuable information about the change in polarity of particles within the bed. Fig. 4-10 depicts the cumulative net charge of elutriated particles over a 60-minute fluidization period for both concentrations. Notably, experiments at 100 ppm concentration did not alter the cumulative charge trend compared to PE experiments where no powder was present. However, a significant shift in the trend occurred when the mass loading increased to represent 1000 ppm, and this significant change will be further discussed.

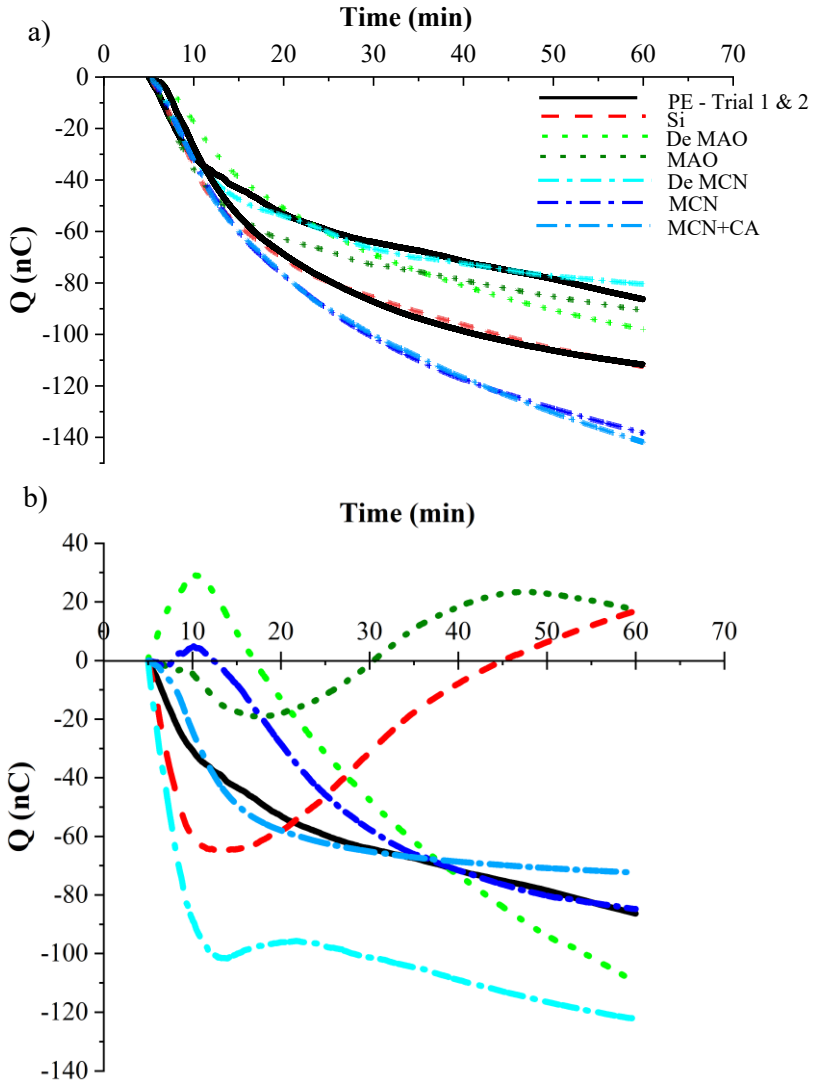

Fig. 4-10. The accumulative net charge of elutriated particles during fluidization period of 60 minutes, a) 100 ppm and b) 1000 ppm. (Please refer to the web version of this article for color interpretations in this figure).

Fig. 4-11 illustrates the fouling amount and the net specific charge of *Bulk* and *Fouling-Bottom* regions for PE fluidizations, alongside the results when 100 ppm of various powders were present in the column and the mixture was fluidized (error bars indicate one standard deviation). Following a one-hour fluidization of PE particles, on average, the amount of total fouling was approximately 22.2 g, and the net Q/m of *Bulk* and *Fouling-Bottom* were 0.41 nC/g and 106.5 nC/g, respectively. Introducing different powders into the bed, statistically, had a marginal influence on the amount of fouling and *Q/m* of *Bulk*. These results differ from the results we obtained in our previous work in which 100 ppm of CA could change the charge and fouling in

the column drastically. Therefore, these results are indicative of a different charge transfer behaviour within the PE bed in presence of these particles.

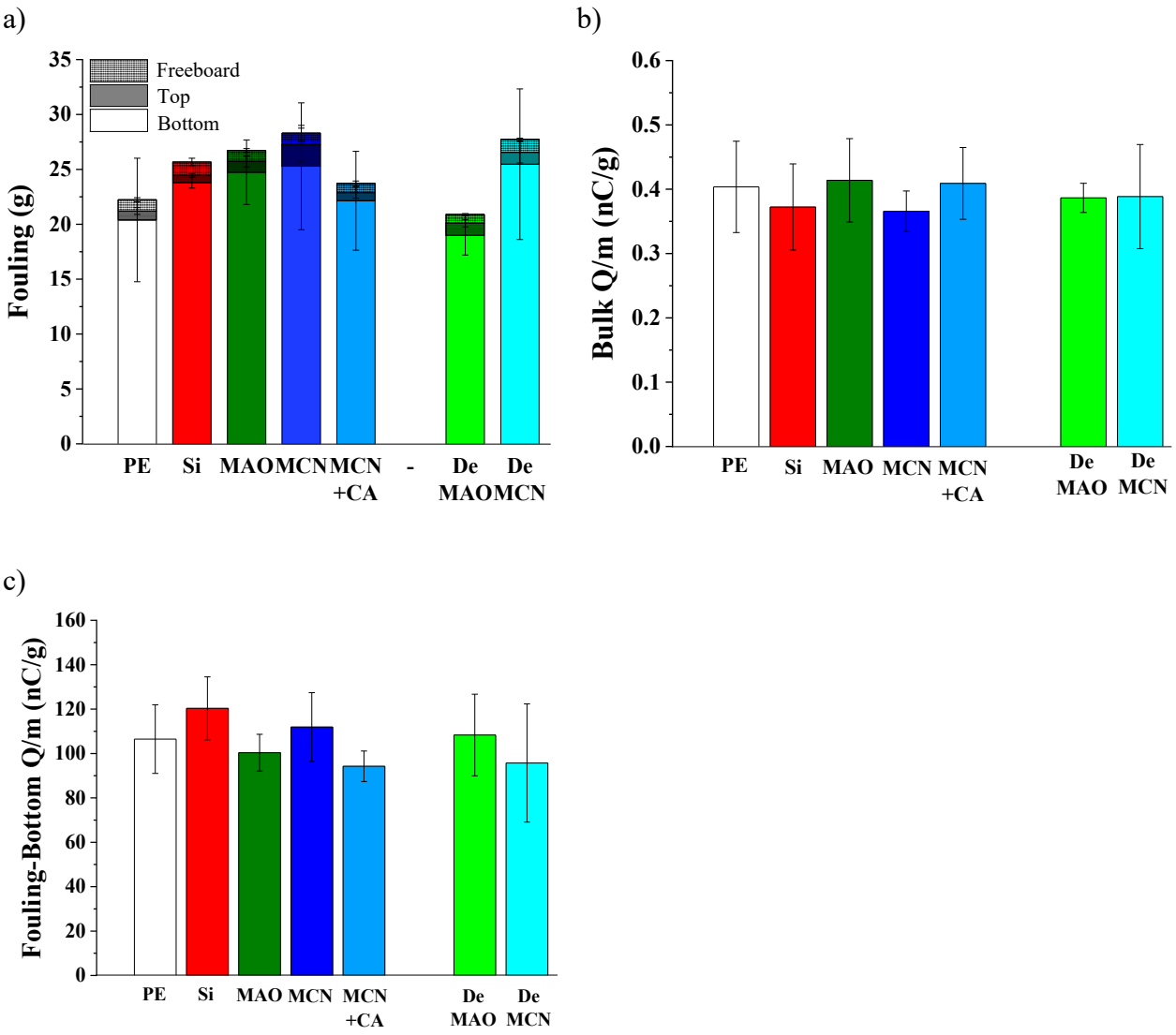

Fig. 4-11. The amount of fouling (a), the net specific charge of Bulk (b) and Fouling-Bottom (c) for 0.1 g powder injections.

Next, the impact of the powder concentration within the PE bed was evaluated, and thus, a higher mass loading of 1.0 g was tested. As illustrated in Fig. 4-12 the fouling amount and the net specific charge of particles in the *Bulk* and *Fouling-Bottom* regions experienced a substantial alteration.

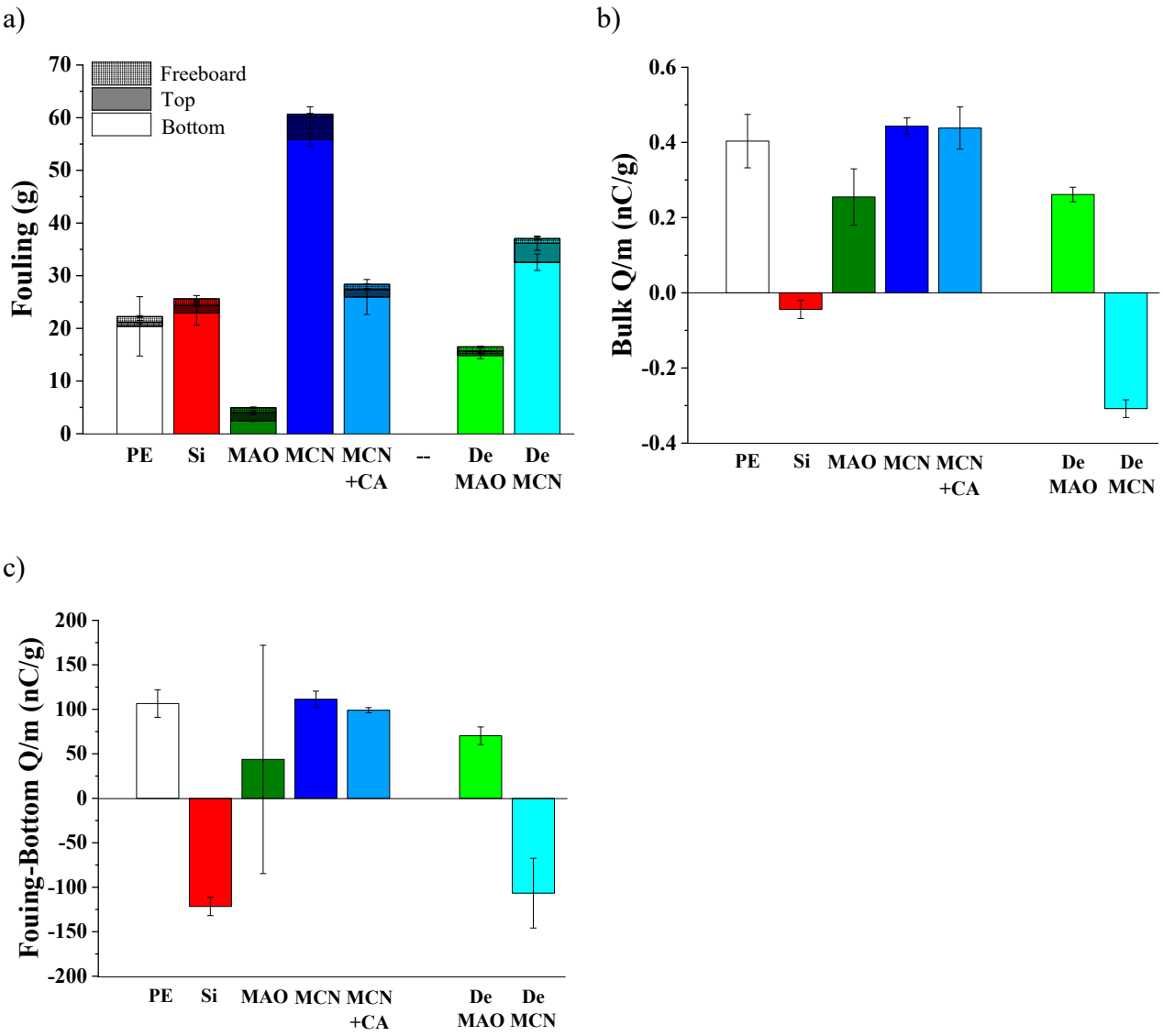

Fig. 4-12. The amount of fouling (a), the net specific charge of *Bulk* (b) and *Fouling-Bottom* (c) at 1000 ppm concentrations.

For the mixture of PE and silica, it is evident that the results for the amount of fouling were consistent in all the experiments; however, the degree of net *Q/m* experienced a significant decline, leading to a polarity shift in the bed from positive to negative. In the case of a very low net charge in the *Bulk*, particles might be composed of either low-charged particles or highly charged particles with opposing polarities. Examining the raw data while the *Bulk* particles were being collected in the bottom Faraday cage (Fig. 4-13) revealed that the bulk consisted of both positively and negatively charged particles, with a slight predominance of negatively charged particles.

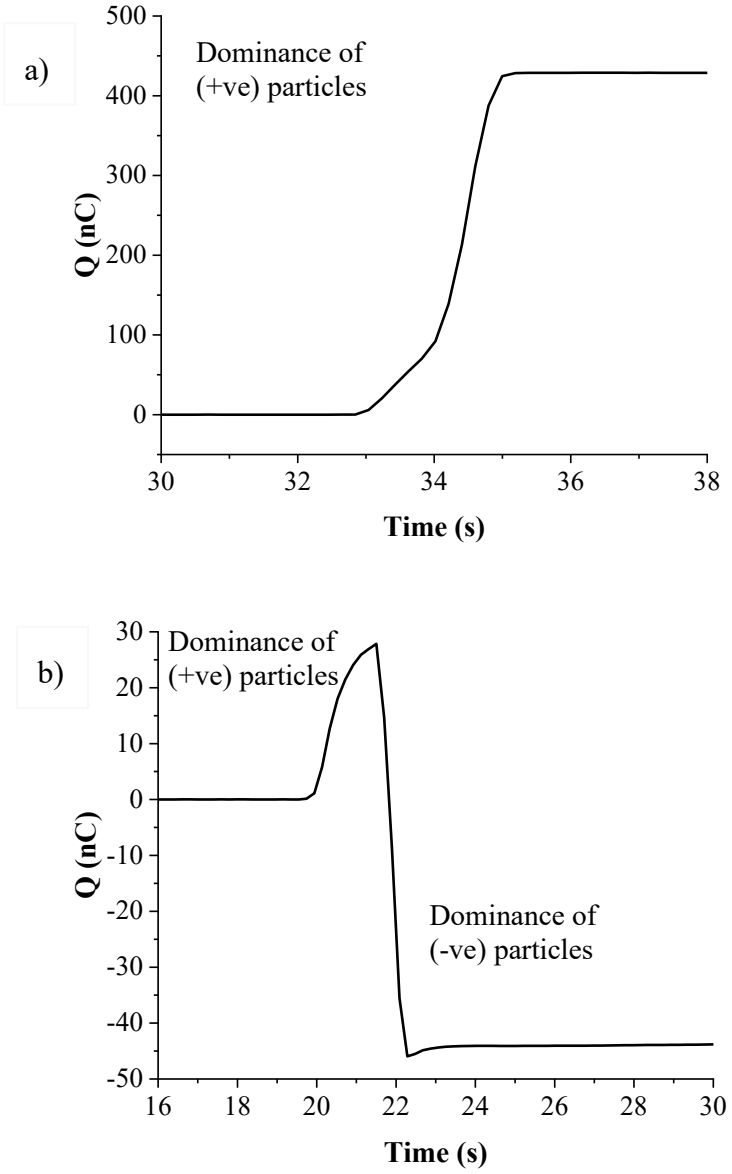

Fig. 4-13. The net charge of *Bulk* particles measured during their collection into the bottom Faraday cage when a) without the addition of Si, b) the bed contained 1 g of Si.

Consequently, the low net Q/m for *Bulk* particles is attributed to the fact that particles acquired both high positive and negative charges. This is further supported by results presented in Fig. 4-10b for the same case, where elutriated particles initially exhibited a steep increase in charge, indicating Si particles entrainment with the small PE particles. However, after 5 minutes of fluidization, the polarity of the elutriated particles (potentially from both silica and PE particles) changed from negative to positive. As depicted in Fig. 4-12c, showing *Fouling-Bottom* with a

negative polarity, the layer formation on the wall is governed by the dominant negatively charged particles. This suggests that silica acts as a negative inducer in the bed, potentially owing to its acidic nature. Building on the earlier analogy, when the *Q/m* of *Bulk* particles decreases, the induced charge on the column also diminishes. Consequently, fine Si particles are prone to adhering to the column wall in the absence of the negative charge on the column wall and promoting fouling to a similar mass as PE experiments.

Presence of MAO particles yielded a significantly lower fouling, approximately by a factor of four. This can be rationalized by the observation that small particles within the bed exhibited minimal charge. As illustrated in Fig. 4-10a, for 100 ppm concentrations, the *Q* of fine particles did not experience significant variations. However, Fig. 4-10b clearly demonstrates that elutriated fines for MAO experiments exhibited a lower magnitude of charge in comparison with 100 ppm runs or PE trials. Furthermore, the elutriated particles exhibited cumulative net charge with positive and negative polarities, indicating an alteration in the charge of small particles during the fluidization period. Zaccaria et al. [62] proposed that three Lewis acid sites on MAO could be generated in presence of ionized nitrogen or oxygen, resulting in the formation of transient $[\text{-AlMe}_2]^+$ species and MAO with a negative polarity. Since the fluidization experiments were performed using a nitrogen gas, the ionized nitrogen could be present in the bed as the result of electrostatic charge generation, and consequently, the breakdown of the gas. Considering this premise, the decline in *Q/m* of *Bulk* and the low charge generation of elutriated particles could be attributed to the presence of negatively charged MAO and its positive transient species, respectively, especially for when high concentration of MAO is present.

Unlike MAO that significantly mitigated the amount of wall fouling, presence of 1 g MCN catalyst in the PE bed led to a substantial increase in total fouling by three fold, and this increase was also observed in various regions of the bed, including the *Fouling-Bottom* and *Fouling-Top* regions, as depicted in Fig. 4-12a . On the other hand, MCN particles yielded a comparable net *Q/m* for both *Bulk* and the *Fouling-Bottom* regions to that obtained in PE alone experiments. The trend for the Q of fines also aligned with PE experiments after 10 minutes of fluidization, suggesting either a lower mass accumulation in the filter bag or a less charge generation by the particles. Fig. 4-14b shows that the mass of elutriated particles at the end of fluidization with MCN particles was minimal, being 45% less than that of PE alone experiments, although 1 g of MCN particles with d_{50} of 45 µm was added to the bed. This implies that the majority of fine

particles, originating from both PE resin and MCN catalyst, remained in the *Bulk* and eventually adhered to the column wall and promoted fouling. The adherence of fine particles to the column wall, potentially possessing a higher specific charge due to a larger surface area, ultimately increased the amount of fouling.

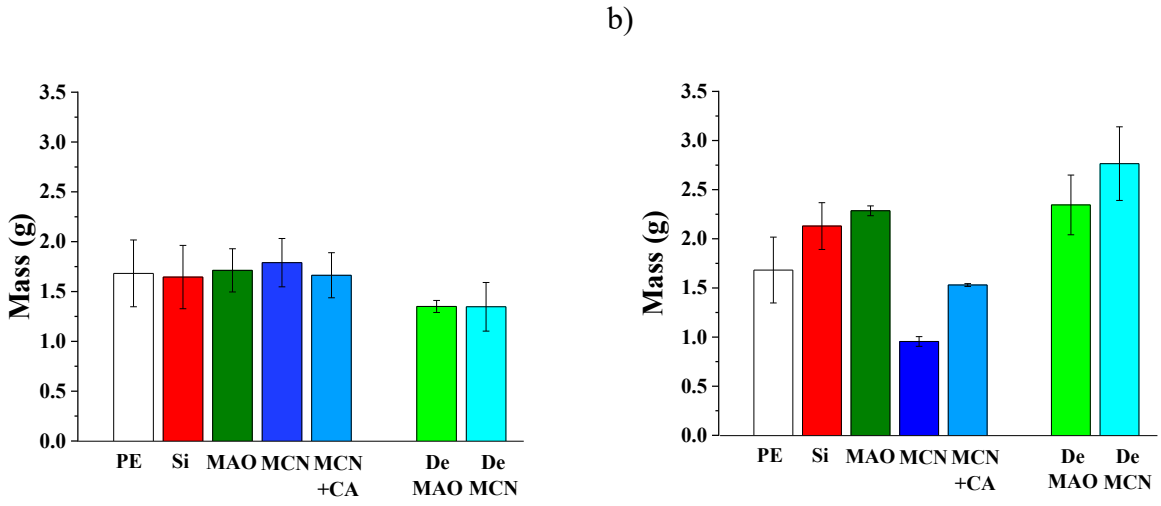

Fig. 4-14. The final mass of elutriated particles for PE and for when various powders were added to the bed, a) 100 ppm and b) 1000 ppm.

MCN in its deactivated form (De MCN) had significantly less influence on the degree of wall fouling compared to its active form. However, it still was a fouling promoter compared to when there was no powder present in the PE bed. This finding points toward an important fact that the changes to the catalyst surface chemistry would affect the charging behavior of the catalyst within the PE bed. De MCN particles acted as a negative inducer in the bed, causing a polarity reversal of the *Bulk* particles to a magnitude similar to that observed for PE particles. The elements present on the De MCN catalyst could be ZrO_2, Al_2O_3 and cyclopentadiene. The only component which possibly exhibits negative inducing behavior due to its acidic nature is the dimerized cyclopentadiene [63], as the other components are amphoteric. Evaluating the elutriated fines charging behavior infers that at the start of fluidization, there was a steep increase in the measured net charge, indicating that De MCN and fine PE particles exited the column together, given that upon entering the bed, De MCN particles displayed a negative polarity (Fig. 4-10b). After 5 minutes of fluidization, the decline in elutriated particles charge became less pronounced and aligned with the trend observed in PE alone experiments. The increase in fouling could have originated from the *Bulk's* negative polarity, resulting in the dominant

formation of the first layer by negatively charged particles. Since both De MCN and fine PE particles were negatively charged, they had a higher probability of adhering to the column wall, thereby promoting the formation of fouled layers on the wall.

Unlike MCN catalyst particles that significantly augmented the extent of wall fouling, when their mixtures with traces of CA (MCN+CA) was tested, no noticeable influence on the values and polarities of particles' net *Q/m* in *Bulk*, *Fouling-Bottom*, and *Fines* regions were observed. Moreover, there was no significant change in the charge magnitude of fouling and elutriated particles. This implies that while CA particles were effective in suppressing the effects of MCN particles, they did not alter the results in comparison to the PE alone experiments. It is important to highlight that the CAs used in the tested samples induced a positive polarity in the bed of PE particles in our prior research [53]. In the case of the MCN fluidization runs, small particles charged with a negative polarity tended to remain in the bed. The presence of these chemical additives resulted in a reduction of the charge on those particles, consequently increasing the quantity of small particles elutriated, as illustrated in Fig. 4-14, and suppressing the fouling generation on the column wall.

MAO in its deactivated form possesses aluminum oxide on its surface, which has an amphoteric characteristic. This suggests that it can act as both an acid and a base depending on the substances it interacts with. Consequently, it was anticipated that De MAO would exhibit minimal influence in the PE bed. As illustrated in Fig. 4-8, the polarity of De MAO upon entering the bed was positive. Fig. 4-10b further indicates that at the beginning of fluidization, the elutriated particles exhibited a net positive polarity, signifying that De MAO elutriated with fine PE particles. Subsequently, there was no deviation in the trend, and the net charge of fines followed the same pattern as observed in the PE alone experiments, indicating a similar behavior as the fine PE particles which generated a negative polarity in the bed. The presence of De MAO in the fluidized bed resulted in a slightly lower amount of fouling and reduced the net *Q/m* of *Bulk* particles. Given its amphoteric nature – neither acidic nor basic – the diminished charge in bulk particles could be attributed to the addition of more fine particles to the bed which tend to generate a negative polarity. Consequently, this reduction in *Bulk*'s charge led to a decline in fouling due to a weakened induced charge on the wall.

Based on the results and discussion presented in this work, it is evident that the catalyst surface chemistry could play a pivotal role in changing the net charge of the bed and its polarity, and in turn, the amount of PE resin wall fouling in a fluidized bed. Therefore, from commercial operation standpoint of view in which altering the type of catalyst could result in various *Sheeting* related issues, it is critical to have a better understanding of the role of other types of catalysts, for instant Ziegler-Natta catalyst. As discussed in section 4.1, Ziegler-Natta catalysts have different surface chemistry and consist of elements such as $MgCl_2$, $TiCl_4$, and triethylaluminium. Hence, further investigation is necessary including the testing of various types of commonly utilized catalysts in gas-phase PE processes.

4.4 Conclusion

This study delved into investigating the impact of a common type of metallocene catalyst and its various elements including the dehydrated amorphous silica catalyst base, the co-catalyst and the full catalyst on charge build up in a fluidized bed of LLDPE resin. The investigation revealed that the type of charge polarity and the degree to which these elements build electrostatic charge, both while pneumatically conveyed and fluidized along with a PE resin is certainly influenced by the particle's surface chemistry. The study specifically demonstrated that at concentrations of 100 ppm neither the catalyst support nor the cocatalyst and the catalyst actively participate in charge generation or fouling formation within the PE fluidized bed. On the other hand, when larger concentrations of these powders were present, i.e. 1000 ppm, both the active cocatalyst (MAO) and the active MCN catalyst played a vital role by mitigating and enhancing the extent of wall fouling, respectively. This is a significant finding implying that in relation to the real PE process any unforeseen variations in the concentration of the catalyst within the reactor could have an adverse effect by potentially augmenting *sheeting*. Conversely, in commercial reactors, a common sheeting mitigation approach involves the introduction of CAs or other charge control agents to reduce charge generation in the reactor. However, these methods often involve negative impacts on catalyst activity and PE properties. In this work, it was demonstrated that MAO can significantly reduce fouling by suppressing charge generation, especially for small particles. Hence, the use of MAO could potentially reduce the of CA in the reactors and benefit industry in decreasing sheeting while simultaneously increasing the activity of the catalyst.

Results of this work infer that the presence of the active MCN catalyst resulted in retaining small PE resin particles within the bed, consequently leading to a substantial increase in fouling mass. Therefore, it is recommended to alter the produced PE resin size distribution to lessen the fine particles in the reactor (i.e., particles smaller than 165 μm). This could potentially help in counter acting the negative effects due to presence of MCN catalyst particles. Furthermore, the deactivation of MCN catalysts at high concentrations in the reactor could potentially induce more negative polarity in the bulk and augment the formation of *sheets*.

In terms of the mechanisms for charge transfer present in this study, it can be concluded that non-ionic components with acidic properties such as silica and deactivated metallocene catalysts tend to induce negative polarity in the bed, aligning with the electron transfer mechanism. As for components that can possibly form ions in the bed such as methylaluminoxane and active metallocene catalysts, ion transfer becomes the dominant charge transfer mechanism.

It is important to note that the experiments in this study were conducted under atmospheric pressure and ambient temperature conditions. In a commercial PE reactor, the catalyst particles are active and participate in polymerization reactions. Additionally, during the polymerization process, the polymer grows, and the catalyst base may undergo fractures. The influence of such dynamic parameters could be a topic of interest for future studies. Furthermore, experimentally investigating the chemistry of other types of catalysts such as Ziegler-Natta will provide more information regarding the role of catalyst chemistry in electrostatic charge generation not only in fluidized beds but also in more controlled environments.

Acknowledgments

Financial support from Univation Technologies, LLC (USA) and the Natural Sciences and Engineering Research Council of Canada (NSERC) is acknowledged.

References

[1] M.G. Goode, D.M. Hasenberg, T.J. McNeil, T.E. Spriggs, Method for Reducing Sheeting During Polymerization of Alpha-Olefns, 4803251, 1989.

[2] B.D. Fulks, S.P. Sawin, C.D. Aikman, J.M. Jenkins, Process for reducing sheeting during polymerization of alpha-olefins, United States Patent, No. 4532311, (1985).

[3] G. Hendrickson, Electrostatics and gas phase fluidized bed polymerization reactor wall

sheeting, Chem. Eng. Sci. 61 (2006) 1041–1064.

[4] J.R. Chirillo, K.C. Kimbrough, P.E. McHattie, Method for Reducing Sheeting During Polymerization of Alpha-Olefns, 1989.

[5] W.R. Harper, The Volta effect as a cause of static electrification, Proc. R. Soc. London. Ser. A. Math. Phys. Sci. 205 (1951) 83–103.

[6] A.F. Diaz, J. Guay, Contact charging of organic materials: Ion vs. electron transfer, IBM J. Res. Dev. 37 (1993) 249–259.

[7] R.G. Horn, D.T. Smith, B.A. Grabbe, Present addresses: Schools of Applied Physics and Chemical Technology, South Aust. 5095 (1993) 442–443.

[8] L.H. Lee, Fundamentals of Adhesion, Plenum, New York, 1990.

[9] R.P.N. Veregin, M.N.V. McDougall, M.S. Hawkins, C. Vong, V. Skorokhod, H.P. Schreiber, A bidirectional acid-base charging model for triboelectrification: Part 1. Theory, J. Imaging Sci. Technol. 50 (2006) 282–287.

[10] R. Veregin, M. McDougall, M. Hawkins, C. Vong, V. Skorokhod, H. Schreiber, A bidirectional acid-base charging model for triboelectrification: Experimental verification by inverse gas chromatography and xerographic charging of toner and carrier, Int. Conf. Digit. Print. Technol. 50 (2008) 30–33.

[11] L.S. McCarty, G.M. Whitesides, Electrostatic charging due to separation of ions at interfaces: Contact electrification of ionic electrets, Angew. Chemie - Int. Ed. 47 (2008) 2188–2207.

[12] S. Pence, V.J. Novotny, A.F. Diaz, Effect of Surface Moisture on Contact Charge of Polymers Containing Ions, Langmuir. 10 (1994) 592–596.

[13] Y. Awakuni, J.H. Calderwood, Water vapour adsorption and surface conductivity in solids, J. Phys. D. Appl. Phys. 5 (1972) 1038–1045.

[14] W.R. Harper, Contact and Frictional Electrification, Morgan Hill, Laplacian, 1998.

[15] H.T. Baytekin, B. Baytekin, J.T. Incorvati, B.A. Grzybowski, Material transfer and polarity reversal in contact charging, Angew. Chemie - Int. Ed. 51 (2012) 4843–4847.

[16] R.K. Pandey, H. Kakehashi, H. Nakanishi, S. Soh, Correlating Material Transfer and Charge Transfer in Contact Electrification, (2018).

[17] A.E. Hamielec, J.B.P. Soares, Metallocene catalyzed polymerization: industrial technology, (1999) 446–453.

[18] R. Hoff, Handbook of Transition Metal Polymerization Catalysts, Second Edition, Wiley, 2010.

[19] Z. Liu, X. He, R. Cheng, M.S. Eisen, M. Terano, S.L. Scott, B. Liu, Chromium catalysts for ethylene polymerization and oligomerization, 1st ed., Elsevier Inc., 2014.

[20] X. Li, R. Cheng, J. Luo, Q. Dong, X. He, L. Li, Y. Yu, J. Da, B. Liu, Experimental and theoretical studies on ethylene polymerization using SiO2-supported silyl chromate type catalysts prepared by a green method, J. Mol. Catal. A Chem. 330 (2010) 56–65.

[21] S.S. Reddy, S. Sivaram, Homogeneous metallocene-methylaluminoxane catalyst systems for ethylene polymerization, Prog. Polym. Sci. 20 (1995) 309–367.

[22] Y.I. Yermakov, V.A. Zakharov, G.A. Nesterov, Catalysis by Supported Complexes, Elsevier, Amsterdam, 1981.

[23] M. Terano, K. Soga, Catalyst Design for Tailor-Made Polyolefins, Kodansha Ltd., Tokyo, 1994.

[24] I.T. Lima, R. Gargano, S. Guerini, E.N.C. Paura, A theoretical study of adsorbed non-metallic atoms on magnesium chloride monolayers, New J. Chem. 43 (2019) 7778–7783.

[25] D. V. Stukalov, V.A. Zakharov, Active site formation in $MgCl_2$-supported Ziegler-Natta catalysts: A density functional theory study, J. Phys. Chem. C. 113 (2009) 21376–21382.

[26] F. Poorsank, H. Arabi, N. Ghasemi Hamedani, Silyl diol ester as a new selectivity control agent in $MgCl_2$-supported Ziegler-Natta systems for propylene polymerization: Catalyst structure and polymer properties, RSC Adv. 9 (2019) 7420–7431.

[27] A. Piovano, M. Signorile, L. Braglia, P. Torelli, A. Martini, T. Wada, G. Takasao, T. Taniike, E. Groppo, Electronic Properties of Ti Sites in Ziegler-Natta Catalysts, ACS Catal. 11 (2021) 9949–9961.

[28] X. Guo, Z. Liu, Z. Fan, B. Liu, New Insights into the Nature of Ti (II) and Ti (III) Active

Sites in the Heterogeneous Ziegler-Natta Catalyst, J. Phys. Chem. C. 127 (2023) 5720–5730.

[29] D. V. Stukalov, I.L. Zilberberg, V.A. Zakharov, Surface species of titanium (IV) and titanium (III) in $MgCl_2$-supported Ziegler-Natta catalysts: A periodic density functional theory study, Macromolecules. 42 (2009) 8165–8171.

[30] T. Taniike, M. Terano, Reductive formation of isospecific Ti dinuclear species on a $MgCl_2$ (110) surface in heterogeneous ziegler-natta catalysts, Macromol. Rapid Commun. 29 (2008) 1472–1476.

[31] J. Wang, R. Cheng, X. He, Z. Liu, Z. Tian, B. Liu, A Novel (SiO_2 / MgO / $MgCl_2$).$TiCl_x$ Ziegler – Natta Catalyst for Ethylene and Ethylene / 1-Hexene Polymerization, Macromol. Chem. Phys. 216 (2015) 1472–1482.

[32] B. Jiang, F. He, P. Yang, Z. Zhang, Y. Weng, Z. Cheng, Z. Fu, Z. Fan, Enhancing stereoselectivity of propylene polymerization with $MgCl_2$-supported Ziegler-Natta catalysts by electron donor: Strong effects of titanium dispersion state, Catal. Commun. 121 (2019) 38–42.

[33] W. Kaminsky, A. Laban, Metallocene catalysis, Appl. Catal. A Gen. 222 (2001) 47–61.

[34] W. Kaminsky, Metallocene based polyolefin nanocomposites, Materials (Basel). 7 (2014) 1995–2013.

[35] M.E.Z. Velthoen, J.M. Boereboom, R.E. Bulo, B.M. Weckhuysen, Insights into the activation of silica-supported metallocene olefin polymerization catalysts by methylaluminoxane, Catal. Today. 334 (2019) 223–230.

[36] E. Zurek, T. Ziegler, Theoretical studies of the structure and function of MAO (methylaluminoxane), Prog. Polym. Sci. 29 (2004) 107–148.

[37] D. Zhang, H. Cai, Y. Su, W. Sun, D. Yang, G.A. Ozin, Silica samurai: Aristocrat of energy and environmental catalysis, Chem Catal. 2 (2022) 1893–1918.

[38] P.S. Shinde, P.S. Suryawanshi, K.K. Patil, V.M. Belekar, S.A. Sankpal, S.D. Delekar,

S.A. Jadhav, A brief overview of recent progress in porous silica as catalyst supports, J. Compos. Sci. 5 (2021) 1–17.

[39] X. Yu, C.T. Williams, Recent advances in the applications of mesoporous silica in heterogeneous catalysis, Catal. Sci. Technol. 12 (2022) 5765–5794.

[40] S. Yariv, H. Cross, Colloid Geochemistry of Silica, Springer Berlin Heidelberg, Berlin, 1979.

[41] R.J. Jorgensen, R. Reib, S.M. Whited, T.J. Hogan, D.G. Clark, T.M. Tambling, Process for Polymerizing Olefin-Based Polymers Containing High Molecular Weight Fractions in Condensed and Super-Condensed Mode, 2013/0137827, 2013.

[42] M.G. Goode, C.C. Williams, F.D. Hussein, T.J. McNeil, K.H. Lee, Static Control in Olefin Polymerization, 6111034, 2000.

[43] D.F. Hussein, K.J. Cann, F.G. Stakem, A.M. Schoeb-Wolters, M.D. Awe, Polymerization Process Using a Supported Constrained Geometry Catalyst, 8957167, 2015.

[44] P. Mehrani, M. Murtomaa, D.J. Lacks, an overview of advances in understanding electrostatic charge buildup in gas-solid fluidized beds, J. Electrostat. 87 (2017) 64–78.

[45] J. Guardiola, V. Rojo, G. Ramos, Influence of particle size, fluidization velocity and relative humidity on fluidized bed electrostatics, J. Electrostat. 37 (1996) 1–20.

[46] W.O. Moughrabiah, J.R. Grace, X.T. Bi, Effects of Pressure, Temperature, and Gas Velocity on Electrostatics in Gas-Solid Fluidized Beds, Ind. Eng. Chem. Res. 45 (2009) 320–325.

[47] A. Sowinski, A. Mayne, P. Mehrani, Effect of fluidizing particle size on electrostatic charge generation and reactor wall fouling in gas-solid fluidized beds, Chem. Eng. Sci. 71 (2012) 552–563.

[48] W.O. Moughrabiah, J.R. Grace, T.B. Xiaotao, Electrostatics in gas-solid fluidized beds for different particle properties, Chem. Eng. Sci. 75 (2012) 198–208.

[49] F. Fotovat, T.A. Alsmari, J.R. Grace, X.T. Bi, The relationship between fluidized bed electrostatics and entrainment, Powder Technol. 316 (2017) 157–165.

[50] T.A. Alsmari, J.R. Grace, X.T. Bi, Effects of superficial gas velocity and temperature on

entrainment and electrostatics in gas-solid fluidized beds, Chem. Eng. Sci. 123 (2015) 49–56.

[51] M.I. Nimvari, A. Sowinski, P. Mehrani, Effect of temperature on triboelectrifcation of polyethylene particles in a pilot-scale pressurized gas-solid fluidized bed, Powder Technol. 405 (2022) 117524

[52] A. Sowinski, P. Mehrani, Impact of addition of a catalyst or its support on reactor wall coating due to electrostatic charging during fluidization of polyethylene, Ind. Eng. Chem. Res. 54 (2015) 3981–3988.

[53] M. Taghavivand, A. Sowinski, P. Mehrani, Triboelectric effects of continuity additives and a silica catalyst support on polyethylene fluidized bed wall fouling, Chem. Eng. Sci. 245 (2021) 116882.

[54] A. Sowinski, F. Salama, P. Mehrani, New technique for electrostatic charge measurement in gas-solid fluidized beds, J. Electrostat. 67 (2009) 568–573.

[55] A. Sowinski, (2010), The Study of Particle Agglomeration and Fouling in Gas-Solid Fluidized Beds Caused by Electrostatic Charge Generation [PhD Thesis], University of Ottawa.

[56] M. Taghavivand, B.J. Cho, P. Mehrani, A. Sowinski, Electrostatic charging behaviour of a silica powder during pulse pneumatic conveying, Powder Technol. 366 (2020) 119–129.

[57] M.I. Nimvari, M. Taghavivand, K. Choi, A. Sowinski, P. Mehrani, Velocity measurement of pneumatically conveyed particles via a simple current signal technique and the influence of electrostatic charge, Powder Technol. 413 (2023) 118018.

[58] A.N. Guerreiro, I.B. Costa, A.B. Vale, M.H. Braga, Distinctive Electric Properties of Group 14 Oxides: SiO2, SiO, and SnO2, Int. J. Mol. Sci. 24 (2023).

[59] D. Song, P. Mehrani, Mechanism of particle build-up on gas-solid fluidization column wall due to electrostatic charge generation, Powder Technol. 316 (2017) 166–170.

[60] M.O. Onizhuk, A. V. Panteleimonov, Y. V. Kholin, V. V. Ivanov, Dissociation Constants

of Silanol Groups of Silic Acids: Quantum Chemical Estimations, J. Struct. Chem. 59 (2018) 261–271.

[61] B.-H. Mao, E. Crumlin, E.C. Tyo, M.J. Pellin, S. Vajda, Y. Li, S.-D. Wang, Z. Liu, In situ study of the electronic structure of atomic layer deposited oxide ultrathin films upon oxygen adsorption using ambient pressure XPS, AIChE Annu. Meet. Conf. Proc. (2019) 1–3.

[62] F. Zaccaria, P.H.M. Budzelaar, R. Cipullo, C. Zuccaccia, A. Macchioni, V. Busico, C. Ehm, Reactivity Trends of Lewis Acidic Sites in Methylaluminoxane and Some of Its Modifications, Inorg. Chem. 59 (2020) 5751–5759.

[63] M. Hurtado, O. Mó, M. Yáñez, J.C. Guillemin, Acidity enhancement of the cyclopentadiene ring by PH_2 and AsH_2 substitution, Croat. Chem. Acta. 82 (2009) 1–6.

Chapter 5 – Velocity measurement of pneumatically conveyed particles via a simple current signal technique and the influence of electrostatic charge

Abstract

Particle velocity in pulse feeding pneumatic conveying was measured utilizing current signal analysis and video imaging. Glass beads and silica particles were conveyed in a conductive tube (ID of 4.57×10^{-3} m) at gas velocities of 7, 15, and 30 m/s. To measure particle velocity, an electrical current signal method was used with a new approach that uses raw current data and eliminates signal conditioning and cross-correlation analysis. This technique was successful, and results were comparable to video imaging results. The conveyed particles' charge was measured to determine its influence on particle velocity. 30 m/s gas velocity resulted in a turbulent flow and greater charge generation causing more deviations between particle and gas velocity due to the enhancement of particles' radial motion. Finally, the comparison of results with predictions of existing models revealed that further research is necessary to better understand the effect of particles' motion and charge on their conveying velocity.

5.1 Introduction

In pneumatic conveying systems, solids are transported by means of a gas through pipes. One important parameter to consider when designing a pneumatic conveying system is particle velocity by which other parameters such as friction factor, saltation velocity and the pressure drop across the conveying line can be calculated [1,2]. Therefore, knowledge of particle velocity is of great importance such that several studies have been conducted throughout the years to measure particle velocity under different pneumatic conveying operating conditions, resulting in developing numerous empirical and semi-empirical correlations which are summarized in Table 1 [3–10].

To measure the pneumatically conveyed solids' velocity, various techniques have been employed including optical probes, capacitive sensors, acoustic sensors, magnetic sensors, microwave sensors, restrictive flow sensors (e.g., Coriolis or Venturi), high-speed imaging, thermal method, Doppler method, and electrostatic method [11–20]. Among the aforementioned techniques, usage of electrostatic method is considered as a promising way to determine particle velocity in dilute systems due to its simple structure and being cost-effective [21]. This technique typically includes two sensors which are located close to each other, upstream and downstream of a pipe line, and measure the electrostatic signals induced by the conveyed charged particles [18–20]. The measured signals are then transformed, filtered, and amplified by using a signal conditioning circuit. To measure particle velocity, the cross-correlation function of the signals is plotted, and the maximum peak in the cross-correlation function corresponds to the residence time of particles between the two electrodes which in turn is converted to particle velocity [20]. The accuracy of the particle velocity measured by this method could be influenced by the distance selection and calibration of the two probes, and ill-defined peaks [21]. Besides the particle velocity measurement, other works including that of Masuda et al. [22] have utilized electrostatic technique to measure mass flow rate of particles in a continuous flow. They measured current from two conductive tubes containing a continuous flow of particles and found a relationship between the measured current and particles mass flow rate. However, their method depended on the type of powder used and required some parameters to be calculated experimentally for each type of the powder in advance.

When solids are pneumatically conveyed, they could acquire electrostatic charge due to particle-particle and particle-conveying tube wall collisions. In the case of a conveying tube made of a conductive material, the electrostatically charged particles induce a charge on the tube wall that can then be directly measured from the conductive tube in the form of a current signal. Matsusaka et al. [23] investigated the current signals from pulse injection of powders in a 6×10^{-3} m conveying tube. They discussed the peaks in the current signal and measured the charge of particles in the form of clouds. It was discussed that when particles enter or exit a conductive tube, they induce their image charge on the conductive wall. Therefore, the initial charge of the particles as they enter and the transferred charge of particles as they exit were determined. They also showed that the intensity of the current signal decreases as the pipe length increases due to less concentrated particle clouds. To improve the application of the electrostatic technique to measure particle velocity in pulse-injection pneumatic conveying of solids, in this work we have proposed a new approach. The new methodology eliminates the usage of signal conditioning circuit and cross-correlation function, and in turn calculates the residence time of particles using the peaks in the current signals directly measured from the conductive conveying pipe as the solids enter and exit the conveying line. Therefore, the first objective of this work was to implement this new proposed method to measure particle velocity in a pulse-injection pneumatic conveying system. In addition, the results were compared with the video imaging technique.

In determining the conveyed solids' velocity, drag and gravity are the two important forces that are affecting the particle's movement and as such, have been considered in all proposed models for particle velocity estimation. Another force which has not gained as much attention as the gravity and drag forces is the electrostatic force. During pneumatic transportation, particles experience numerous collisions with each other and with the wall of the conveying pipe resulting in generation and buildup of electrostatic charge on the surface of the particles, and thus generation of an electric field around each particle. Results from our previous studies [24–26] show that when particles are pneumatically conveyed in a conductive tube, they can acquire positive or negative electrostatic charge, and the magnitude of the generated charge is related to the solids surface chemistry, conveying gas velocity, and mass loading of the particles. Most significantly, we observed that the particles with high electrostatic charge would foul inside the conveying line and their electrostatic charge was larger than that of the particles leaving the conveying line [24]. This clearly indicates that the generated electric field could redirect the

conveyed particles towards the tube wall and cause fouling. In other works [27–30], it was observed that presence of a high electric field could affect the particles flow by forming a ring flow, in which particles tend to travel closer to the tube wall, or even in some cases form a back flow of particles. To the authors' knowledge, none of the experimental and modeling works reported in the open literature on conveyed particle velocity have considered the influence of the conveyed solids contact electrification. Therefore, the second objective of this work was to study the possible influence of electrostatic charge on particle velocity in the presence of electric field generated due to contact electrification of particles during pneumatic transportation. To achieve this goal, pulse injections of different solids through a conductive tube were performed at various operating conditions (i.e., conveying gas velocity and conveying tube length), and the electrostatic charge and velocity of the particles were measured and compared. Also, the measured particle velocity in the presence of electric field was compared with the particle velocities calculated by the existing models summarized in Table 5-1.

It is worth nothing that all the experiments carried out in this work were in relation to the polyethylene gas-phase production, where the catalyst particles are pneumatically fed into the reactor via pulse injection. The catalyst conveying lines are narrow stainless-steel tubes and the injection conveying gas velocity is approximately 15 m/s. It is important to indicate that no experimental work is previously reported to measure particle velocity in such a narrow conveying system, as well as the measurement of the extent particles electrostatic charging.

Table 5-1. Summary of particle velocity correlations.

Authors	**Tube Properties D (mm) & L (m)**	**Conveying Gas Velocity (m/s)**	**Particles d_p (μm) & ρ_p (kg/m^3)**	**Particle Velocity (m/s)**	**Equation**	**Note**
Belden and Kassel (1949), [3]	12<D<1.023 L=13.5	4<U_g<16.5	963<d_p<1941 860<ρ_p<976	0.765<U_p<13	$U_p = U_g - u_t$	Vertical pipe
Hinkle (1953), [4]	51<D<76	21.6<U_g<36.6	1679<d_p<8382 1048<ρ_p<1808	3< U_p <24	$U_p = U_g\left(1 - 1.41 d_p^{0.3} SG_p^{0.5}\right)$	Dilute phase
IGT (1978) [5]	-	-	-	-	$U_p = U_g\ (1 - 0.68 d_p^{0.92} \rho_p^{0.5} \rho_g^{-0.2} D^{-0.54})$	-
Kmiec and Leschonski (1984), [6]	26.6<D<50.4	3< U_g <19	67<d_p<900 2395<ρ_p<5004	3 < U_p < 17	$U_p = \left(U_g - u_t^{0.71}\right) D^{0.019}$	Vertical pipe, dilute phase
Matsumoto et al. (1986) [7]	D=20 L=5.6	5< U_g <20	210<d_p<2930 2500<ρ_p<8700	2 < U_p < 13	$U_p = U_g - 0.71 u_t \left(1 + \frac{0.0065 Fr^{2.5}}{Fr_t^{1.25}}\right)^{0.5}$	Vertical pipe, dilute phase
Klinzing et al. (1989), [8]	25.4<D<50.8	7< U_g <24	67<d_p<900 2395<ρ_p<5004	3 < U_p <15	$U_p = \left(g.d_p\right)^{0.5} (Fr - Fr_t^{0.87}) \times (1 - 0.5 sin\theta)^{0.0765} \left(\frac{D}{d_p}\right)^{0.031} \left(\frac{\rho_p}{\rho_g}\right)^{-0.0321}$	Dilute phase
Hong and Shen (1994), [9]	-	2.4< U_g <10	Fine powder	-	$U_p = U_g \left(1 - 0.533 \left(\frac{1000\rho_g}{\rho_p}\right)^{1.093} \times \left(\frac{d_p}{100} D\right)^{-0.721}\right)$	High solid/gas mass ratios (10-72)
Santo et al. (2018), [10]	26.6<D<76.2 L=55	12< U_g <28	100<d_p<4000 8.4<ρ_p<5800	10< U_p <23	$\frac{U_p}{U_g} = 1 - 0.02 \left[Ar \frac{(\rho_p - \rho_g)}{\rho_g} \left(\frac{D}{D_{50}}\right)^{-2}\right]^{0.14}$	Dilute phase

5.2 Materials and methods

Fig. 5-1 illustrates the schematic of the pneumatic conveying apparatus and the techniques utilized to measure particles' electrostatic charge and velocity. This apparatus was composed of three sections: particle loading and pneumatic conveying line, particle velocity measurement, and electrostatic charge measurement. The conveying system included a drier to reduce the conveying gas relative humidity to <1%, a pressure regulator to provide a consistent pressure, a mass flow controller (MFC) to adjust the flow rate of the conveying gas, two solenoid valves for injection of particles, a feeder to load the particles, and a stainless-steel tube. The particle velocity measurement section had a transparent glass tube and a camera at the end of the conveying line to visualize particles' movement, and one electrometer connected to the tube to measure electrical current signals. Finally, particles were captured in a cyclone-type Faraday cup for their charge measurement.

A straight horizontal stainless-steel 316 tube 4.57×10^{-3} m (¼ inch) in inner diameter, electrically isolated from the system at its inlet and outlet, was used as the conveying line. The material and diameter of the conveying line are typical of those used for catalyst conveying in polyethylene gas-phase production process. The conveying tube length (L) was varied from 2 to 3 m. Per injection, particles at 0.1 g mass loading (m_L) were loaded into a stainless-steel 316 (SS) branch tee that was used to provide an inlet for particles into the conveying line. The injection of particles was enabled by two solenoid valves operating simultaneously and controlled by LabVIEW; one normally open (NO) and one normally closed (NC). Before each injection, the conveying gas was allowed to pass through the NO valve to reach the desired gas velocity. Meanwhile, particles were loaded into the feeder. At the time of injection, NC and NO valves were switched simultaneously, allowing the gas to enter the conveying line and carry the particles. It must be noted that when the gas direction was switched to the NC valve, a pressure fluctuation occurred causing a change in the gas flow rate set by the MFC. Therefore, the average gas velocities reported in this manuscript have a variation of ±1 m/s. Air at ambient temperature (22 ± 1˚C) and relative humidity of 0.5±0.5 was used as the conveying gas at velocities (U_g) set at 7±1, 15±1 and 30±1 m/s by a mass flow controller (MKS Model 1559). The conveying gas was stopped after 40 s which was sufficient for all the particles to exit the conveying tube.

To enable visualizing the particles flow pattern and dynamics, a 40×10^{-3} m long glass tube with an inner diameter similar to that of the conveying tube was connected to the exit of the conveying line. A camera (capable of recording a video at the speed of 1000 frame per second) was placed across the glass tube to record the particles' flow. Particles were then captured in a cyclone-type Faraday cage placed at the exit of the glass tube. Two Keithley 6514 digital electrometers (E_1 and E_2 shown in Fig. 5-1) were used to measure the particles' electrostatic charge, Q (C), after pneumatic injection. E_1 was connected directly to the conveying tube to capture the electric current signal from the conveying line generated due to particles' flow. The details of such measurement can be found in our earlier work [26]. E_2 was connected to the cyclone-type Faraday cage to directly measure the particles' cumulative net charge upon exiting the conveying line.

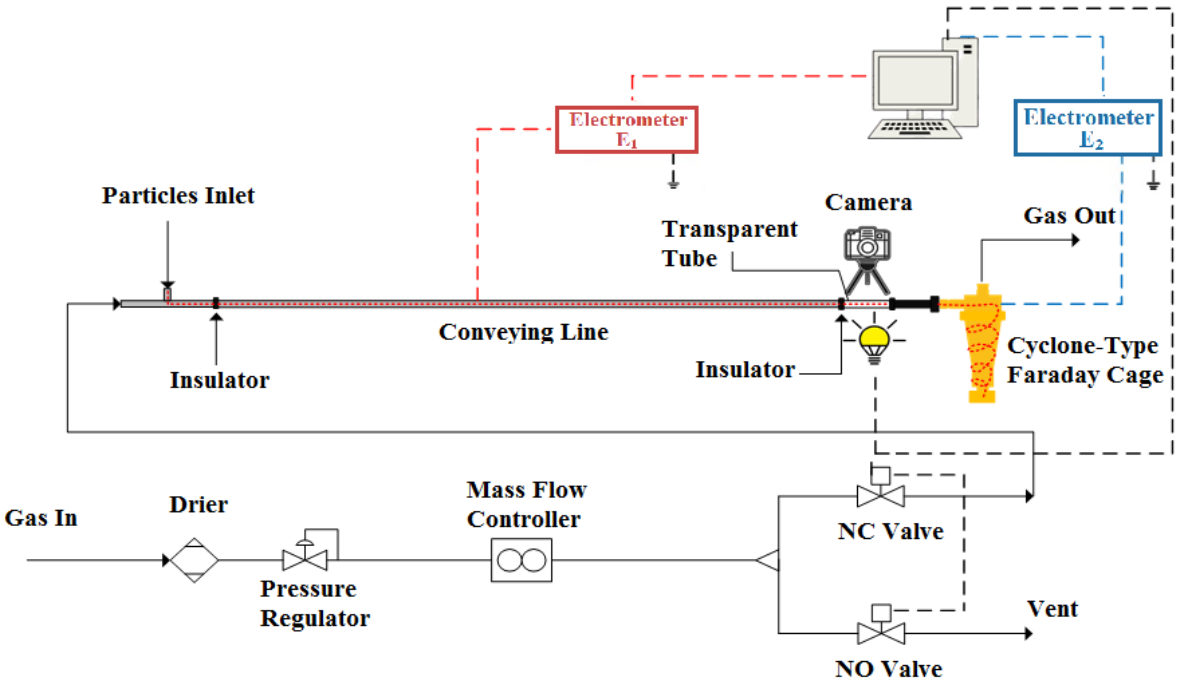

Fig. 5-1. Schematic of the pneumatic conveying apparatus with the electrostatic charge and two particle velocity measurement techniques.

The conveyed particles were glass beads, and non-dehydrated and dehydrated amorphous silica with properties shown in Table 5-2. The appearance of both particle samples as well as their Scanning Electron Microscopy (SEM) images are shown in Fig. 5-2, and the Fourier Transform Infrared (FT-IR) spectroscopy of the particles is illustrated in Fig. 5-3Fig. 5-3 FT-IR spectroscopy of the tested samples.. Glass beads were purchased from Potters Industries (USA)

whereas the amorphous silica was a typical catalyst support used in polyethylene production process and provided by the industry. Amorphous silica particles were dehydrated at 600°C using argon in a tubular furnace. Depending on the extent of the conveying tube fouling as well as the accuracy of the results, tests were conducted in sets of 5 or 10 consecutive injections and each set (i.e., operating condition) was repeated for a minimum of two times.

Table 5-2. Properties of particles.

Properties	**Glass Beads**	**Non-dehydrated Amorphous Silica**	**Dehydrated Amorphous Silica**
Density (kg/m^3)	2500	2200	2200
Skeletal density (kg/m^3)	2500	770	770
Mean particle diameter (d_{50}, μm)	68	54	54
Initial Charge (nC/g)	-0.09±0.05	-0.15±0.05	-2.2±0.1

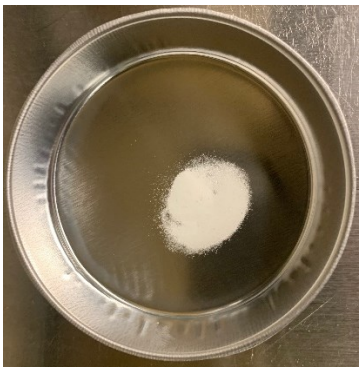

(a)

(b)

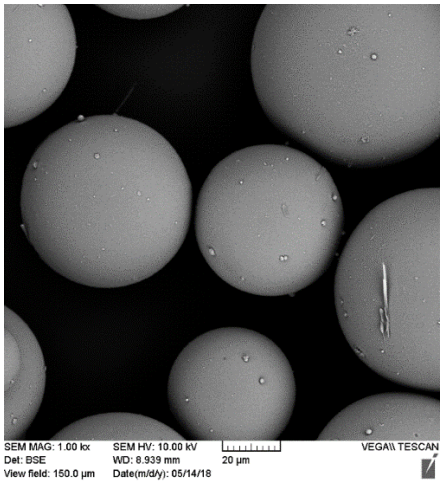

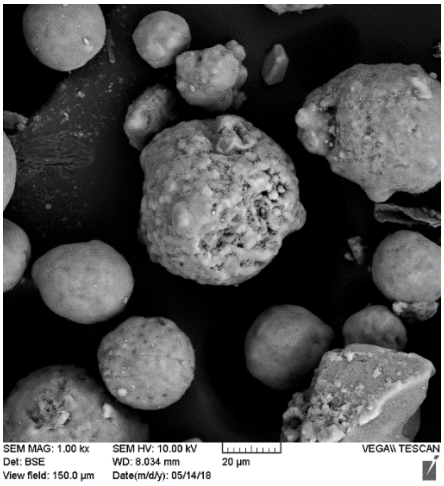

(c) (d)

Fig. 5-2. Images of the tested samples: (a) 0.1 g of glass beads, (b) 0.1 g of amorphous silica, (c) SEM of glass beads with 1000x magnification, (d) SEM of amorphous silica with 1000x magnification.

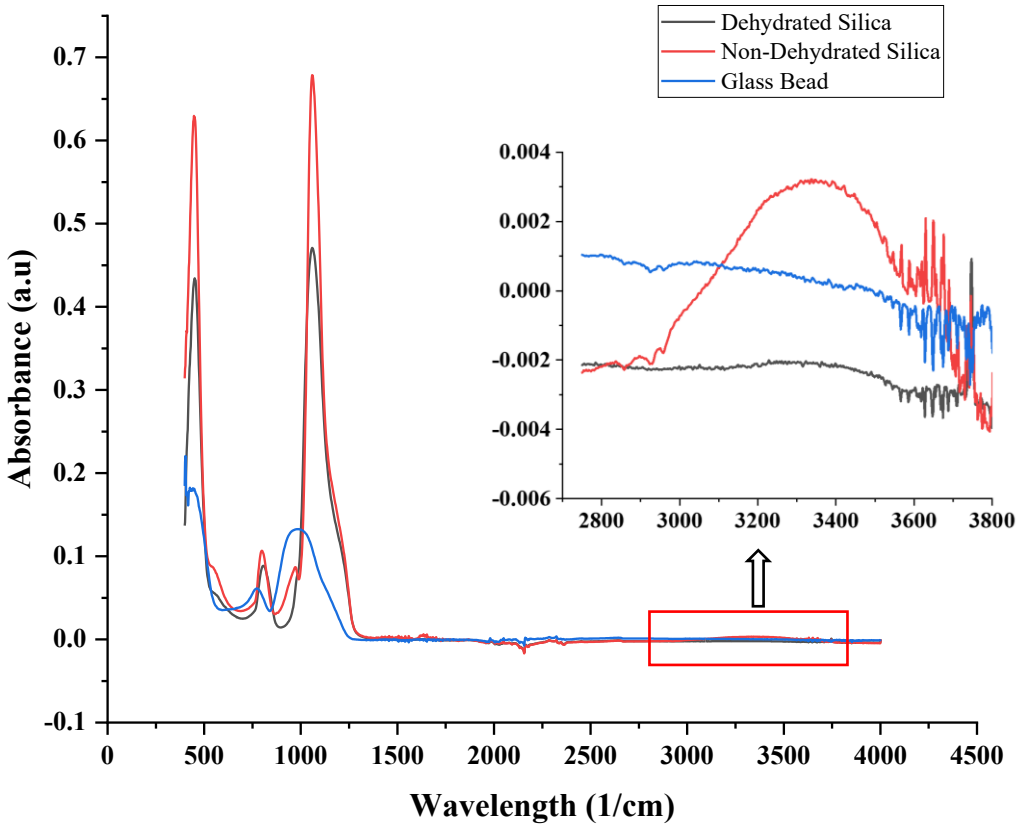

Fig. 5-3 FT-IR spectroscopy of the tested samples.

5.3 Particle velocity measurement techniques

Two different techniques were employed to measure the particle velocity during pneumatic conveying: current signal analysis and video imaging.

5.3.1 Current Signal Analysis

Fig. 5-4 shows a typical electric current signal recorded by E_1 from the conveying tube. The first peak in the current signal occurs when particles enter the SS conveying tube and induce their charge to the tube wall which is then measured by E_1. The time at which the first peak occurs is referred to as t_{in}. While inside the conveying tube particles build up electrostatic charge; however, the net charge of the tube wall and particles is zero, and thus, the current signal remains at its baseline of approximately 0 nA. However, when particles exit the conveying tube, they

leave behind a charged tube with an opposite charge polarity (e.g., in case of negative polarity charge buildup on the particles, the SS tube will be positively charged). This charge is then measured by E_1 and corresponds to the second peak in the current signal. The corresponding time to the second peak is referred to as t_{out}. The time difference between the two peaks corresponds to the particles' residence time, t_r (s), within the conveying tube. Knowing the conveying tube length, L (m), and the particles residence time, t_r (s), the particle velocity, U_p (m/s), is found using the following equation:

$$U_p = \frac{L}{t_r} \qquad \text{Eq. (5-1)}$$

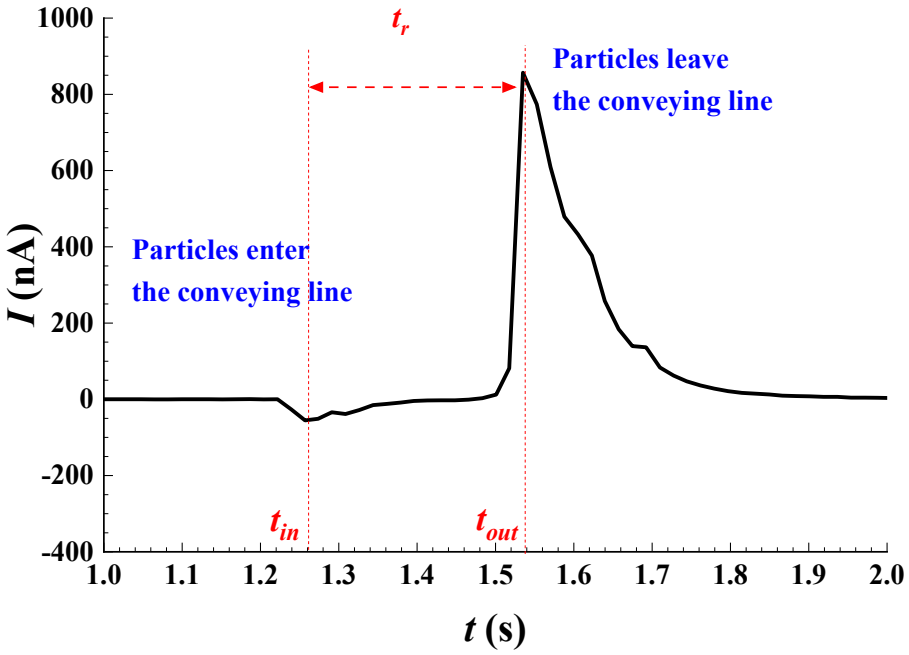

Fig. 5-4. A typical electric current signal recorded by E_1 (glass beads, L = 3 m, and U_g = 15 m/s).

5.3.2 Video Imaging

The video imaging technique utilized a camera, an LED light and two solenoid valves (NO and NC) as shown in Fig. 5-1. At the time of injection, the LED light located in front of the camera was turned on while the NC and NO valves switched simultaneously. The time at which the LED light turned on corresponds to the time that particles start to move in the feeder by the gas flow

and was referred to as t_0. It must be noted that for all the tested conditions there was a time difference between when particles started to move in the feeder (t_0) and when they entered the conveying tube (t_{in}). t_{in} was measured for all the operating conditions by placing the glass tube right after the feeder at the entrance of the conveying tube. In the transparent tube, particles were observed in dilute and dense phases as shown in Fig. 5-5. t_{in} was considered as the time of visualizing the head of the conveyed particles' plume (first dense body). Then, to measure the time that particles leave the conveying tube (t_{out}), the transparent glass tube was located at the end of the conveying tube. By knowing t_{in} and t_{out}, U_p was calculated using Eq. (5-1). It must be mentioned that the calculated particle velocity using this technique in this work corresponds to the plume head velocity and does not represent the average particle velocity.

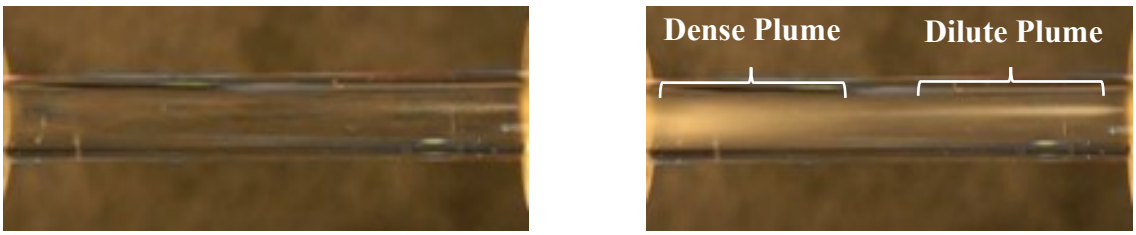

(a) (b)

Fig. 5-5. An example of a silica particles observed in the transparent tube: (a) before injection when the transparent glass tube is clear, (b) upon injection and when the dilute and dense plumes appear.

5.3.3 Comparing the two velocity measurement techniques

As mentioned in section 5.3.2, the velocity calculated by the video imaging technique represents the plume head velocity, whereas the velocity measured by the current signal analysis represents the velocity of a part of the plume which has a high concentration of charged particles. In the current signal analysis technique, the time at which the t_{out} occurs depends very much on the type of conveyed particles. In fact, t_{out} is the most important parameter that significantly influences the calculated particle velocity. Therefore, comparing the velocities obtained from the two techniques should be carried out carefully. An example of a case where Dilute Head and Dense Plume were detected, is shown in Fig. 5-5. To resolve this, the electric current signals were carefully analyzed, and four distinguishable types of signals were detected which are shown in Fig. 5-6. Comparing the obtained electric current signals with their corresponding videos, revealed a pattern by which the particles velocity could be calculated with a minimum discrepancy between the two techniques. As seen in Fig. 5-5, the video imaging analysis

disclosed that all the conveyed particles travel in a plume shape consisting of two segments of a less concentrated (referred to as dilute) head followed by a more concentrated (referred to as dense) body that also contains a high concentration of electrostatically charged particles. The transition time from the head to the body was observed to vary by the particles type. The transition time for the glass beads was calculated to be approximately 2 ms, whereas that for the non-dehydrated and dehydrated silica was between 10 to 20 ms.

- *Signal Type-I*: The small transition time for the glass beads would result in an overlap between the plume head and body and in turn a current signal with a sharp ascending slope as shown in Fig. 5-6a. As such, the glass beads moved in a dense plume followed by a dilute tail (referred to as *dense + dilute*) within the conveying tube.

The observed plume behaviour for the non-dehydrated and dehydrated amorphous silica were different from that of glass beads. Two distinguishable patterns were identified which are listed below:

- *Signal Type-II (dilute + dense + dilute + continuous dense + dilute)*: As the name suggests, in this case, the particles moved in segregated dense plumes with each dense phase resulting in a peak in the current signal (Fig. 5-6b). Since the image analysis utilized in this work only considered the first dense plume, then the t_{out} from the current signal must be adjusted to correspond the first dense plume. The adjusted t_{out} (referred to as $t_{out\text{-}adj}$) can then be used for particles velocity calculations.
- *Signal Type-III & IV (dilute + continuous dense + dilute)*: In this category, no segregated plumes formed, and particles moved in a dilute phase followed by a continuous dense phase. As such, the peak of the electric current signal would tend to be either flat or parabolic. For the cases where the peak is flat (Fig. 5-6c), the $t_{out\text{-}adj}$ is the time at which the ascending current signal slope became almost zero. This case happens when a big portion of particles in the dense plume have the same amount of charge and no change occurs in the particles' current over time (i.e., $dI/dt = 0$ or $dQ/dt = constant$). However, there were cases where the peak of the current signal was parabolic, making it impossible to locate the $t_{out\text{-}adj}$ (Fig. 5-6d). This is the case where some discrepancies can be observed between the two velocity measurement techniques.

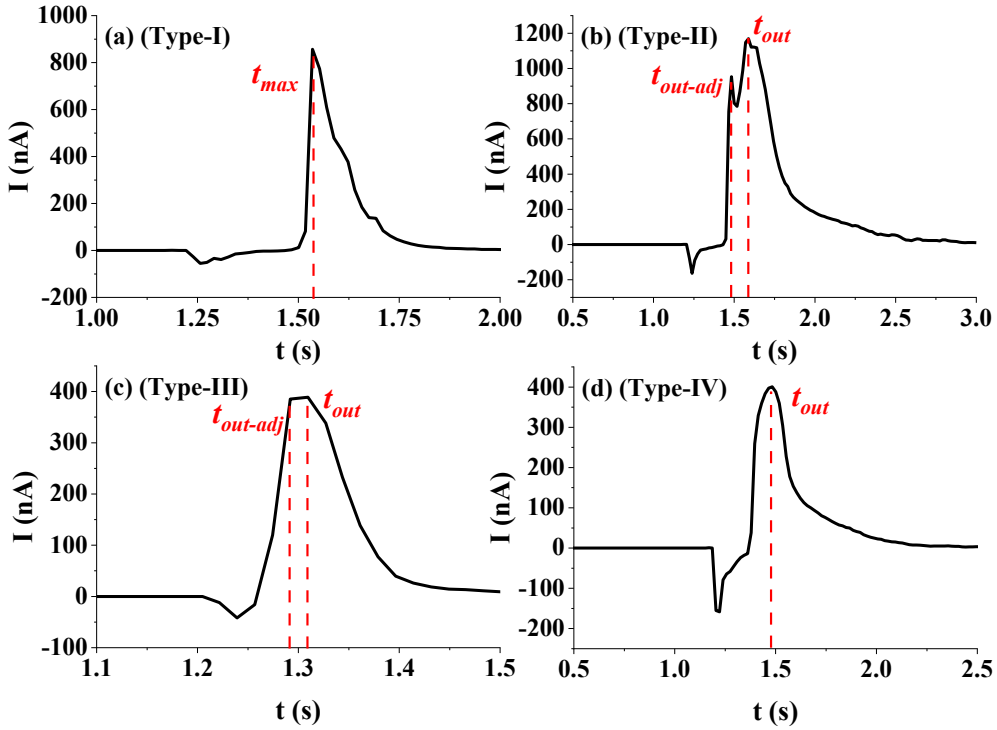

Fig. 5-6. Various types of electric current signals captured from the pneumatic conveying line. (a) *signal Type-I* (glass beads, L = 3 m, U_g = 30 m/s); (b) *signal Type-II* (non-dehydrated silica, L = 3 m, U_g = 15 m/s); (c) *signal Type-III* (non-dehydrated silica, L = 3 m, U_g = 7 m/s); (d) *signal Type-IV* (dehydrated silica, L = 2 m, U_g = 7 m/s).

5.4 Results and Discussion

5.4.1 Electrostatic charge generation

As shown in Fig. 5-7, all samples acquired a negative net charge polarity after contacting the stainless-steel conveying tube which was expected and in agreement with the triboelectric series [31,32]. For all the operating conditions tested, all three types of particles became significantly charged in comparison to their charge prior to conveying (initial charges are presented in Table 5-2). At the same operating conditions, in comparison to glass beads, amorphous silica particles gained a larger electrostatic charge at high gas velocities. This was expected to be due to their lower bulk density, resulting in a significantly larger number of particles for the same sample mass loading, which is also evident from Fig. 5-2. Therefore, a larger number of contacts with the conveying tube was expected for the amorphous silica particles, which subsequently resulted in a higher degree of charge generation.

Between the two amorphous silica particles, dehydrated particles obtained a larger electrostatic charge. As presented in our earlier work [26], dehydration removes physically adsorbed moisture and silanol groups from the surface of silica particles which is evident from FT-IR results shown in Fig. 5-3 where a small O-H stretching was observed between 3200-3650 cm^{-1} spectra for non-dehydrated silica. Thus, it is expected that the surface electrostatic charging to be augmented for the dehydrated particles.

Results from Fig. 5-7 also clearly indicate that increasing the tube length and conveying gas velocity resulted in more charge generation for all three particles. In a conveying tube, before reaching saturation charge, the charge transfer between particles and the tube wall depends on many parameters including the types of materials (i.e., gas, tube, and particles) which are in contact, particles size and surface morphology, conveying gas velocity and conditions (e.g., temperature and humidity), and tube length (i.e., number of contacts) [26,33–35]. The conveying gas and its conditions, as well as the tube material were similar for all the particle types tested in this work. Hence, it is concluded that the variations in the *Q/m* gained by the particles depended on the conveying gas velocity, and the number and extent of the collisions present. Another parameter that could result in a greater number of contacts, other than the tube length, is the trajectory of particles during transportation. It should be noted that the *Re* number of the gas at 7, 15 and 30 m/s were 2132, 4570 and 9140, respectively. Thus, the conveying gas flow regime at 7 m/s was close to laminar, at 15 m/s close to transient, and at 30 m/s was turbulent [36]. In a turbulent flow regime, the velocity of the fluid undergoes a continuous change in magnitude and direction. Therefore, at this condition the conveyed particles would have a greater chance to collide with the tube wall and in turn acquire more electrostatic charge.

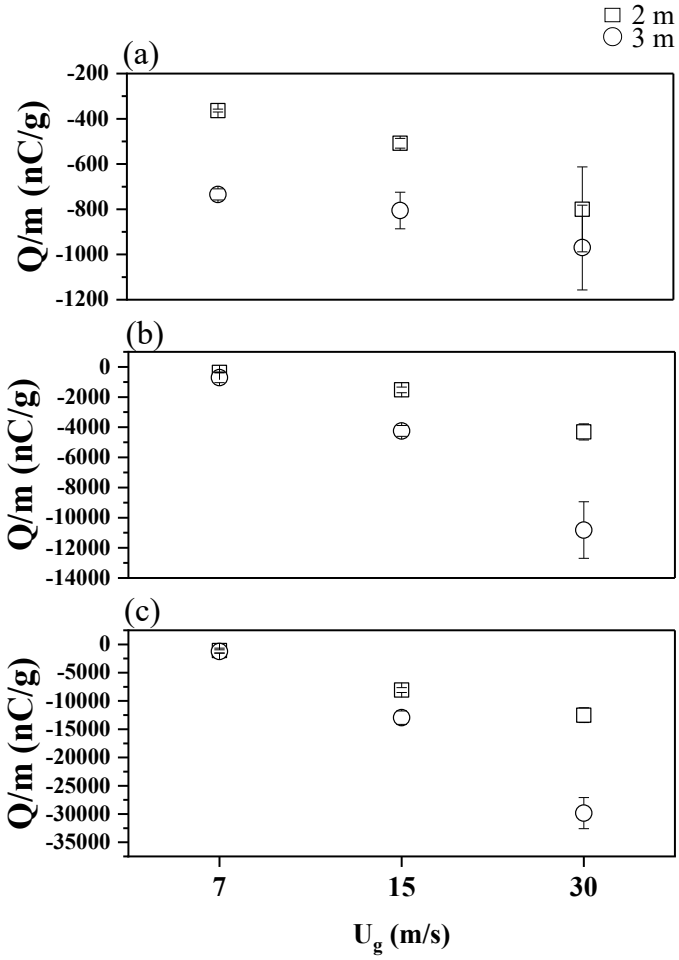

Fig. 5-7. The net specific charge of glass beads (a), non-dehydrated silica (b) and dehydrated silica (c) when conveyed at various conveying tube length and gas velocities.

As discussed earlier in section 5.3.3, particles formed dilute and/or dense plumes. In a dense plume, unlike in the dilute plume, particles are mostly concentrated at the center of the plume and thus, do not experience as many contacts with the tube wall. Therefore, the net *Q/m* of particles is expected to be smaller in dense plumes compared with dilute plumes. Fig. 5-8 shows the values of *Q/m* of different samples normalized with respect to the conveying tube length under various operating conditions. Since the generated charge depended on gas velocity and tube length, *Q/m/L* must be constant for a given gas velocity. Fig. 5-8 clearly shows that this was the case for glass beads whereas for silica particles tested at U_g of 30 m/s a discrepancy was observed. This is an indication of the influence of another parameter at such high gas velocity which would result in larger number of contacts between the particles and the tube wall. It is speculated that during transportation, the dense plumes became elongated and as a result,

particles had more opportunity to collide with the wall for this gas velocity. However, with the existing set-up we were unable to validate this proposed mechanism.

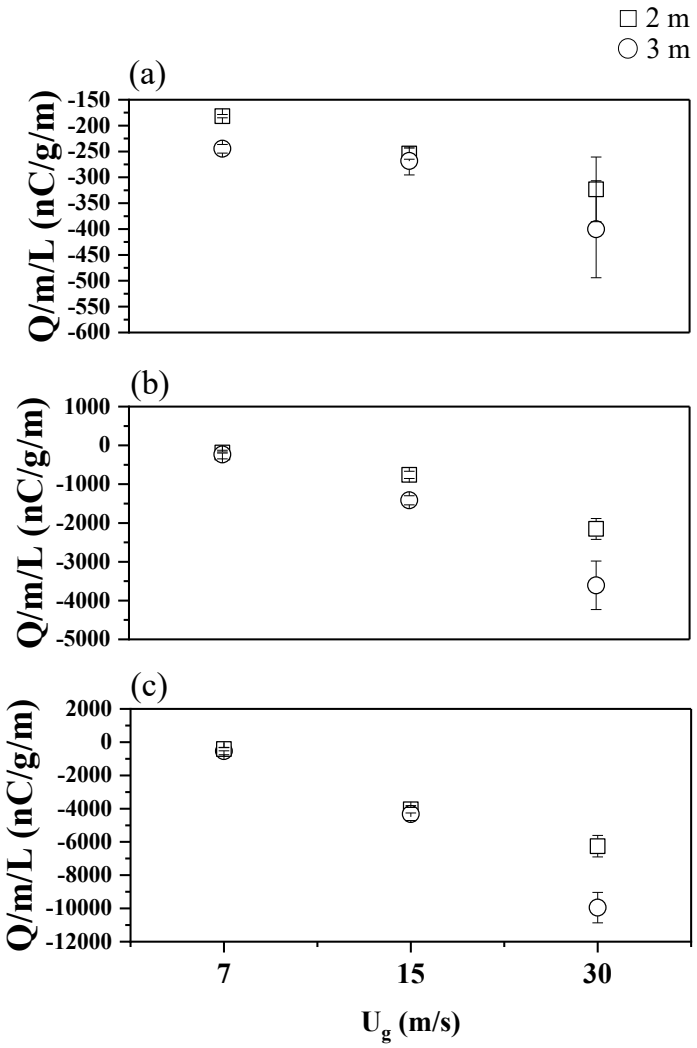

Fig. 5-8. The *Q/m/L* of glass beads (a), non-dehydrated silica (b) and dehydrated silica (c) tested at different conveying tube length and gas velocities.

5.4.2 Particle Velocity

Fig. 5-9 shows particle velocities measured by current signal and video imaging techniques in 2 and 3 m conveying tubes at various conveying gas velocities of 7±1, 15±1 and 30±1 m/s. As can be seen, particle velocities measured by the two techniques were in good agreement for almost all the operating conditions tested with the exception of the dehydrated amorphous silica where some discrepancies were observed. Analyzing the captured videos of the observed non-matching cases revealed that the plume moving patterns fell under the *signal Type-IV* case as described in

section 5.3.3. Therefore, $t_{out\text{-}adj}$ was challenging to find, and as a result particle velocity in this case was not adjusted.

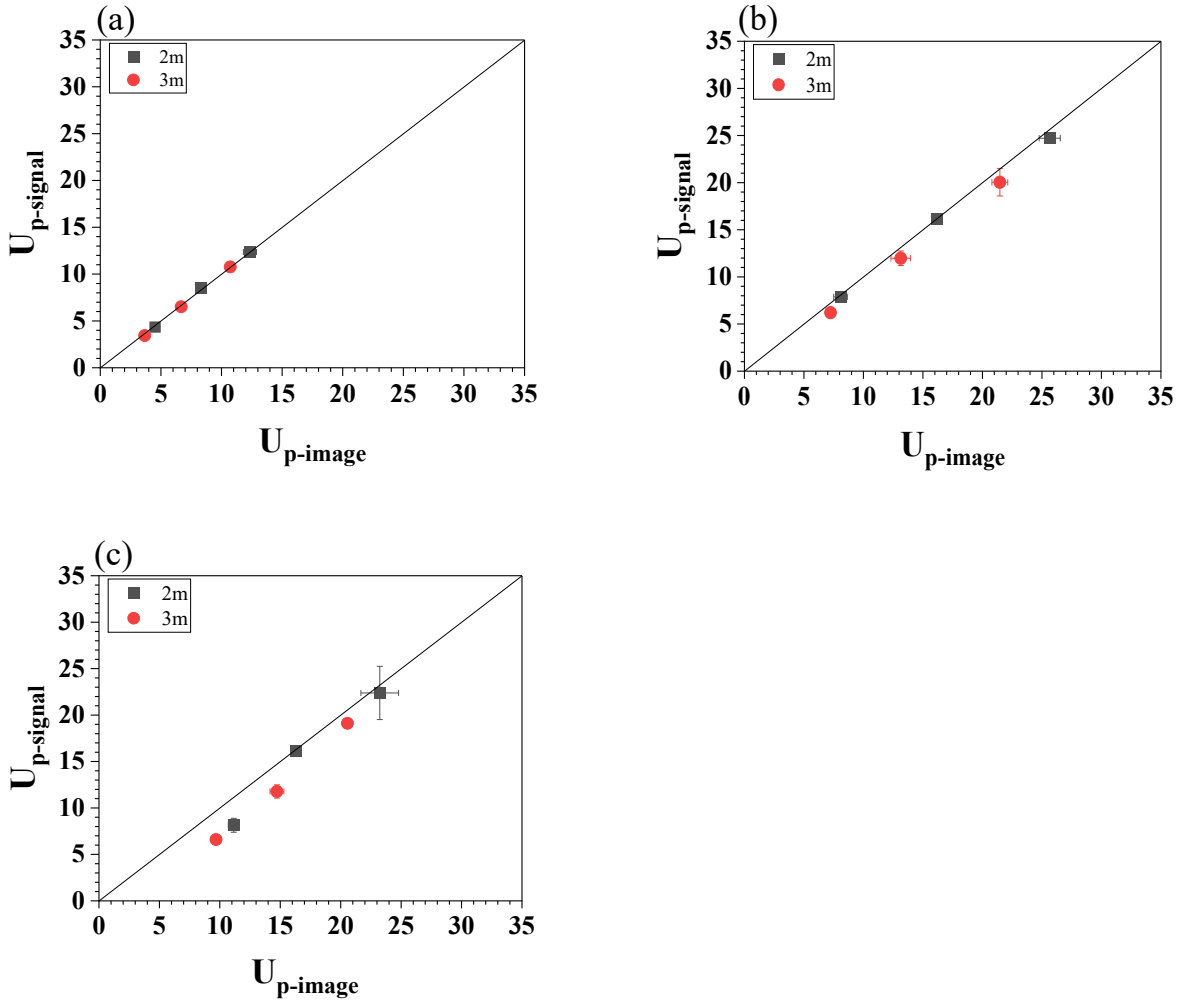

Fig. 5-9. Comparison of particle velocity of glass beads (a), non-dehydrated silica (b) and dehydrated silica (c) at 7±1, 15±1 and 30±1 m/s gas velocities in 2 and 3 m in-length conveying tubes measured by the current signal and video imaging.

Comparison of particle velocity of different samples at the same gas velocity and tube length implies that glass beads acquired a lower velocity than both types of amorphous silica particles. Furthermore, assessment of particles velocity with that of the gas velocity showed that at 7 and 15 m/s gas velocities, glass beads travelled slower than the conveying gas velocity, whereas for both types of amorphous silica particles the velocities were similar. On the other hand, at 30 m/s gas velocity, none of the particle velocities reached the gas velocity. To better visualize the deviations between U_p and U_g, the ratio of these velocities was also plotted based on the current signal method and is shown in Fig. 5-10. The observed variations can be attributed to the

Archimedes (*Ar*) number that is dependent on particle and fluid properties and shows falling intensity, resulting in powders with larger *Ar* to travel at a lower velocity than the conveying gas velocity [10]. In this work, *Ar* numbers were approximately 4 and 27 for amorphous silica and glass beads, respectively. Therefore, silica particles with a lower *Ar* number would have travelled faster at a speed closer to the conveying gas. Furthermore, pneumatically conveyed particles while suspended in a gas, experience collisions with other particles and the tube wall. Particle-particle collisions can be neglected in a dilute phase flow; however, particle-wall contacts are significant. After each collision, particles lose their initial kinetic energy and accelerate until the next collision occurs. These repeated decelerations and accelerations which are expected to be more with the elongated plums as discussed in section 5.4.1 could in turn reduce particle velocity. Also, the gas flow regime could play a role. In this work, the flow regime was turbulent at 30 m/s gas velocities which could cause more radial motion and collisions for particles. Therefore, particles need to travel a longer distance than the conveying tube actual length. In result, at larger gas *Re* numbers, particle velocity is expected to deviate more from conveying gas velocity.

Another factor that could intensify radial movement of particles is the electric field generated by electrostatic charge on the surface of particles. Our previous work [26] concludes that highly charged particles tend to migrate to the conveying tube wall and cause fouling. In this work, the mass of fouled particles was 0.04 g, 0.01 g, and almost 0 g for dehydrated amorphous silica, non-dehydrated amorphous silica, and glass beads, respectively. As shown earlier in Fig. 5-7, amorphous silica particles generated significantly more electrostatic charge at 15 and 30 m/s. Moreover, for these conditions, Fig. 5-10 illustrates that U_p/U_g decreased with respect to gas velocity. This observation is then attributed to a higher electrostatic charge generation and consequently more radial motion due to the particle's attraction towards the conveying tube wall.

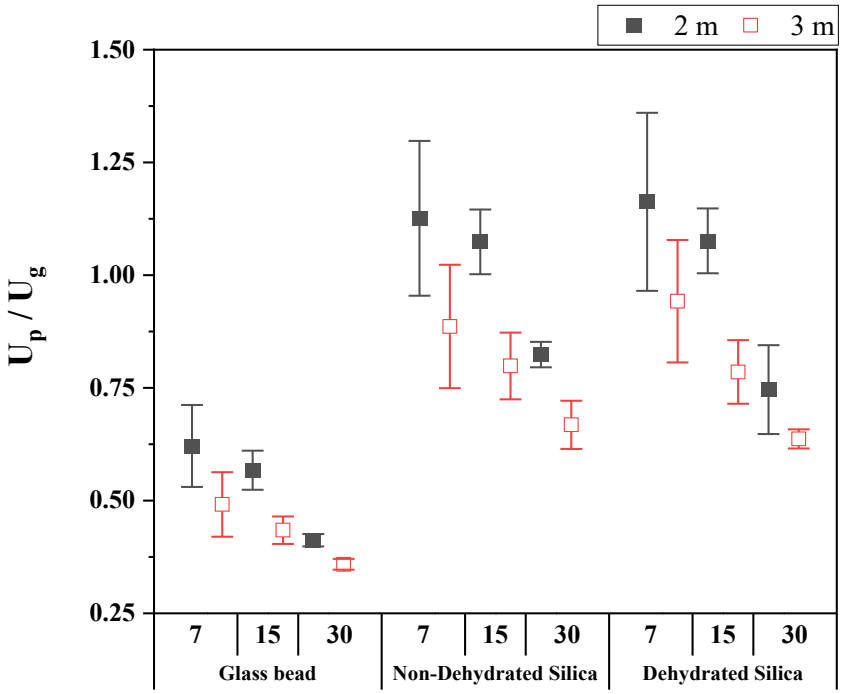

Fig. 5-10. U_p/U_g based on current signal technique for various conveying tube length and gas velocity.

Comparing results of different tube lengths implies that 3 m tube resulted in a smaller particle velocity in comparison to that of 2 m tube. As discussed in section 5.4.1, by increasing the tube length, dense plums in the conveying line became elongated and therefore, more contact between particles and the tube wall took place which resulted in a higher charge generation and in turn particles radial motion.

The results in this study clearly indicate that electrostatic charge of particles could influence conveyed particle velocity, which has not been considered in any of the proposed models in open literature. Fig. 5-11 and Fig. 5-12 compare the measured particle velocities in this work with those estimated using a number of existing models. It must be noted that the models have various limitations in relation to operating conditions tested in this work (e.g., particle size range, tube diameter, etc.). All the models predicted a linear relation between conveying gas and particle velocity. However, experimental data in this work clearly illustrates a decline in the rate of the change in particle velocity as the gas velocity approached 30 m/s. This is the condition that resulted in the largest degree of electrostatic charging on particles. Velocities calculated by the

models are also unable to predict a similar particle velocity as the average gas velocity which is a valid case for silica particles when *Ar* is small. It should be noted that even reaching a higher particle velocity than the average gas velocity was also reported by Yan and Ma [37]. The results in this work stress that the proposed models have limitations on the operating conditions at which they were derived, especially the tube diameter, and most importantly they ignore the presence of electrostatic charge that could influence the dynamics of the conveying particles and consequently particle velocity.

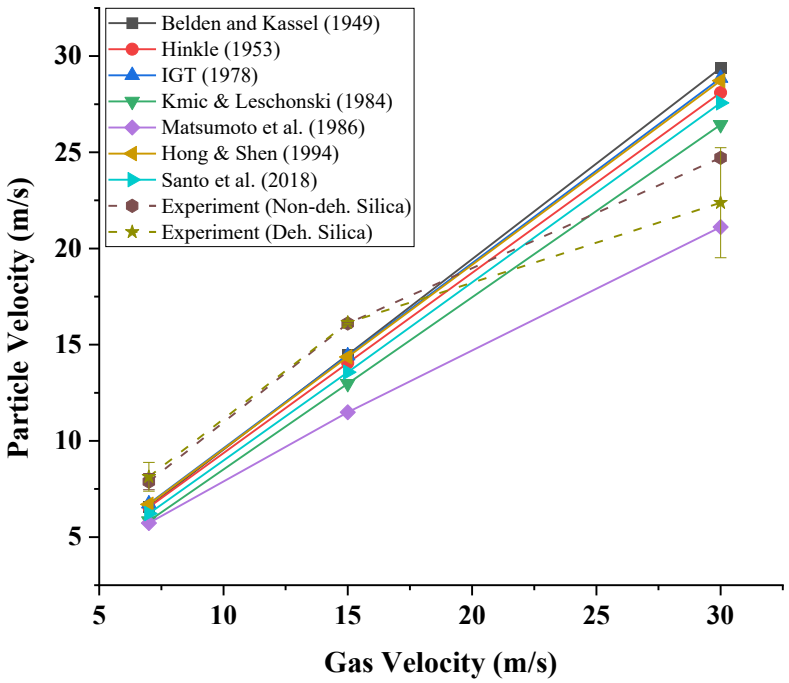

Fig. 5-11. Estimated and measured particle velocity for non-dehydrated and dehydrated amorphous silica particles in the 2 m conveying line at various conveying gas velocities.

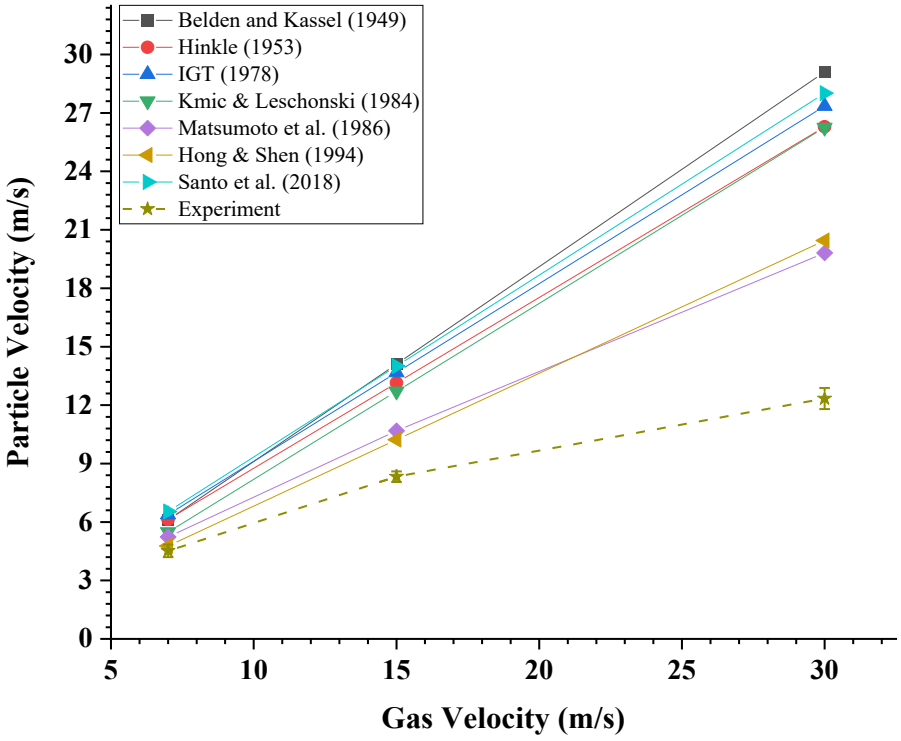

Fig. 5-12. Estimated and measured particle velocity for glass beads in the 2 m conveying line at various conveying gas velocities.

5.4.3 Back flow observation

Finally, we would like to report on an observation of a phenomenon that only occurred during pneumatic conveying of dehydrated and non-dehydrated amorphous silica particles at 15 and 30 m/s gas velocities. At these conditions, a back flow of particles at the end of the plume was observed (Fig. 5-13). As such, particles were traveling in opposite direction of the gas flow in a parabolic flow pattern in which particles seemed to have a higher velocity at the center of the back flow, even though this was the region where the drag force on the particles must be at a maximum. On the other hand, when the transparent tube was relocated to the inlet of the conveying tube, no back flow was observed. It is suspected that the electrostatic charge of the particles was the contributing factor. Amorphous silica particles possessed a significant amount of surface charge by the time they reached the tube outlet, which would have generated a strong electric field and as a result overcoming the drag force. It is also important to mention that for these test conditions the greatest amount of fouling was observed at the tube outlet which could have resulted in a strong repulsion and in turn pushing the particles backwards. This observation

could be an example of the influence of the conveyed particles' electrostatic charge on their flow dynamics and thus requires further investigation.

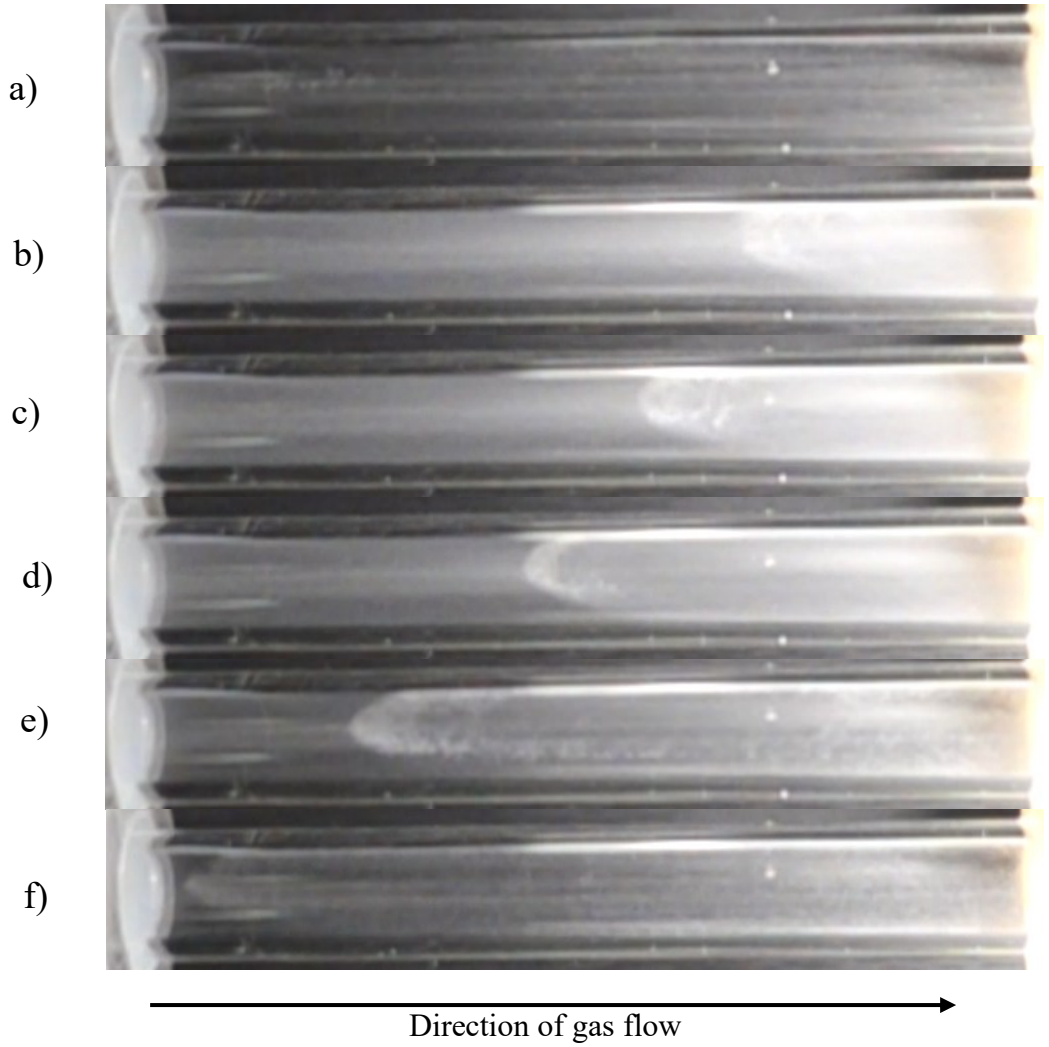

Fig. 5-13. An example of back flow observed for non-dehydrated amorphous silica particles at 15 m/s gas velocity in a 3 m in length tube. Direction of gas flow is from left to right. a) t<0 only air is passing through, b) t=0 s when the back flow is first seen, c) t=0.2 s, d) t=0.4s, e) t=0.6, f) t=0.8 s.

5.5 Conclusion

In this work, a modified particle velocity method using electrical current signal analysis was proposed and tested and results showed that it has simplicity and reliability. The particles velocity of fine glass beads as well as dehydrated and non-dehydrated amorphous silica particles were measured while being pneumatically conveyed in a narrow stainless-steel tube. Particle velocity was also measured by using video imaging technique and results were in good agreement with the new proposed method. It was shown that in pulse injection of different samples, particles in the conveying line travelled in dense and dilute plumes where the plumes could become elongated, in turn increasing the charge generated on the surface of the particles by increasing the number of particle-wall contacts. Charge of particles was also elevated when gas velocity increased to exemplify a turbulent flow regime at which more radial motion of particle was expected. This change in motion of particles was proposed as the main reason for the greater deviation that was observed between the conveying gas and the particle velocity. The comparison between the particle velocities predicted by some existing models and those measured in this work, as well as particles flow pattern observations made in this study (i.e., the occurrence of back flow), suggest the necessity of more fundamental work to be carried out to study the effect of particles electrostatic charge on their motion patterns and conveying velocity.

References

[1] G.E. Klinzing, F. Rizk, R. Marcus, L.S. Leung, Pneumatic Conveying of Solids, Springer, 2010.

[2] W. Wei, G. Qingliang, W. Yuxin, Y. Hairui, Z. Jiansheng, L. Junfu, Experimental study on the solid velocity in horizontal dilute phase pneumatic conveying of fine powders, Powder Technol. 212 (2011) 403–409.

[3] D.H. Belden, L.S. Kassel, Pressure Drops Encountered in Conveying Particles of Large Diameter in Vertical Transfer Lines, Ind. Eng. Chem. 41 (1949) 1174–1178.

[4] B.L. Hinkle, Acceleration of particles and pressure drops encountered in horizontal pneumatic conveying, (1953).

[5] G.E. Klinzing, N.D. Rohatgi, A. Zaltash, C.A. Myler, Pneumatic transport - a review (generalized phase diagram approach to pneumatic transport), Powder Technol. 51 (1987) 135–149.

[6] A. Kmiec, K. Leschonski, An experimental study of the pressure drop of gas-solids suspension flow in vertical pipes, Chem. Eng. J. 29 (1984) 51–56.

[7] S. Matsumoto, H. Harakawa, M. Suzuki, S. Ohtani, Solid particle velocity in vertical gaseous suspension flows, Int. J. Multiph. Flow. 12 (1986) 445–458.

[8] G.E. Klinzing, C.A. Myler, A. Zaltash, S. Dhodapkar, A simplified correlation for solids friction factor in horizontal conveying systems based on Yang's unified theory, Powder Technol. 58 (1989) 187–193.

[9] J. Hong, Y.S. Shen, Flow characteristics of high density continuous conveying of solids, Chem. Metall. 15 (1994) 122–128.

[10] N. Santo, D. Portnikov, I. Eshel, R. Taranto, H. Kalman, Experimental study on particle steady state velocity distribution in horizontal dilute phase pneumatic conveying, Chem. Eng. Sci. 187 (2018) 354–366.

[11] H. Taofeeq, S. Aradhya, J. Shao, M. Al-Dahhan, Advance optical fiber probe for simultaneous measurements of solids holdup and particles velocity using simple calibration methods for gas-solid fluidization systems, Flow Meas. Instrum. 63 (2018) 18–32.

[12] M.P. Mathur, G.E. Klinzing, Flow measurement in pneumatic transport of pulverized coal, Powder Technol. 40 (1984) 309–321.

[13] A.A. Vetter, F.E.C. Culick, Acoustical resonance measure- ment of particle loading in gas-solids flow, J. Eng. Gas Turbines Power. 109 (1987) 331–335.

[14] J.D. King, W.L. Rollwitz, Magnetic resonance measurement of flowing coal, ISA Trans. 22 (1983) 69–76.

[15] S. Kobyashi, S. Miyahara, Development of microwave powder flowmeter, Instrum. 27 (1984) 68–73.

[16] M.D. Atkins, Velocity Field Measurement Using Particle Image Velocimetry (PIV), Elsevier Inc., 2016.

[17] S.R. Woodhead, A.N. Pittman, S.J. Ashenden, Laser Dopler Velocimetry Measurements of Particle Velocity Profiles in Gas-Solid Two-Phase Flows, (1995) 770–773.

[18] W.B. Zhang, T.Y. Wang, Y.Y. Liu, W.B. Zhan, C.H. Wang, Particle velocity measurement of binary mixtures in the riser of a circulating fluidized bed by the combined use of electrostatic sensing and high-speed imaging, Pet. Sci. 17 (2020) 1159–1170.

[19] X. Qian, Y. Yan, L. Wang, J. Shao, An integrated multi-channel electrostatic sensing and digital imaging system for the on-line measurement of biomass – coal particles in fuel injection pipelines, Fuel. 151 (2015) 2–10.

[20] Y. Yan, B. Byrne, S. Woodhead, J. Coulthard, Velocity measurement of pneumatically conveyed solids using electrodynamic sensors, Meas. Sci. Technol. 6 (1995) 515–537.

[21] Y. Yan, Mass flow measurement of bulk solids in pneumatic pipelines, Meas. Sci. Technol. 7 (1996) 1687–1706.

[22] H. Masuda, S. Matsusaka, H. Shimomura, Measurement of mass flow rate of polymer powder based on static electrification of particles, Adv. Powder Technol. 9 (1998) 169–179.

[23] S. Matsusaka, H. Fukuda, Y. Sakura, H. Masuda, M. Ghadiri, Analysis of pulsating electric signals generated in gas-solids pipe flow, Chem. Eng. Sci. 63 (2008) 1353–1360.

[24] M. Taghavivand, Role of Catalyst Support and Continuity Additives on the Degree of Electrostatic Charging and Reactor Fouling in Polyethylene Gas-solid Fluidized Bed Reactors, University of Ottawa, 2021.

[25] M. Taghavivand, P. Mehrani, A. Sowinski, K. Choi, Electrostatic charging behaviour of polypropylene particles during pulse pneumatic conveying with spiral gas flow pattern, Chem. Eng. Sci. 229 (2021) 116081.

[26] M. Taghavivand, B.J. Cho, P. Mehrani, A. Sowinski, Electrostatic charging behaviour of a silica powder during pulse pneumatic conveying, Powder Technol. 366 (2020) 119–129.

[27] E.W.C. Lim, Y. Zhang, C.H. Wang, Effects of an electrostatic field in pneumatic conveying of granular materials through inclined and vertical pipes, Chem. Eng. Sci. 61 (2006) 7889–7908.

[28] Y. Zhang, E.W.C. Lim, C.H. Wang, Pneumatic transport of granular materials in an inclined conveying pipe: Comparison of computational fluid dynamics-discrete element method (CFD-DEM), electrical capacitance tomography (ECT), and particle image velocimetry (PIV) results, Ind. Eng. Chem. Res. 46 (2007) 6066–6083.

[29] E.W.C. Lim, J. Yao, Y. Zhao, Electrostatic effects in pneumatic transport of granular materials, 19 (2012) 351–361.

[30] G.E. Klinzing, A review of pneumatic conveying status, advances and projections, Powder Technol. 333 (2018) 78–90.

[31] D.M. Gooding, G.K. Kaufman, Tribocharging and the Triboelectric Series, Encycl. Inorg. Bioinorg. Chem. (2014) 1–9.

[32] H. Zou, Y. Zhang, L. Guo, P. Wang, X. He, G. Dai, H. Zheng, C. Chen, A.C. Wang, C. Xu, Z.L. Wang, Quantifying the triboelectric series, Nat. Commun. 10 (2019) 1–9.

[33] S. Jantač, L. Konopka, J. Kosek, Experimental study of triboelectric charging of polyethylene powders: Effect of humidity, impact velocity and temperature, Adv. Powder Technol. 30 (2019) 148–155.

[34] F. Chowdhury, A. Sowinski, M. Ray, A. Passalacqua, P. Mehrani, Charge generation and saturation on polymer particles due to single and repeated particle-metal contacts, J. Electrostat. 91 (2018) 9–15.

[35] W.D. Greason, Investigation of a test methodology for triboelectrification, J. Electrostat. 49 (2000) 245–256.

[36] E. Krause, Fluid mechanics: With problems and solutions, and an aerodynamic laboratory, Fluid Mech. With Probl. Solut. an Aerodyn. Lab. (2008) 1–354.

[37] Y. Yan, J. Ma, Measurement of particulate velocity under stack-flow conditions, Meas. Sci. Technol. 11 (2000) 59–65.

Chapter 6 - Conclusions and Recommendations

Electrostatic charge generation is an inherent phenomenon in various gas-solid processes, such as pneumatic conveying and fluidization, arising from the contacts among solids and with neighbouring surfaces. Buildup of electrostatic charge within a unit operation can pose undesirable consequences and significant operational challenges including particle agglomeration, fouling, and electrostatic discharge in the form of sparks. For instance, a critical challenge that persists with the operation of commercial gas-phase polyethylene fluidized bed reactors is the presence of electrostatics that results in formation of undesired aggregates that affect product quality and reactor wall fouling/sheeting; challenges that requires reactor shutdown for cleaning with associated high cost of cleaning and loss of production (nearly $2.0M/day). Therefore, a thorough understanding of the primary sources that influence electrostatic charge generation in the gas-solid fluidized bed reactors, such as in PE process, is critical. Comprehensive understanding of the underlying sources is an essential step to develop techniques to regulate and suppress charge generation within these systems to improve process efficiency and minimize economic losses.

Although numerous studies have explored the electrostatic phenomenon in PE reactors, the majority have focused solely on the charging behavior of PE resin under operating conditions that are not completely relevant to industrial conditions. Therefore, this thesis presented a novel investigation on determining the extent of electrostatic charging of a commercially produced linear low-density polyethylene resin fluidized at elevated pressures (up to 2600 kPa) and temperatures (up to 58ºC). In addition, this thesis aimed at establishing a preliminary study on determining the effect of complex chemistry of catalysts that coexist with PE resin in commercial reactors on the bed electrification and wall fouling.

6.1 Conclusions

In the first phase, this study delved into the impact of fluidization temperature on contact electrification of a commercially produced LLDPE resin and its fouling tendency within a pilot plant pressurized fluidized bed. Fluidization at 2600 kPa, resulted in a substantial decline in the amount fouling, approximately 72.5%, when fluidization temperature was increased from ambient to 58ºC. Findings revealed that as temperature increased, the net specific charge of fluidized particles in the bulk of the bed decreased, and thus, the fouling of particles on the

column wall was reduced. To gain a more comprehensive understanding of the factors contributing to this decline, the next research step concentrated on conducting bench-scale shake testing. The experimental setup involved shaking the PE resin at both ambient temperature and 60ºC inside two small stainless-steel cups, with one of the cups having its wall coated with PE resin. Through shake tests, we systematically examined the generation of electrostatic charge in different contact scenarios, including insulator-insulator and metal-insulator contacts. Regardless of temperature variations, particles in contact with stainless-steel exhibited consistent charge transfer. In contrast, contacts involving the coated wall showed a reduced generation of electrostatic charge at higher temperatures, which was similar to the fluidization results. The materials' volume resistivity was believed to explain the observed phenomenon. To gauge changes in volume resistivity with temperature, a volume resistivity cell was constructed in-house based on ASTM D257 standards. The investigation revealed a decline in the volume resistivity of different insulating films at 60ºC comparing to ambient temperature. Furthermore, this study, based on the experimental data from the volume resistivity cell, concluded an enhanced charge carrier mobility and an increase in dissipation of charge to the ground with rising temperature for insulator-insulator contacts. Although the breakdown voltage of the surrounding gas was also identified as a potential factor influencing contact electrification, its impact was deemed negligible within the temperature range investigated. While this investigation primarily focused on the electron transfer mechanism among the three main charge transfer mechanisms, it underscored the necessity for further exploration into the potential effects of temperature on ion transfer and material transfer mechanisms.

In the second phase, in an effort to replicate operating conditions relevant to commercial PE fluidized bed reactors, this thesis also focused on experimentations where catalysts and PE resin coexist. For the first time, a preliminary work was established to gain a comprehensive understanding of the role of a typical metallocene (MCN) catalyst in PE fluidized bed electrification and wall fouling formation. A systematic approach was adopted where electrostatic charge inducing behaviour of all components present in a MCN catalyst, namely the catalyst base (dehydrated amorphous silica) and cocatalyst (methylaluminoxame (MAO)), was examined individually. The static charging of these powders was not only investigated during their pneumatic conveying but also during their contact with PE resin within an atmospheric fluidized bed. In each experiment, at minimum fluidization velocity, the catalyst base, the

cocatalyst, and the MCN catalyst were introduced into the fluidization column via pneumatic conveying (with similar material and dimension as that of the catalyst conveying lines in commercial processes). The powders were used in their active and deactivated forms at two concentrations of 100 and 1000 ppm. The conclusions are as follow:

a) In the conveying line, although silica particles exhibited a negative polarity with the greatest charge magnitude, active MAO and MCN particles showed 80% and 90% decline in the charge, respectively. This indicated a complete coverage of the silica catalyst base surface by MAO or the catalyst elements.
b) Fluidization experiments in the presence of powders at low concentrations (i.e., 100 ppm) did not influence the tribocharging of PE particles in the bed. However, at 1000 ppm concentrations there was a noticeable change in the net charge of the bed and the mass of fouled layer on the wall.
    - Active MAO substantially (approximately by a factor of four) reduced the column wall fouling. It was suspected that active MAO particles experienced a breakdown in their chemical structure and produced $[\text{-AlMe}_2]^+$ and negative MAO ions. These ions were responsible for the mitigation of the charge generation in the bed, particularly for small particles, and in turn, reducing fouling.
    - This study suggests that MAO could potentially play a similar role to static control agents (or continuity additives (CAs)), and thus, could partially replace the usage of static control agents. This finding is significant since it is advantageous for the PE industry to employ a static suppressant agent that would not only demote catalyst's activity but also assist in reducing sheeting. This could be an effective method in regulating charge generation without impacting the established process severely.
    - Active MCN catalyst caused a substantial increase in the amount of fouling without altering the net specific charge of particles in the bulk, as the result of retaining the fine particles in the bed.
    - Adding continuity additives to MCN catalyst was promising in reducing the magnitude of fouling in comparison with MCN without CA; however, the results were similar to those observed in PE experiments.

- Deactivated MCN catalyst altered the polarity of the bed from positive to negative and increased the amount of fouling.
- It was proposed that powders with acidic properties (i.e., silica and deactivated MCN catalysts) induce a negative polarity to the PE bed, and powders which could undergo ionization such as MAO mitigate the net specific charge of the bed and fouling formation.

Finally, this thesis aimed at studying the influence of the electrostatic charge that powders acquire through pneumatic conveying on their conveying velocity. This study involved pulse feeding pneumatic conveying and a new particle velocity measurement technique which was developed based on electrical current signal analysis and was compared with video imaging technique. The pulse injection of fine glass beads, as well as dehydrated and non-dehydrated amorphous silica particles was performed in a 0.00475 m stainless-steel tube at conveying gas velocities of 7, 15, and 30 m/s. We concluded that the current signal analysis is a reliable method to measure particle velocity, as evidenced by consistent results from the video imaging technique. This study also revealed that particles obtained more electrostatic charge as the gas velocity was raised and the particle's plume became elongated in the tube, providing more chance for particles in the middle of the plum to contact with the tube wall. Furthermore, at greater conveying gas velocities, a larger deviation between gas and particle velocities was observed which was attributed to the turbulency of gas flow and tribocharging of particles. Comparison between particle velocities predicted by existing models in literature and those measured in this study, along with observations of particle flow patterns, including instances of backflow, emphasized the need for continued exploration to refine existing models and enhance our comprehension of particle behavior in pneumatic conveying in the presence of electrostatic charge.

6.2 Recommendations for Future Work

This thesis explored the influence of temperature and a common type of metallocene catalyst on contact electrification within a PE fluidized bed and its column wall fouling. Nevertheless, certain unknown parameters still require further investigation. Hence, the following recommendations are proposed for potential future studies:

a) The influence of temperature on contact electrification was exclusively studied for PE particles in this thesis. It is recommended to expand the experiments to other types of insulators, such as polypropylene, nylon 6/6, and Teflon.
b) In this thesis, non-ionic materials were examined, and thus, the influence of temperature on charge transfer mechanisms was only limited to electron transfer. Therefore, it is recommended to explore the effect of temperature for cases where ion transfer and material transfer mechanisms are involved.
c) This research investigated the impact of various elements on an active metallocene catalyst, particularly in terms of fouling formation and electrostatic charge generation. Given the diverse catalyst types used in the PE production industry and their complex chemistry, it is essential to extend these studies to include other catalysts, such as Ziegler-Natta catalysts.
d) This research proposed that MAO could act as a static control agent. This was observed for a large concentration of 1000 ppm while in relation to real reactors such a large concentration maybe not be feasible. Thus, it is recommended to examine smaller MAO concentrations to determine the ideal concentration that still be beneficial with respect to the mitigation of wall fouling.
e) None of the existing models found in literature that are used for predicting particle velocity in pneumatic conveying systems consider the electrostatic charge of the conveyed solids. Therefore, performing experiments and simulations with various tube materials and dimensions, particle diameters and particle types are suggested to develop new models incorporating the static charging of particles.

Appendix A – Experimental Equipment

This appendix illustrates experimental equipment employed in performing different experiments.

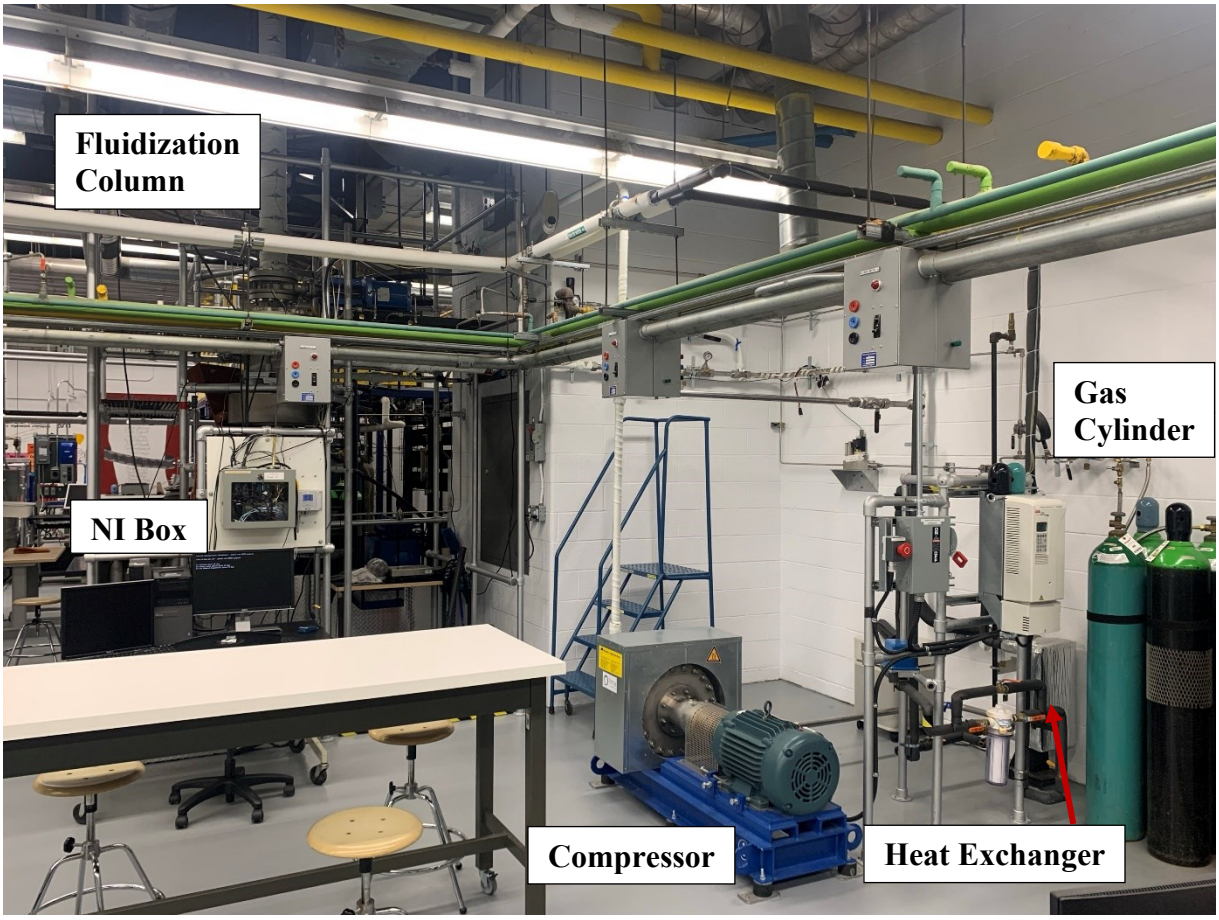

Fig. A - 1. Pilot-scale fluidization system

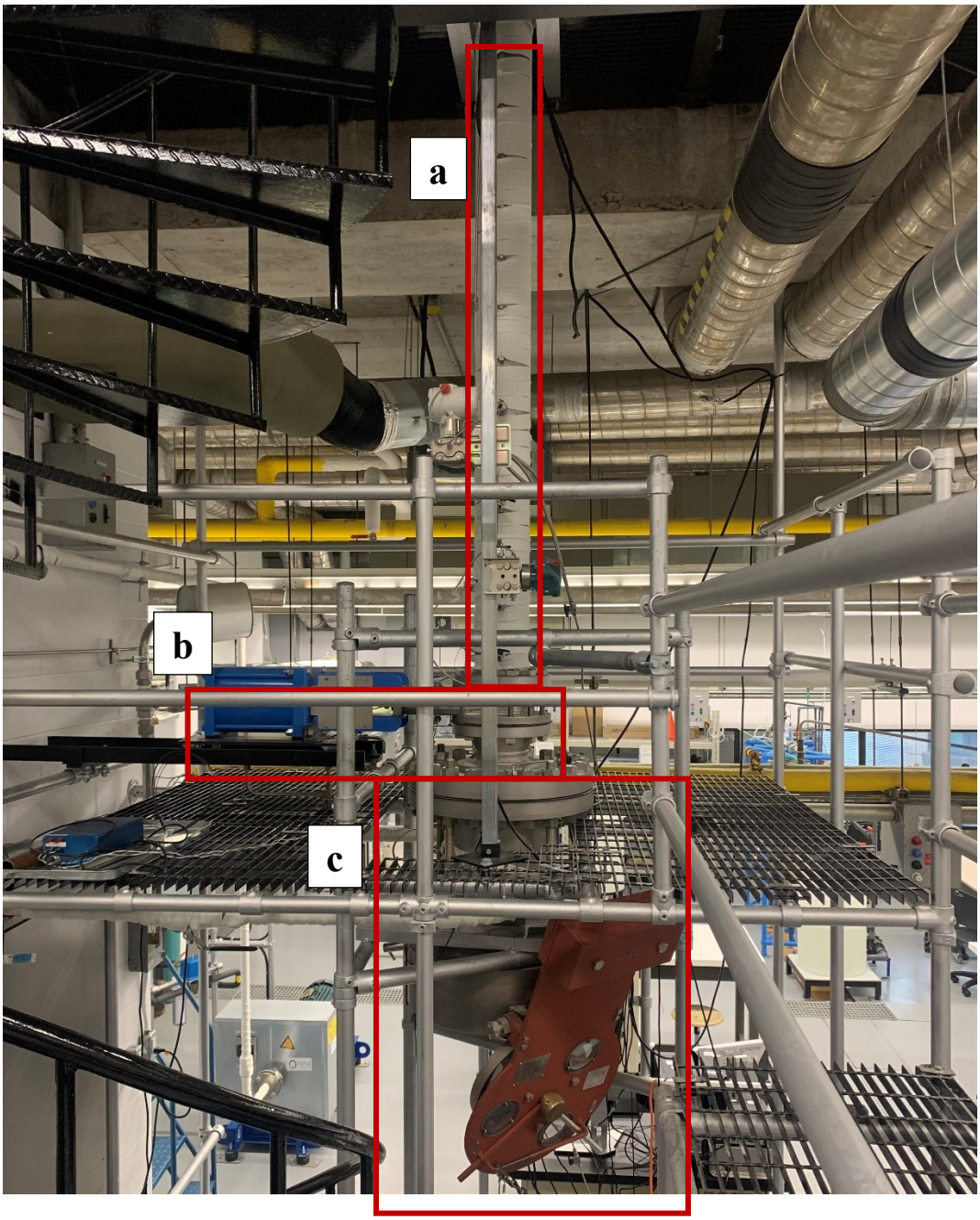
a
b
c

Fig. A - 2. This image outlines the different parts of the fluidization system. a) fluidization column, b) bottom manway, c) the knife gate valve used as a distributor plate, and d) top manway

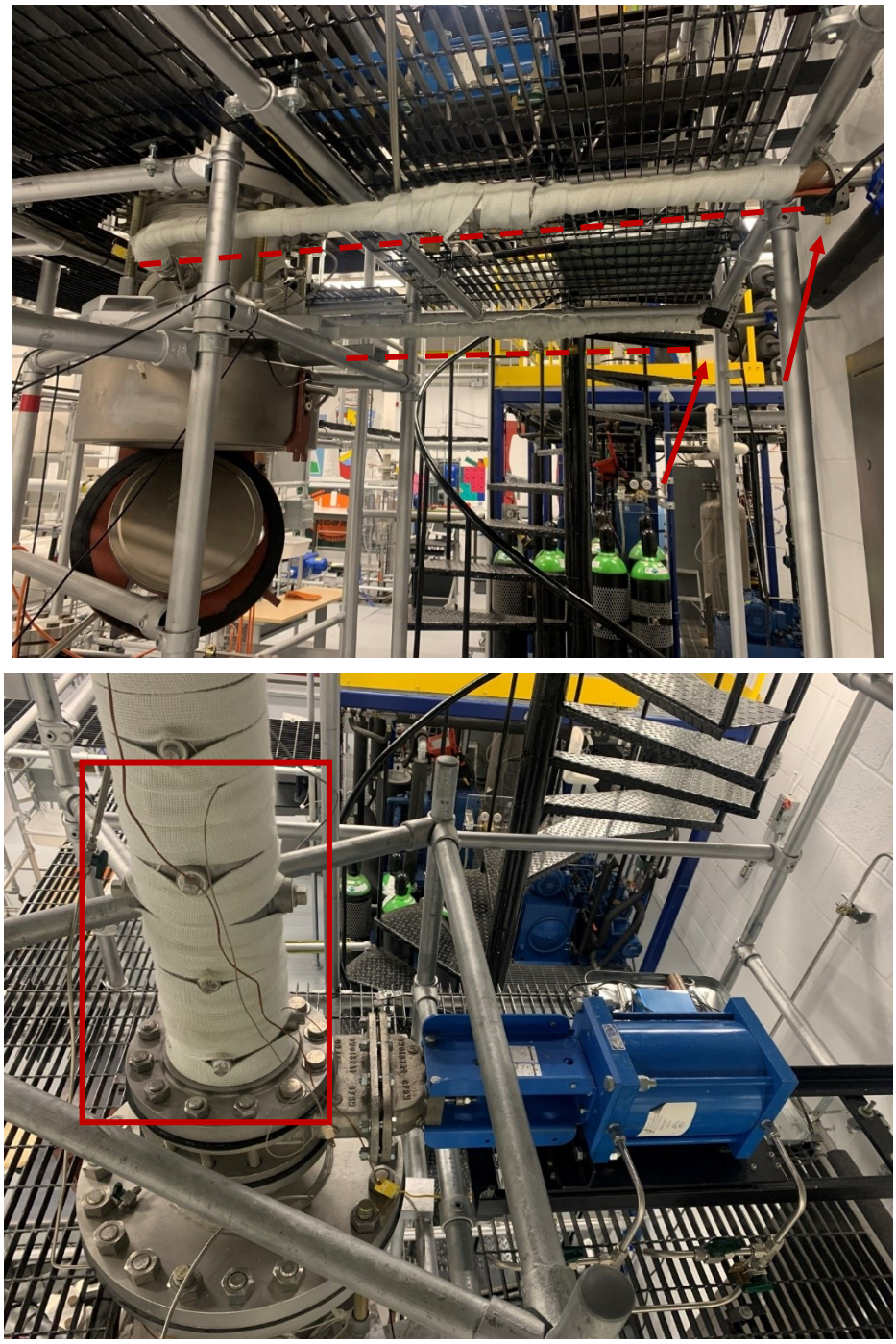

Fig. A - 3. Band heaters around the inlet pipes and the fluidization column

Fig. A - 4. Shake test apparatus in a glove box filled with nitrogen

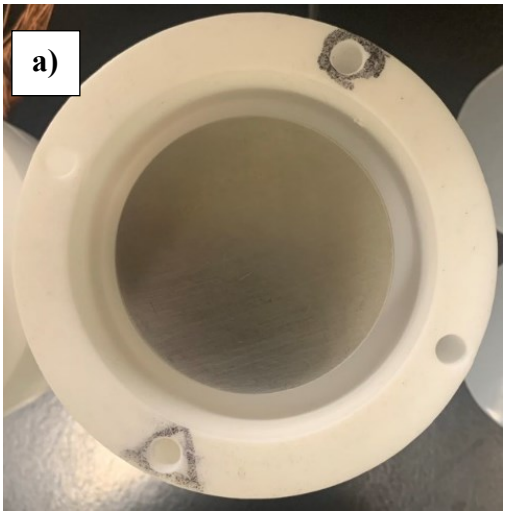

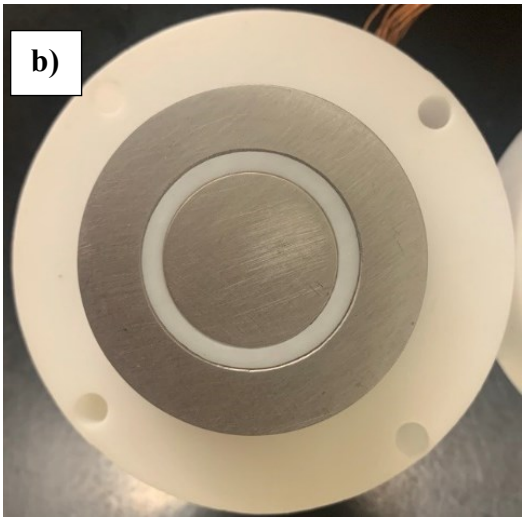

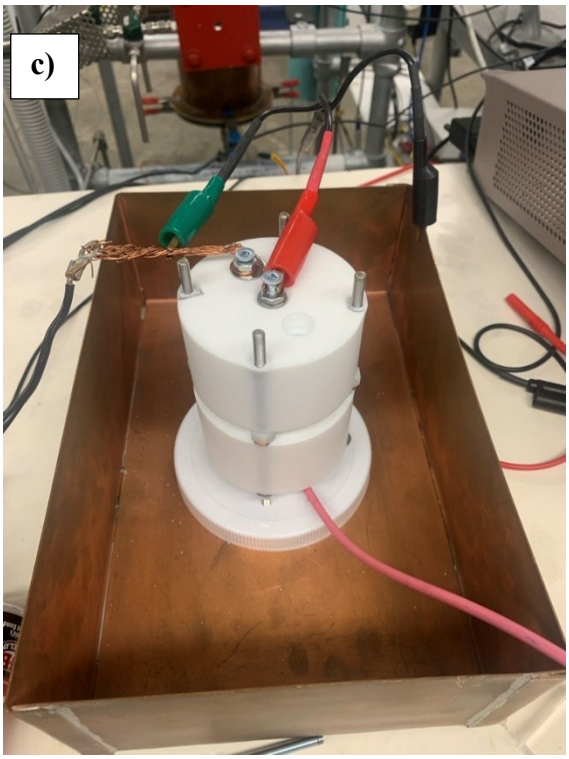

Fig. A - 5. Volume resistivity measurement cell. a) potential electrode, b) current and ground electrodes, c) red: electrometer (current), green and black: ground, pink: power supply (voltage)


Conveying tube


Fluidization Column

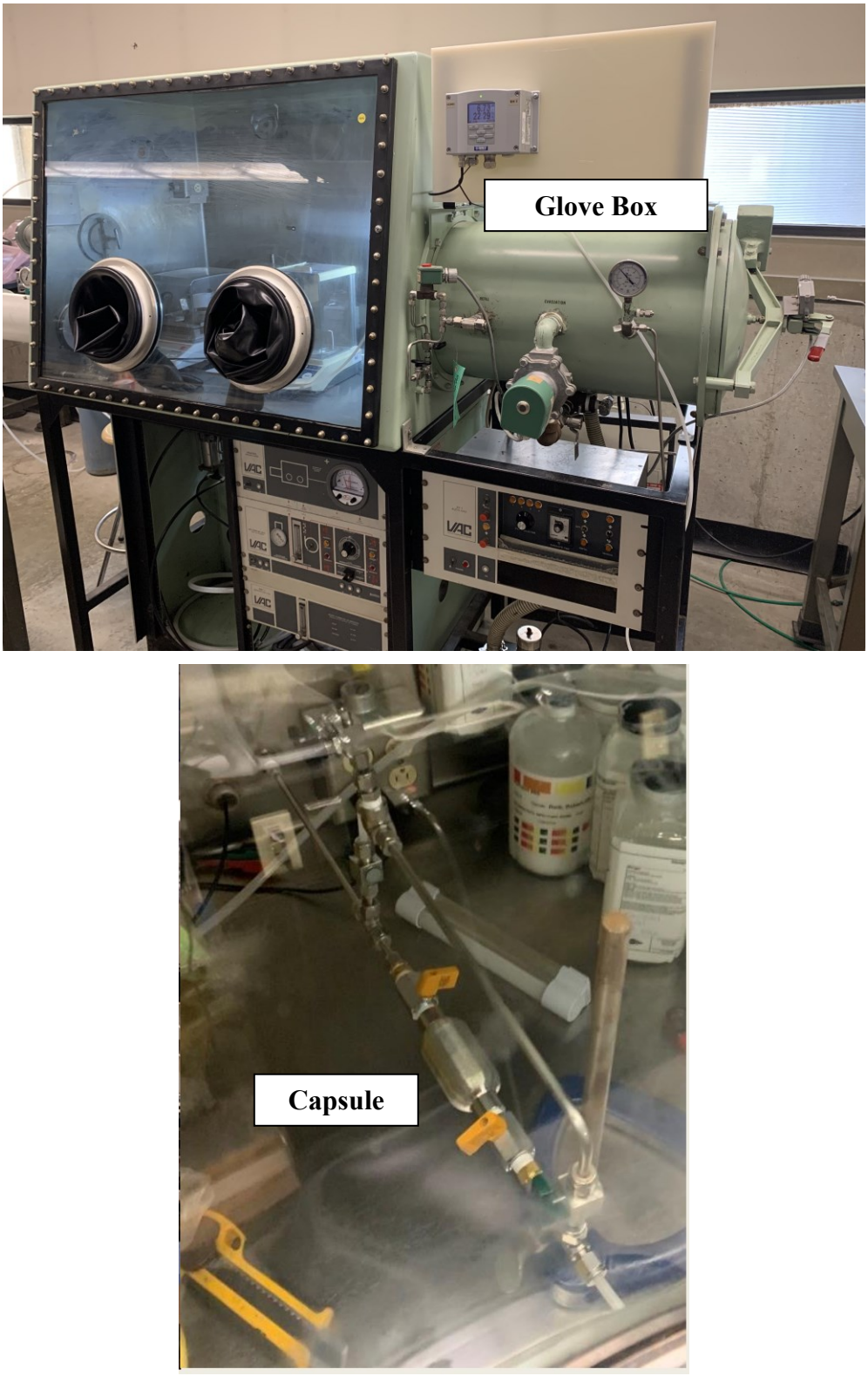

Fig. A - 6. Atmospheric fluidization apparatus along with the injection capsules attached to the pneumatic conveying line inside a glove box.

Fig. A - 7. Particle size distribution measurement techniques. a) Sieve test, b) Malvern Mastersizer 2000.

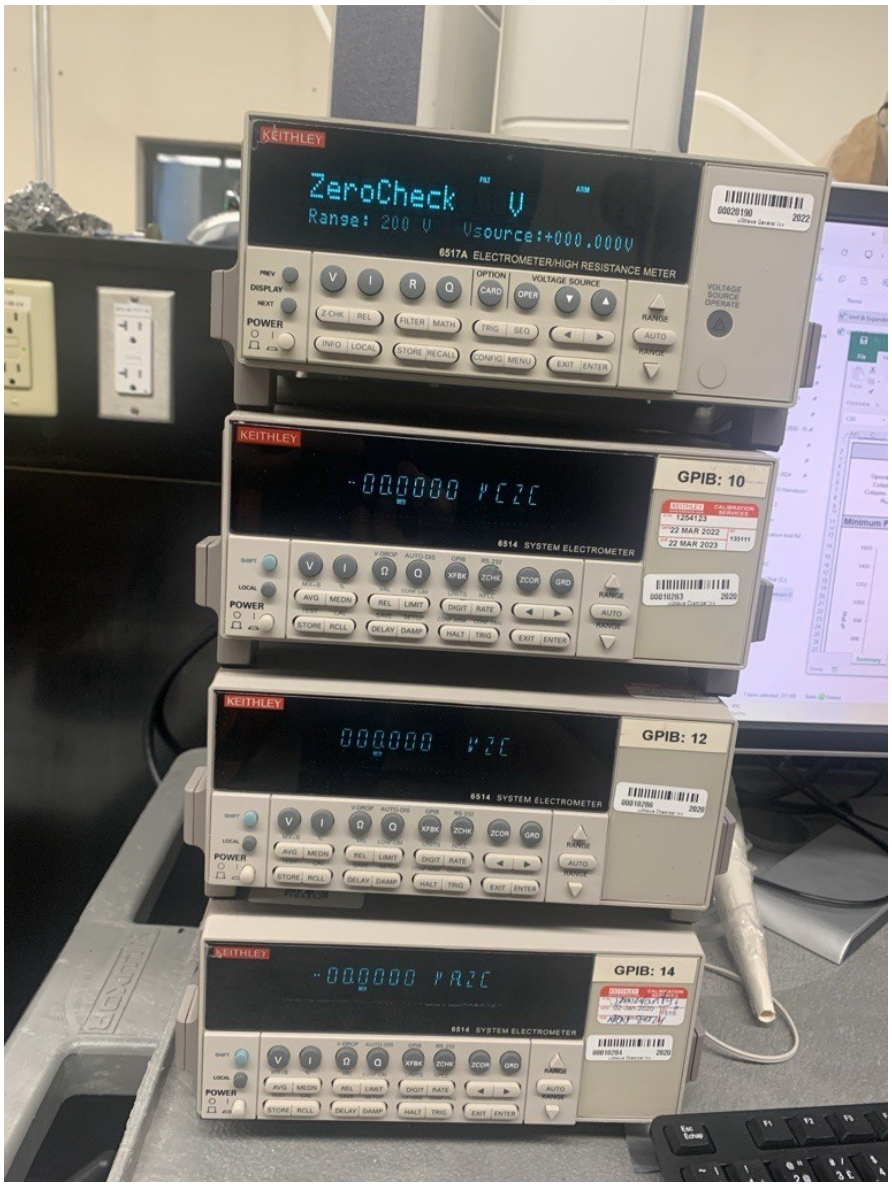

Fig. A - 8. 6517A and 6514 Keithley electrometers

Appendix B – Active Catalyst Injection & Gas-Solid Fluidization Procedure

The experimental procedure outlined below involves the atmospheric fluidization set up located in CBY-D215 with its schematic shown in Figure 1 and Figure 2. The procedure is related to runs involving the injection of powders (e.g., active catalyst) using pre-loaded capsules received from Univation Technologies.

Procedure for Sample Injections

1- While valves V-6 and V-7 located at the two ends of the capsule remain closed, place the capsule in the glove box and attach it to the N_2 inlet tubing.
2- Insert the pneumatic conveying tube into glove box through the designated port at the back of the glove box and connect it to valve V-7. This step is performed while valve V-1 is open and purging the glove box with N_2 to avoid in-flow of air during insertion.
3- Connect the other end of conveying tube to the fluidization column and connect Electrometer 3 to the tubing.
4- Mount the Faraday cage at the bottom of the fluidization column and connect to Electrometer 1.
5- Close the knife gate valve to place the distributor plate.
6- Pour 1 kg polyethylene into fluidization column from top.
7- Secure the filter bag and the Faraday cage at the top of the column and connect to Electrometer 2. (*Note: Filter bag contains multiple layers of a filter material referred to as "dust luck filter" containing some adhesives which trap the elutriated particles*)
8- Connect the outlet of the top Faraday cage to the fume hood.
9- **Purge fluidization column:** Open valve V-3 and close V-4, then using MFC-1 pass N_2 through fluidization column at 0.25 U_{mf}.
10- **Purge conveying line:** Open valve V-2 and close valve V-5, then using MFC-2 pass N_2 through the conveying line with 15 m/s velocity using the bypass around the capsule (open V-8 and V-9 while V-10 remains closed).
11- Continue purging N_2 in steps 9 and 10 for 30 min.
12- Start recording charge and current measurements from Electrometer 2 and 3, respectively.
13- Increase fluidization gas velocity to U_{mf}.
14- **Sample injection (redirect flow from bypass to the capsule):**
    a. Open V-10.

b. Close V-9.
c. Open V-7.
d. Close V-8 while opening V-6 simultaneously.

15- Stop MFC-2 after 40 s (the maximum time for the electrometer to record data in *medium* mode)

16- Increase fluidization gas velocity to $1.5U_{mf}$ and continue fluidization for 1 hr.

17- Shut down fluidization gas.

18- Note the final charge of *Fine* particles in the filter bag (Electrometer 2).

19- Start recording charge measurements from Electrometer 1.

20- Open the distributor plate to drop the *Bulk* particles into the bottom Faraday cage and measure the charge of particles (Electrometer 1).

21- Catalyst deactivation:

a. Switch the gas-flow through MFC-1 and MFC-2 to dried building air (close valves V-2 and V-3, and open valves V-4 and V-5).
b. Pass air through fluidization column and the conveying tube at low gas velocity ($0.25U_{mf}$ for column, 5 m/s for conveying tube). The reaction products leave the system to the fume hood.
c. Stop after 15 min.

22- Remove top Faraday cage and filter bag to measure the mass of *Fine* Particles; contain the filter bag in a small bag to prevent any spill of powder.

23- Remove bottom Faraday cage to measure the mass of *Bulk* Particles.

24- **Wall fouling removal**:

a. Re-mount the bottom Faraday cage and connect it to Electrometer 1.
b. Insert a tube from the top of the column and pass air through it to dislodge particles from the column wall.
c. Remove bottom Faraday cage to measure the mass of *Wall* Particles.
d. Perform these steps (24a to 24c) for each region on the column wall, starting with *Fouling-Bottom* (up to 35 cm above the distributor plate), then *Fouling-Top* (30 cm to 65 cm above the distributor plate), and finally *Freeboard* (the rest of the column to the filter bag).

25- Clean the inside of the fluidization column using wet towels. Dispose of the used towels along with all the particles as a hazardous material in black bins.

26- Disconnect the conveying line and cap each end of the tubes.

27- Clean the pneumatic conveying tubes by brushing under fume hood, followed by washing with water.

28- Clean, wash and dry the empty capsule.

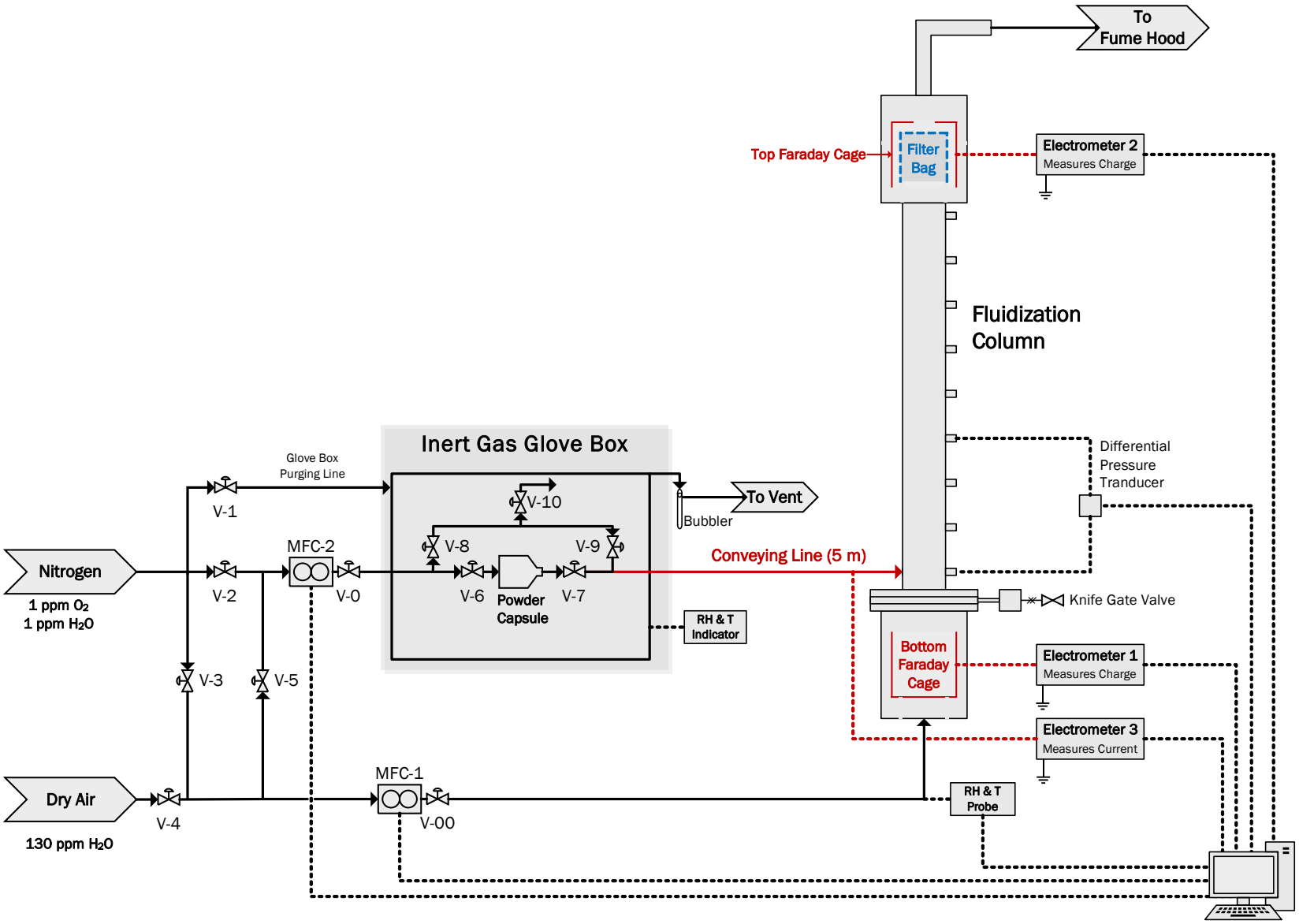

Fig. B - 1. Atmospheric Fluidization Setup Schematic for sample injections

Appendix C – Catalyst polymerization

Ziegler-Natta Polymerization

A common Ziegler-Natta combination consists of $TiCl_3$ supported on $MgCl_2$, an electron donor and a co-catalyst which is $Al(C_2H_5)_2Cl$. Ti atoms on the surface are surrounded by five chlorine atoms and an empty space. $Al(C_2H_5)_2Cl$ donates its ethyl group to fill this orbital and kicks out a Cl atom in this process. Ti atom now has a free orbital to start the reaction with an ethylene monomer as shown in Fig. C - 1.

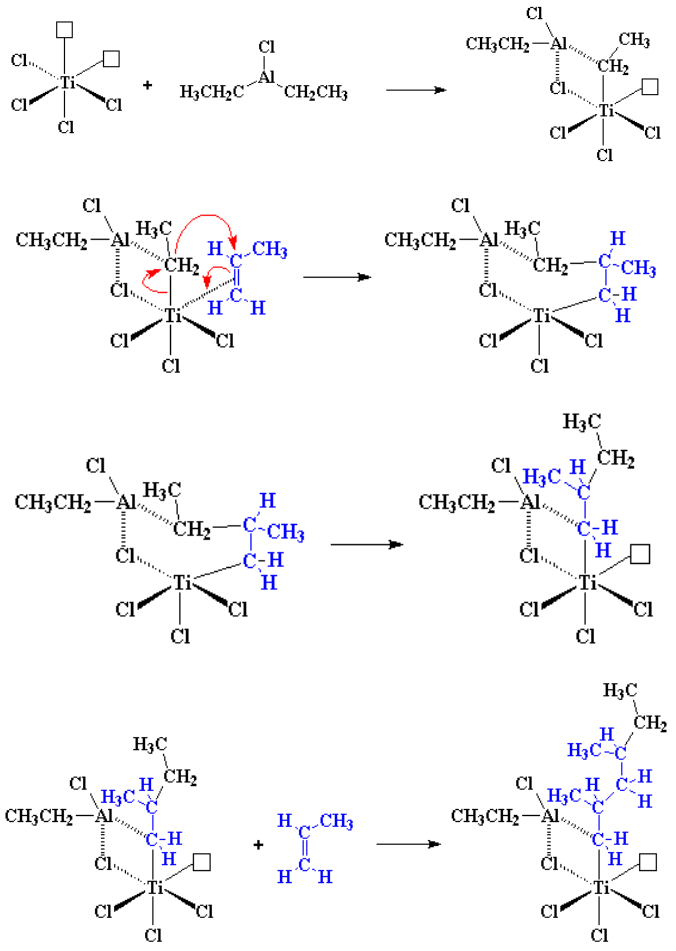

Fig. C - 1. The polymerization process of a Ziegler-Natta catalyst [1]

Metallocene polymerization

Fig. C - 2 shows a zirconium metallocene catalyst along with its co-catalyst (methyl alumoxane (MAO)). MAO replaces the Cl atoms bonded to Zr with its methyl group. One of these methyl

groups can easily fall off and leave Zr atom with a positive charge. However, Zr atom in this condition is still stable since electrons from C-H bond can be shared, but still lacking electrons. Therefore, when a monomer comes in, one of the electron pairs of C-C bond will be shared with Zr. Then, a complex forms and electrons start to move as shown in Fig. B-2. Zr ends up lacking a ligand, but with a C-H bond from the monomer. This process continues and that monomer bonded with Zr, grows.

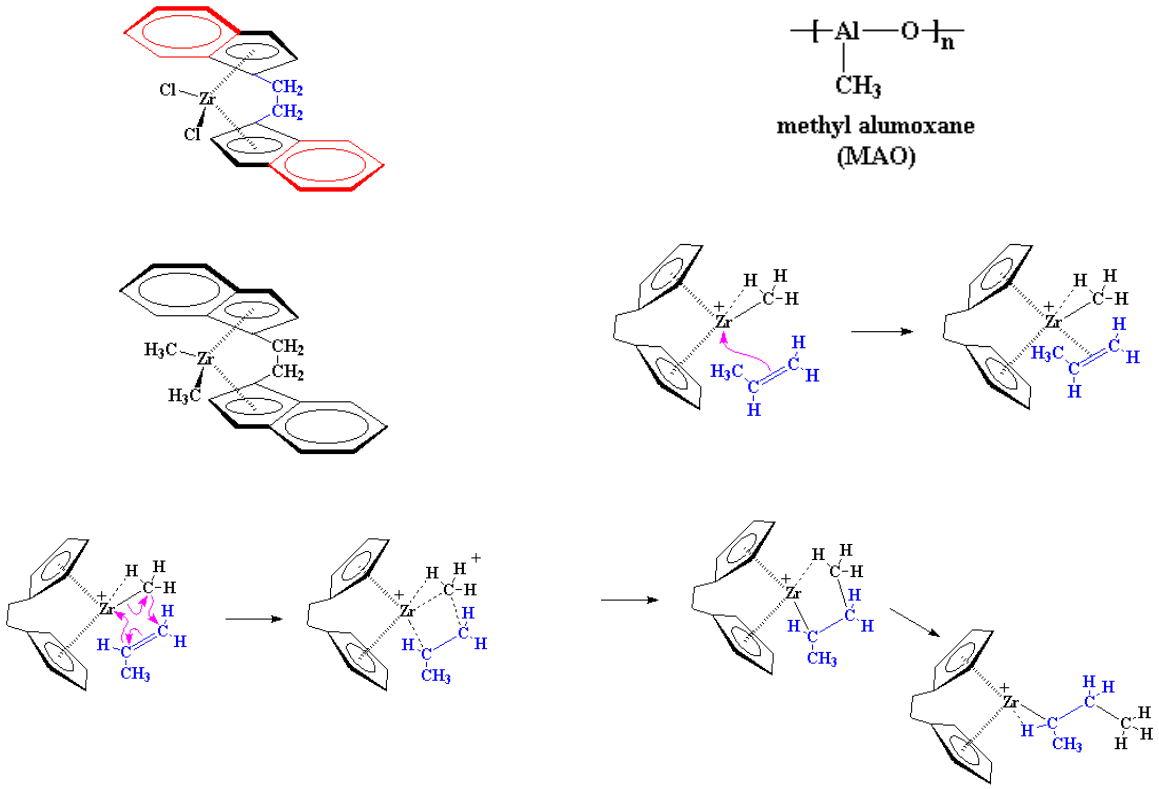

Fig. C - 2. The polymerization steps of a metallocene catalyst [1].

Appendix D – Triboelectric Charging of Particles in Pneumatic Conveying

Table D - 1. Influential Parameters on Triboelectric Charging of Particles in Pneumatic Conveying.

Author	Conveying line				Particle			Conclusions
	Material	ID (cm)	Length (m)	U_g (m/s)	Material	Size (µm)	Density (kg/m^3)	
Smeltzer et al. (1982) [2]	PMMA	2.54	3	39	Glass beads	75 150	2495	Smaller the particle, the higher the loading and the lower the relative humidity, the greater the electrostatic charge generated.
Gajewski (1989) [3]	SS	5	8.8	1.5-15	Polystyrene pearl	400 to 2200	1040	Degree of the material electrification (in C/kg) is greater for smaller particles. For a definite fraction (size) of the particles the Q/m increases when the relative humidity of the air and the solid load decrease, and the transport speed increases.
Masuda et al. (1994, 1998) [4,5]	SS, PTFE, Conductive PTFE, Conductive Nylon	0.6	0.8, 0.07, 0.4, 0.1	29, 30	Fly ash, Alumina, Epoxy resin	3.4, 3.1, 33	2300, 4000, 1450	Powder flow rate and particle charge can be simultaneously measured through on-line calculation based on the currents generated from two metallic pipes.
Matsusaka et al. (2002) [6]	SS	0.46	0.05, 0.25, 0.5, 1, 2	36-77	Fly ash	7	2300	A new model was presented for tribocharging in gas–solids pipe flow based on the number of collisions of a particle with the wall, initial particle charge, and the impact electrification factor characterizing the transferred charge. By increasing gas velocity and pipe length net charge density increases.
Matsusaka et al. (2003) [7]	SS (spiral)	0.6	3	20-39	Fly ash Alumina	4.2 3.9	2300 4000	The mean charge-to-mass ratio of particles increases with pipe length, and reaches an equilibrium (maximum) value, which then depends on the air velocity.
Nifuku and Katoh (2003) [8]	Brass Nylon	5.3 0.69	1 100	10-35 7.5-13.3	Pulverized coal Fly ash	38 20	- 2300	The electrostatic charge increases, reaches a peak and decreases with increase of the particle concentration and the air velocity. Also, the charge polarity change happened for air velocity of more than 30 m/s.
Yao et al. (2004) [9]	PVC	4		11.4 -21.2	PP PP +Glass beads	3.35 – 4.1 38	1400 1414	The effects of several factors such as pipe wall material, particle composition, relative humidity of the conveying air were investigated. Lower air flow rate resulted in the higher induced current and particle charge density. Air with high RH also reduces electrostatic effects.

Author	Conveying line				Particle			Conclusions
	Material	ID (cm)	Length (m)	U_g (m/s)	Material	Size (µm)	Density (kg/m^3)	
Yao et al. (2006) [10]	PVC	4		12.6 -21.2	PVC	3.35 – 4.1	1400	Electrostatic generation was found to increase with the increase of granular attrition in a pneumatic conveying process.
Watano (2006) [11]	SS (SUS 304)	2.8	2	33	PMMA	100 – 200	1090	A corona discharge neutralizer was developed. By increasing gas velocity and mass loading, electrostatic charge generation was controlled.
Matsusaka et al. (2007) [12]	SS, Al, Cu, Brass	0.6	0.5, 1, 2, 3	40	Alumina	3.3	4000	The polarity and the amount of particle charge were found to depend on the pipe material and the length.
Matsusaka et al. (2008) [13]	SS Copper	0.6	0.5, 1, 2, 3 (spiral, 8 cm R)	40	Alumina	3.1	4000	Based on their analysis from the current signals, the total charge, transferred charge, and particle concentration can be measured.
Dragan et al. (2009) [14]	PVC	3.3	2	25	ABS-PC	3000		A higher mass loading will lead to a higher degree of triboelectrification.
Thomas et al. (2009) [15]	Polyurethane	1	6	25	Polyester Al	25	1350	For coated particles, the electrostatic charge generation is controlled by the nature of the coating agent provided that particles are completely covered by the additive rather than the chemical nature of major compound.
Ndama et al. (2011) [16]	PTFE Nylon	1	0.5	21.2	Sugar PVC	45 38	1603 1414	For very dilute transport conditions (solids loadings about 0.001), the charge-to-mass ratio becomes independent of the solids mass flowrate.
Saleh et al. (2011) [17]	PTFE Nylon	1	0.5	5.3 - 44.6	Spherical and Non-spherical glass beads	80 - 500 150-500	2495	Irregularly shaped particles generate more charge than spherical particles. The generated electric current from conveying line increases with the solid's flowrate. The generated charge reduces at RH values larger than 60%. For lower velocities than saltation velocities, plugging phenomenon occurs, leading to a higher particle–wall friction, whereas at higher velocities the increase in charge is due to more energetic collisions.
Schwindt et al. (2017) [18]	PMMA PTFE	2, 5 3	1.32 1.43	4 - 36	PMMA	0.08 - 250	1180	The powder charge first increases with increasing conveying gas velocity and it drops after reaching a maximum. Results

	PVC	3.4	1.43	250 - 500		showed that the charge increases significantly with the inner diameter of the conveying tube.

Author	Conveying line				Particle			Conclusions
	Material	ID (cm)	Length (m)	U_g (m/s)	Material	Size (µm)	Density (kg/m^3)	
Taghavivand et al. (2019) [19]	SS	4.57	0.8, 1.2, 2, 3	20, 30, 60, 100	PTFE Nylon	3.18, 0.79 3.18	2200 1150	Increasing gas velocity increased the charge magnitude of particles due to the stronger collisions. Charge measured by current signals was in a good agreement with the charge measured by the Faraday cage. The particles pathway had a large effect on charging behavior at high gas velocities, whereas at the lowest gas velocity, the total tube length was more influential on particles charging.
Taghavivand et al. (2020) [20]	SS	4.57	1, 3, 5	15, 30	Silica	54	2170–2200	Higher gas velocity and longer conveying line resulted in a higher degree of charge generation. It was observed that increasing the mass loading had an inverse effect on the net specific charge of particles.

Appendix E – Safety Guidelines

Table E - 1. Safety Procedure Regarding Active Catalyst Exposure

Scenario	If	How to address
Spill on the lab floor	The valves of the capsule (V-6 & V-7) at either end become open by accident	Wait for the catalyst to deactivate, then wipe all exposed surfaces with Wypall towels and Hydrobrite 380 mineral oil; dispose them as a hazardous material
Spill inside the glove box	The capsule in method 1 is not properly connected to the conveying line during injection.	Purge glove box with air to deactivate catalyst and follow cleaning procedure from *spill on the lab floor* scenario
Dispersion in air	a) The conveying line in method 1 or the capsule in method 2 is not properly connected to the fluidization column prior to injection. b) Powder manages to escape the top filter bag and the outlet piping is not connected to the fume hood	1) Shut down all MFCs (shut down all gases) 2) Leave the lab for a minimum of 30 minutes to allow catalyst particles to deactivate and settle. 3) Follow cleaning procedure from *spill on the lab floor* scenario

Personal Protective Equipment (PPE)

a) Safety glasses
b) N95 mask
c) Nitrile gloves
d) Lab coat

References

[1] Polymer Science Learning Center, Department of Polymer Science, The University of Southern Mississippi, 2005.

[2] E.E. Smeltzer, M.L. Weaver, G.E. Klinzing, Individual electrostatic particle interaction in pneumatic transport, Powder Technol. 33 (1982) 31–42.

[4] H. Masuda, S. Matsusaka, H. Shimomura, Measurement of mass flow rate of polymer powder based on static electrification of particles, Adv. Powder Technol. 9 (1998) 169–179.

[5] H. Masuda, S. Matsusaka, S. Nagatani, Measurements of powder flow rate in gas-solids pipe flow based on the static electrification of particles, Adv. Powder Technol. 5 (1994) 241–254.

[6] S. Matsusaka, H. Umemoto, M. Nishitani, H. Masuda, Electrostatic charge distribution of particles in gas-solids pipe flow, J. Electrostat. 55 (2002) 81–96.

[7] S. Matsusaka, H. Masuda, Electrostatics of particles, Adv. Powder Technol. 14 (2003) 143–166.

[8] M. Nifuku, H. Katoh, A study on the static electrification of powders during pneumatic transportation and the ignition of dust cloud, Powder Technol. 135–136 (2003) 234–242.

[9] J. Yao, Y. Zhang, C.H. Wang, S. Matsusaka, H. Masuda, Electrostatics of the granular flow in a pneumatic conveying system, Ind. Eng. Chem. Res. 43 (2004) 7181–7199.

[10] J. Yao, C.H. Wang, Granular size and shape effect on electrostatics in pneumatic conveying systems, Chem. Eng. Sci. 61 (2006) 3858–3874.

[11] S. Watano, Mechanism and control of electrification in pneumatic conveying of powders, Chem. Eng. Sci. 61 (2006) 2271–2278.

[12] S. Matsusaka, M. Oki, H. Masuda, Control of electrostatic charge on particles by impact charging, Adv. Powder Technol. 18 (2007) 229–244.

[13] S. Matsusaka, H. Fukuda, Y. Sakura, H. Masuda, M. Ghadiri, Analysis of pulsating electric signals generated in gas-solids pipe flow, Chem. Eng. Sci. 63 (2008) 1353–1360.

[14] C. Dragan, A. Samuila, S. Das, D. Iancu, M. Bilici, L. Dascalescu, Factors that influence the tribo-charging of insulating ducts in suction-type dilute-phase pneumatic transport systems, J. Electrostat. 67 (2009) 184–188.

[15] A. Thomas, K. Saleh, P. Guigon, C. Czechowski, Characterisation of electrostatic properties of powder coatings in relation with their industrial application, Powder Technol. 190 (2009) 230–235.

[16] A.T. Ndama, P. Guigon, K. Saleh, A reproducible test to characterise the triboelectric charging of powders during their pneumatic transport, J. Electrostat. 69 (2011) 146–156.

[17] K. Saleh, A. Traore Ndama, P. Guigon, Relevant parameters involved in tribocharging of powders during dilute phase pneumatic transport, Chem. Eng. Res. Des. 89 (2011) 2582–2597.

[18] N. Schwindt, U. von Pidoll, D. Markus, U. Klausmeyer, M. V. Papalexandris, H. Grosshans, Measurement of electrostatic charging during pneumatic conveying of powders, J. Loss Prev. Process Ind. 49 (2017) 461–471.

[19] M. Taghavivand, B. Elchamaa, A. Sowinski, P. Mehrani, Study of electrostatic charging of single particles during pneumatic conveying, Powder Technol. 355 (2019) 242–250.

[20] M. Taghavivand, B.J. Cho, P. Mehrani, A. Sowinski, Electrostatic charging behaviour of a silica powder during pulse pneumatic conveying, Powder Technol. 366 (2020) 119–129.